Investigation into Strain Propagation to Determine Preserve Regions for Compliant Mechanisms

THE UNIVERSITY OF
WAIKATO
Te Whare Wānanga o Waikato

A thesis submitted

in fulfilment of the requirements

for the degree of

Master of Engineering

At

The University of Waikato

Christoff Venter

2024

Declaration

In submitting this thesis to The University of Waikato School of Engineering, I affirm my awareness of the university's standards and honour code.

Name: Christoff Venter

Signature: 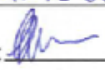

Abstract

This thesis aims to improve the theoretical modelling of compliant mechanisms. The conclusions drawn from this work will help designers understand sources of error associated with strain propagation when designing with lumped compliance. Compliant mechanisms have increased in popularity as they allow for designs that feature lower part counts, increased precision and reduced manufacturing costs. Although using theoretical models to design compliant mechanisms is a useful tool, there is an assumption that only the nodes in a compliant mechanism undergo strain. This is not the case. There is strain occurring outside of the node in a region called the preserve region. The preserve region's impact on the theory is greatly under-explored in the literature.

The preserve region's size, shape, and impact were found and quantified for a range of critical node types. This was done through the use of FEA software by altering the model of a simple, compliant mechanism. The size of the preserve region changed based on the thickness and the fillet used, with an increase of thickness from 4mm to 8mm, causing the radius of the arc that encompasses the preserve region to grow from 8.5mm to 13mm. The shape was also found to be an ellipse, irrespective of the node's geometry. The preserve region's impact on the theoretical models was also quantified. It was found that the thickness has the most drastic effect on the compliance values of the node, increasing the error from 20.53% to 102.18% when the thickness was increased from 4mm to 8mm.

This work shows the importance of considering the preserve region when creating theoretical models of compliant mechanisms. When properly considered, this research shows that the error between the theoretical and the FEA values can be greatly reduced.

Acknowledgments

- I would like to thank my supervisor, Dr Ben McGuinness, for all of his guidance and assistance. His contribution cannot be overstated.
- I would like to thank my assistant supervisor, Ajit Pal Singh. He granted me a lot of guidance and introduced me to the world of compliant mechanisms
- I would like to thank my family and my partner, Jayde, for all their support throughout this journey
- I would like to thank the team in D.G.12 for their assistance with the research, as well as Denis Jouan for his help with understanding DIC.

Table of Contents

List of Figures

List of Tables

Chapter 1

Introduction

Within mechanical engineering, the importance of mechanisms cannot be overstated. They are fundamental to some of the most widely used and crucial designs. Due to the advances in technology, a lot of work and actions previously done by hand are being either enhanced through or outright replaced by the use of mechanisms. Handheld tools such as pliers and vice grips are fundamental mechanisms that enhance human capabilities, while things such as automated robotic grippers allow the removal of the human element altogether. When discussing the mechanisms mentioned before, it is not uncommon to imagine a system with several individual rigid members connected by joints such as pin joints. For many years, this has been the baseline approach to the design of all mechanisms. There are common design issues with traditional mechanisms, such as high part count, assembly costs and manufacturing costs. In an attempt to combat these issues with traditional mechanisms, compliant mechanisms have seen a growth in popularity [1]. A compliant mechanism refers to a mechanism that gains some or all of its motion from the bending and flexing of its members [1]. Compliant mechanisms have seen widespread applications across various fields, including handheld tools, robotics, MEMS (Micro Electrical-Mechanical Systems), and aerospace [2]. Compliant mechanisms have a long list of advantages compared to their traditional mechanism counterparts. They feature lower part counts, lower assembly costs, monolithic structures, reduced friction, lower manufacturing costs and higher precision. [3].

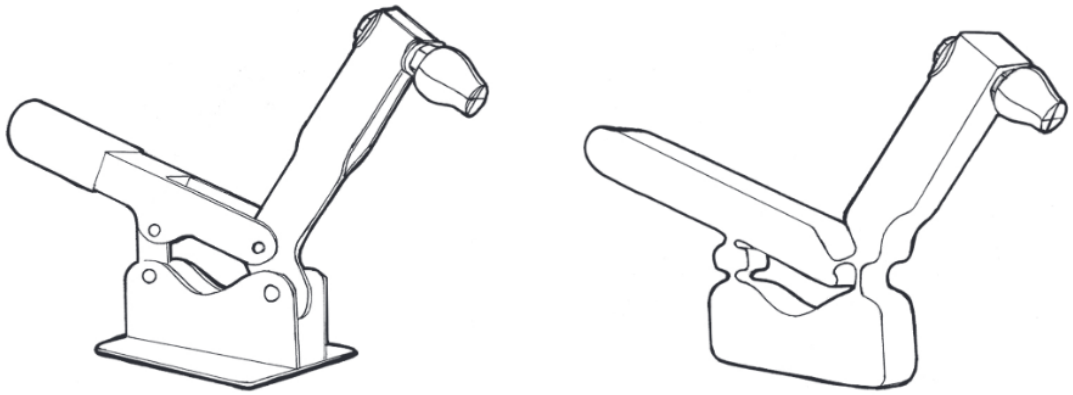

Figure 1.1: *Compliant mechanisms synthesis [3]*

When modelling compliant mechanisms theoretically, there is an assumption that certain sections are flexible while other parts are effectively rigid. This is done commonly within the two main theoretical approaches to modelling compliant mechanisms: the pseudo-rigid-body Model and the compliance matrix method. Although this assumption allows for much faster modelling, it can potentially lead to substantial inaccuracies when compared to experimental results. As compliant mechanisms are commonly designed to be monolithic, the assumption that only part of the mechanism is flexible is not true. When a monolithic compliant mechanism is operating, the whole system technically experiences deformation. The exclusion of deformations in the theoretical modelling leads to an increase in error, as there are unaccounted-for strains that lead to an increased displacement.

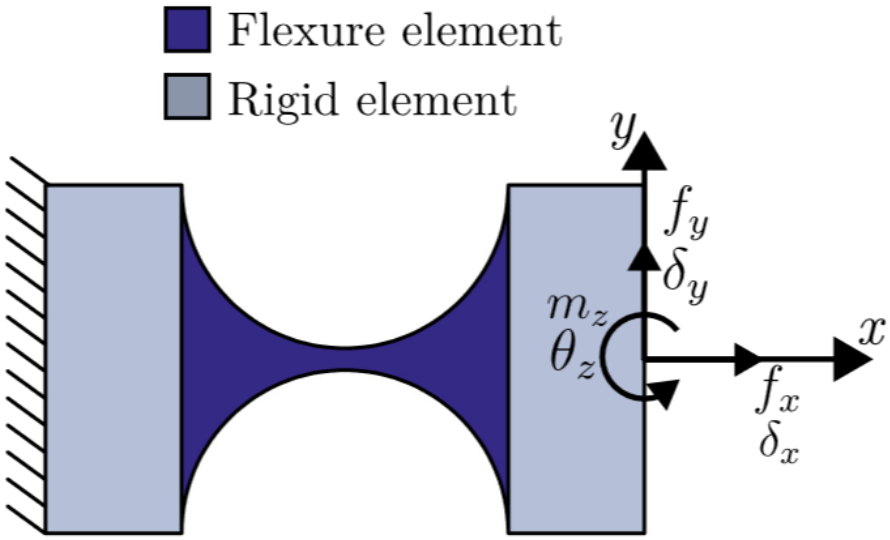

Figure 1.2: *Theoretical model [4]*

1.1 Nodes

When discussing compliant mechanisms, it is important to establish the difference between lumped and distributed compliance. As the names would imply, lumped compliance refers to when most of the compliance (or flexibility) is gained in concentrated areas called nodes. Distributed compliance is when the deformation is spread out across a wider area of the compliant mechanism [1]. Both types of compliance are very valid ways to design compliant mechanisms. However, each is more common in different design methods. When creating designs using a theoretical approach, it is often advantageous to use lumped compliance, as the nodes allow for straightforward modelling. Distributed compliance is more commonly found when using optimisation algorithms such as topology optimization. Distributed compliance can often be desirable, as it allows for the stress to be distributed across the mechanism, allowing for a greater range of motion before yielding. There are many examples of people creating topology optimization algorithms with the explicit goal of trying to distribute compliance. [5]

When designing nodes, there are very few restrictions on what shape it should take. Most commonly, nodes are in the shape of a rectangular cross-section with circular fillets at the corners that connect the node to the rest of the mechanism [6]. There are, of course, more sophisticated node shapes [7–10]; however, these have the same issues as distributed compliance in that they can prove difficult to model mathematically.

1.2 Preserve Region

The preserve region refers to the area where strain is occurring outside of the node that is not accounted for in the theory. Figure 1.3a shows strain in a common node design. Most of the strain in the system is isolated within the node. This is expected as this reduction in thickness leads to a lumped compliance about that node. However, in the same figure, it can be seen that strain is propagating past the node. This strain propagation is referred to as the preserve region. Figure 1.3b shows this strain much more clearly by not including the strain in the node. These strains lead to an increased displacement further down the mechanism and, in turn, reduce the accuracy of the theoretical models.

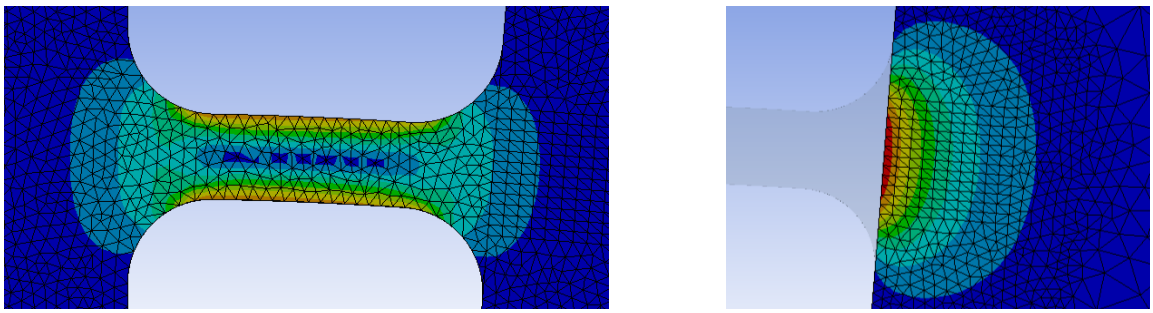

(a) ***(b)***

Figure 1.3: *a) Strain field example b) Preserve region example*

For the node shown in figure 1.3, the preserve region led to a tip displacement that was about 10% larger than what the theory expected. This shows the impact this preserve region can have on the accuracy of the results. As will be discussed in the literature review, very little effort has been made to quantify the impact this region has as well as its size and shape. If the impact can be measured, it can lead to a lot faster theoretical

optimizations in the future, and understanding the size of the preserve region will allow designers to be much more knowledgeable about where their mechanisms are truly rigid and design accordingly.

1.3 Objective

The goal of this thesis is to investigate how strain propagates past the nodes into the preserve region within compliant mechanisms. In this investigation, three main attributes will be investigated and quantified, namely, the size, shape, and effect of this region on the accuracy of the theoretical models. The investigation will cover a range of common node types and will find the attributes discussed earlier as the geometries change for these nodes.

1.4 Contribution

The contributions of this work are as follows:

1. A greater understanding of the shape and size of the strain propagation past the node.
2. A quantification of the effect this strain has on the accuracy of the mathematical models of compliant mechanisms.
3. Knowledge on how certain geometries alter the strain propagation past the node.
4. Validation of the FEA models of these strain propagations through the use of DIC.

1.5 Thesis Overview

The thesis is structured as follows:

Chapter 2 will review the literature relevant to compliant mechanisms, specifically concerning modelling methods and means to validate the results of the research done in this thesis. In this chapter, a theoretical modelling method along with a method of data validation will be selected.

Chapter 3 will cover the method used in the analysis of the preserve region. It will cover how each part of the method met each part of the objective put forward in section 1.3.

Chapter 4 will be where the results of the research are collated and discussed. It will include various graphs showing the changes in errors and displacements over a range of geometries as well as drawing conclusions as to what relationships were found. This chapter will also include where the finite element analysis was verified. This will be done, as mentioned before, through the use of a digital image correlation system.

Finally, chapter 5 will provide concluding remarks and recommendations for future work.

Chapter 2

Literature Review

This chapter will review the current state of the art concerning designing and modelling compliant mechanisms. Firstly, the most commonly used methods for modelling compliant mechanisms will be investigated and compared. Secondly, research will be done into common node geometries as well as applications of compliant mechanisms. Thirdly, strain measurement techniques will be reviewed to find the technique most suitable for the work done in this thesis. Finally, the key research questions will be decided through finding areas in which the existing literature is lacking.

2.1 Modelling Compliant Mechanisms

When designing compliant mechanisms, there are two main approaches: the use of mathematical modelling and the use of computational techniques such as topology optimisation. Within mathematical modelling, there are two main approaches: the compliance matrix method (CMM) and the pseudo-rigid-body model (PRBM). Each of these will be investigated in this section.

2.1.1 Compliance Matrix Method [6]

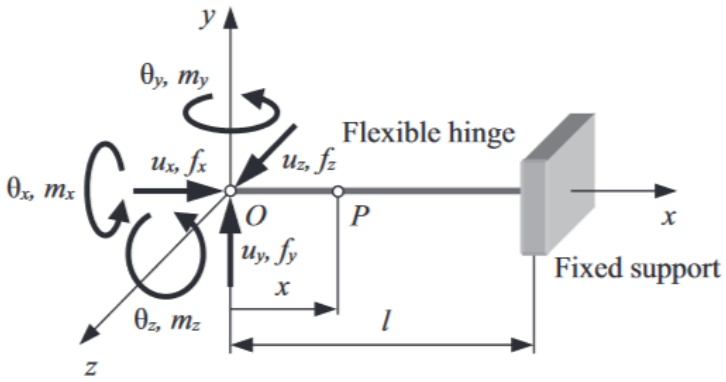

Figure 2.1: *Compliance matrix method diagram*

The first mathematical model researched was based upon the strain-energy Castigliano's second theorem. It takes a matrix approach using the compliances of each of the members in a flexible hinge design. The compliance of a flexible hinge is found in the equation below, which is Castigiliano's second theorem. Equation 2.1 defines the linear displacement of a point as a function of its strain energy and force, while equation 2.2 defines the angular deformation due to its strain energy and moment.

$$u_i = \delta U / \delta f_i \tag{2.1}$$

$$\theta_j = \delta U / \delta m_j \tag{2.2}$$

Equation 2.3 defines the sum of strain energy in all directions of displacement. This equation is then used along with equation 2.1 and 2.2 to relate the strain energy in each direction to the displacement in that respective direction, expressed in equation 2.4.

$$\begin{aligned} U = U_a + U_t + U_b, zU_b, y = \frac{1}{2E}\int_0^l \frac{N(x)^2}{A(x)}\,dx + \frac{1}{2G}\int_0^l \frac{m_t(x)^2}{I_t(x)}dx + \\ \frac{1}{2E}\int_0^l \frac{M_B, z(x)^2}{I_x(x)}dx + \frac{1}{2E}\int_0^l \frac{M_b, y(x)^2}{I_y(x)}dx \end{aligned} \tag{2.3}$$

$$
\begin{aligned}
u_x &= \frac{1}{E}\int_0^l \frac{N(x)}{A(x)} \cdot \frac{\delta N(x)}{\delta f_x} dx = C_{ux-fx} \cdot f_x \\
u_y &= \frac{1}{E}\int_0^l \frac{M_{b,z}(x)}{I_z(x)} \cdot \frac{\delta M_{b,z}(x)}{\delta f_y} dx = C_{u_y-f_y} \cdot f_y + C_{u_y-m_z} \cdot m_z \\
u_z &= \frac{1}{E}\int_0^l \frac{M_{b,y}(x)}{I_y(x)} \cdot \frac{\delta M_{b,y}(x)}{\delta f_z} dx = C_{u_z-f_z} \cdot f_z + C_{u_z-m_y} \cdot m_y \\
\theta_x &= \frac{1}{G}\int_0^l \frac{M_t(x)}{I_t(x)} \cdot \frac{\delta M_t(x)}{\delta m_x} dx = C_{\theta_x-m_x} \cdot m_x \\
\theta_y &= \frac{1}{E}\int_0^l \frac{M_{b,y}(x)}{I_y(x)} \cdot \frac{\delta M_{b,y}(x)}{\delta m_y} dx = C_{\theta_y-f_z} \cdot f_z + C_{\theta_y-m_y} \cdot m_y \\
\theta_z &= \frac{1}{E}\int_0^l \frac{M_{b,z}(x)}{I_z(x)} \cdot \frac{\delta M_{b,z}(x)}{\delta m_z} dx = C_{\theta_z-f_y} \cdot f_y + C_{\theta_z-m_z} \cdot m_z
\end{aligned}
\tag{2.4}
$$

It is in equation 2.4 that the variable "compliance" or c can be seen. These equations can then be used to find the individual compliances that create a compliance matrix:

$$
\begin{aligned}
&C_{ux-fx} = \frac{1}{E}\int_0^l \frac{dx}{A(x)}; \qquad C_{\theta x-mx} = \frac{1}{G}\int_0^l \frac{dx}{I_t(x)}; \\
&C_{uy-fy} = \frac{1}{E}\int_0^l \frac{x^2 dx}{I_z(x)}; \quad C_{uy-mz} = -\frac{1}{E}\int_0^l \frac{x dx}{I_z(x)}; \; C_{\theta y-my} = \frac{1}{E}\int_0^l \frac{dx}{I_z(x)}; \\
&C_{uz-fz} = \frac{1}{E}\int_0^l \frac{x^2 dx}{I_y(x)}; \qquad C_{uz-my} = \frac{1}{E}\int_0^l \frac{x dx}{I_y(x)}; \; C_{\theta z-mz} = \frac{1}{E}\int_0^l \frac{dx}{I_z(x)}; \\
&C_{\theta z-fy} = C_{uy-mz}; \qquad\qquad C_{\theta y-fz} = C_{uz-my};
\end{aligned}
\tag{2.5}
$$

Compliance defines how easily a node deforms due to an induced force or moment. It can be modified by changing the innate property of a material's Young's modulus or by altering the geometry. Reducing the stiffness or second moment of the area will increase compliance. Using this method results in a matrix of compliances for each member. Each compliance is multiplied by its corresponding force, and the displacement in the direction of the compliance can be found. The compliance matrix can be seen in equation 2.6:

$$[C] = \begin{bmatrix} C_{ux-fx} & C_{ux-fy} & C_{ux-mz} \\ C_{uy-fx} & C_{uy-fy} & C_{uy-mz} \\ C_{\theta z-fx} & C_{\theta z-fy} & C_{\theta z-mz} \end{bmatrix} \tag{2.6}$$

$$[u] = [F][C]$$

As this thesis only considers a 2D scenario, all of the out-of-plane motion is ignored, and the compliance matrix can be simplified further. Particularly, C_{ux-fy} and C_{ux-mz} is 0 as a y-directional force and a moment about the z-axis will not affect the compression of the system. $C_{\theta z-fx}$ and C_{uy-fx} are also considered zero as a force in the x direction will have no impact on the vertical displacement and angle about the z axis of the scenario. Finally, as can be seen from equation 2.5, $C_{\theta z-fy}$ is the same as C_{uy-mz}, further simplifying the matrix down to the most common compliance matrix:

$$[C] = \begin{bmatrix} C_{ux-fx} & 0 & 0 \\ 0 & C_{uy-fy} & C_{uy-mz} \\ 0 & C_{uy-mz} & C_{\theta z-mz} \end{bmatrix} \tag{2.7}$$

After using the listed equations, the matrix layout will produce a compliance matrix for a node with a reference point O_1 right at the end of the node. This means when the compliance matrix is multiplied by the force matrix, the displacement matrix is about reference point O_1. If the reference point was to be away from the end of the node at point O_2, i.e. the displacement matrix for a point away from the node is needed, a translation matrix is introduced. The translation matrix follows the format as shown below:

$$[T] = \begin{bmatrix} 1 & 0 & 0 \\ 0 & 1 & 0 \\ \Delta y & -\Delta x & 1 \end{bmatrix} \tag{2.8}$$

Where Δy and Δx are the y and x distance from point O_1 to point O_2. This translation

matrix can be used to find a compliance matrix about O_2 knowing the distance from and the compliance matrix of O_1. This is done using the equation shown below:

$$[C_{O_2}] = [T]^T \cdot [C_{O_1}] \cdot [T] \tag{2.9}$$

The first translation matrix $[T]^T$ is a transposed version of the translation matrix $[T]$. This is because the displacement at point O_2 will be different to O_1 based on the angular deformation. The difference is that the angular displacement at the node boundary will cause additional displacement equal to the angle of the deflection at the node multiplied by the x and y distance from point O_1 to O_2. The second translation matrix $[T]$ is included to account for the fact that the forces described relative to $[C_{O_1}]$ will now be different as the location is now relative to O_2 as opposed to O_1. Now, if the load is acting at point O_2, it will also induce a moment relative to point O_1.

The largest advantage of using this method to calculate the response of a compliant mechanism is that it can easily account for a scenario with multiple loads and multiple hinges. Since there is a compliance for every direction for a load in every direction, in scenarios where there is both a moment, axial force and vertical (shear) force, this method will be able to accurately account for the combined effect of all the loads. Later in the reading, Lobuntiu et al. also show how these matrices can be rotated, allowing calculations for rather complex combinations of forces and hinges.

The main issue with this method is that when performing the calculations, the method did not accurately account for the displacement in the x direction due to a force in the y direction. This is fine for mechanisms with relatively small deflections, as the change in the x direction would be so small it would be negligible. However, as the deflection gets larger, this becomes more of a factor to account for.

2.1.2 Pseudo Rigid Body Model

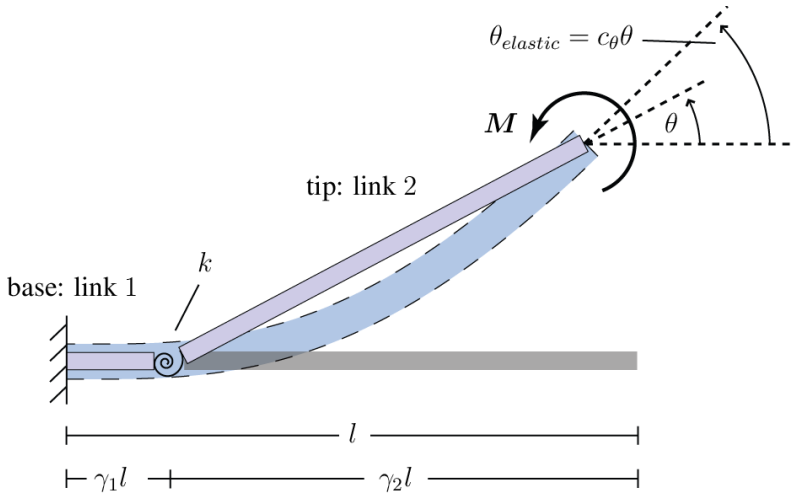

Figure 2.2: *Pseudo-rigid-body model diagram*

The pseudo-rigid-body model aims to model compliant mechanisms by relating them to traditional rigid link mechanisms [11]. The pseudo-rigid-body model achieves this by simulating the compliant mechanism as a rigid link system where the flexural members are considered to be torsional springs. These springs each have a rotational spring constant that provides a resistive force to angular displacements. This model was used to develop 2 further methods to aid in the analysis of compliant mechanisms, namely the conventional Newtonian methods, and the principle of virtual work.

2.1.2.1 Conventional Newtonian Methods

As the name suggests, this method uses the pseudo-rigid-body model in conjunction with conventional Newtonian methods to find solutions to various analyses. In this method, the pseudo-rigid body model is formed. This model is then treated as a free-body diagram, and the applied forces and boundary conditions are added. Equations of static equilibrium are formulated for each link, which is then solved using the boundary conditions and applied forces. The product is an equation that relates an applied force or torque to an equilibrium displacement or rotation.

2.1.2.2 Principle of Virtual Work

This method is also derived from the pseudo-rigid-body model. Through the use of generalised coordinates, this method allows an analysis of the system as a whole as opposed to individual members. This allows for a much faster analysis as each link does not need equations of static equilibrium formulated. Using the generalised coordinates found in this method allows a virtual displacement to be found, a displacement expressed as a function of these coordinates. Knowing the virtual displacement as well as the applied forces, a virtual work can be found (W=Fd). Assuming that the system is in equilibrium, this net virtual work would equate to zero, as the potential energy stored in the springs perfectly counteracts the work being done by the applied forces and an equation of equilibrium for the system as a whole can be found.

2.1.3 Topology Optimization

Due to the nonlinear nature of modelling compliant mechanisms, many optimisation methods are used to help reach a final design. Among these optimisations, topology optimisation is very common. Topology optimisation finds the best material distribution for any given set of constraints or design domain [5]. It does this by distributing elements throughout the design domain and applying constraints to the elements according to the boundary conditions and loads desired for the design. Then, through using an algorithm and optimisation formulae, elements are eliminated if they are experiencing any stress or do not meet any other criteria, e.g. a minimum or maximum thickness [12]. This leads to a very efficient process that can form very complex shapes that can meet the desired input-output relationship.

There are many algorithms available for use to experiment with topology optimisation [13–25]. All of these algorithms have their advantages and disadvantages, hence why sometimes some intervention is needed from the designer when using this method. Often, topology optimisation is only a step within the design process of compliant mechanisms

[26, 27]. Engineers will provide the algorithm with a very broad idea of what the design requires, e.g. inputs, outputs and boundary conditions. The optimised shape is then given by the algorithm. However, often, these shapes contain unfeasible hinges that would not function in real life. Many of the aforementioned algorithms attempt to tackle this issue. Often, it simply comes down to the designer deciding on certain dimensions and using the topology optimisation as a guide of the general shape of the mechanism, followed by changes to the dimensions and further optimisations, as seen in the work done by Chi et al. [28].

2.2 Material Selection

When designing a compliant mechanism, often a large amount of deflection is required. This large amount of deflection implies that the mechanism must be able to generate the least amount of stress during its deformation and must also be able to withstand the most amount of stress possible [11]. This is where a common misconception is made. Often there is an assumption that a stiff material is a strong material, however, this is not wholly the case. Many materials have a large amount of strength whilst also exhibiting a low stiffness. This is where the notion of strength-to-stiffness ratio comes into play [11]. A material that is optimal for a compliant mechanism is a material with a low Young's modulus (stiffness) and a high amount of strength, as a flexible material will experience less stress for the same amount of deformation, and a strong material will only yield when the stress becomes very large. Therefore, the ratio between stiffness and strength is very important when selecting a material for a compliant mechanism. Table 2.1 details several examples of materials as well as their strength-to-stiffness ratios

Table 2.1: Materials and their associated strength to stiffness ratio [11]

Material	Stiffness (GPA)	Strength (MPA)	Ratio (×1000)
Steel (1010hot rolled)	207	179	0.87
Steel (4140 Q& T @400)	207	1641	7.9
Aluminium (1100 annealed)	71.7	34	0.48
Aluminium (7075 heat treated)	71.7	503	7.0
Titanium (Ti-35A annealed)	114	207	1.8
Titanium (Ti-13 heat treated)	114	1170	10
Beryllium copper (CA170)	128	1170	9.2
Polycrystalline silicon	169	930	5.5
Polyethylene (HDPE)	1.4	28	20
Nylon (Type 66)	2.8	55	20
Polypropylene	1.4	34	25
Kevlar (82 vol %) in epoxy	86	1517	18
E-glass (73.3 vol %)in epoxy	56	1640	29

From table 2.1, it can be seen that certain materials surpass others in terms of applicability for compliant mechanisms. The three that stood out are Titanium (Ti-13 heat treated), E-glass, and Polypropylene. Titanium has an extremely high strength-to-stiffness ratio, considering it is a metal, as it allows compliant mechanisms to be designed with many advantages exclusive to metals. When it comes to simply the best ratio, E-glass in epoxy surpassed all the other materials mentioned. It is, however, quite hard to source compared to some of the other materials, particularly compared to polymers. It is for this reason that polypropylene is considered one of the best materials for compliant mechanisms, as it exhibits an impressive strength-to-stiffness ratio whilst also having many of the advantages that come with polypropylene [29].

2.3 Node Geometries

Much of the mathematical modelling methods are based on the assumption that a compliant mechanism can be simplified down to a combination of nodes and rigid links. Research was done into common node geometries to help gain a better understanding of what sort of shapes are critical to be able to be modelled. It is worth noting that all of the node geometries not included in the novel geometries section are distinct examples of lumped compliance, where most of the flexibility is gained at a certain point.

2.3.1 Rectangular Cross Section

This is the basis of most compliant mechanisms [6]. This is due to its ease of modelling as well as the constant thickness and width of these sections leading to a simple second moment of area calculation ($I = \frac{bh^3}{12}$). When not filleted, there is a substantial amount of stress present at the connection between the flexible hinge and the rigid sections.

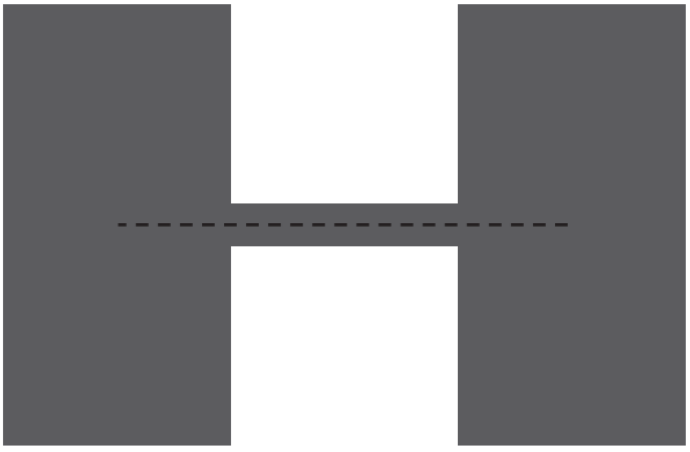

Figure 2.3: *Rectangular cross section*

2.3.2 Rectangular Filleted Hinge

It is extremely common for flexible hinges to include fillets at the corners of the node [6, 30]. This fillet comes commonly in 2 forms: a circular fillet or an elliptical fillet. It allows for superior distribution of stress throughout the member and negates the effects of stress concentrations. Seeing as much of the theory does not account for stress concentration factors in flexible hinges and that it can account for the impact of fillets, this allows for not only stronger designs but also more accurate modelling [6]. Assuming the node has a circular fillet, all that is needed to calculate the motion of the hinge is the length, the thickness, and the radius of the node. It is also possible for the hinge segment to only consist of circular sections. In this case, the fillets that attach to the rigid bodies meet in the middle and form a large semicircle. This is often the case for very small flexible hinges, as the short length does not allow for a flat rectangular section in the middle.

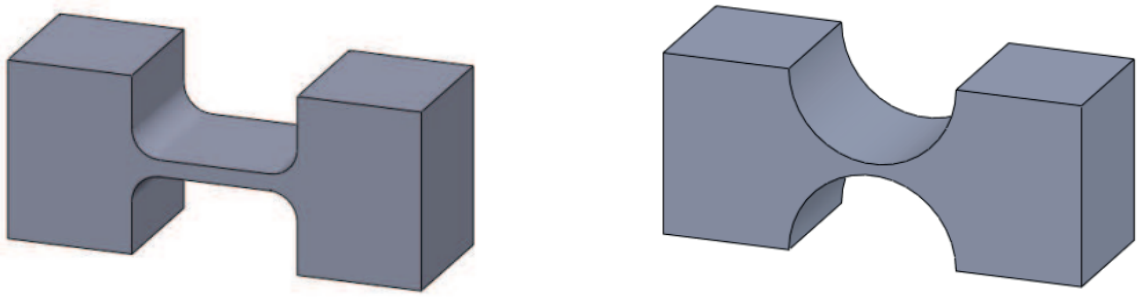

(a) ***(b)***

Figure 2.4: *a) Circular filleted hinge b) Circular hinge [31]*

Another common hinge shape is elliptical. This is very similar to that of the circular shape in that it is often used to form fillets. Knowing the key dimensions, such as the a and b value of the ellipse found in figure 2.5 as well as the length and thickness of the rectangular part of the hinge, allows for fairly simple compliance calculations as well.

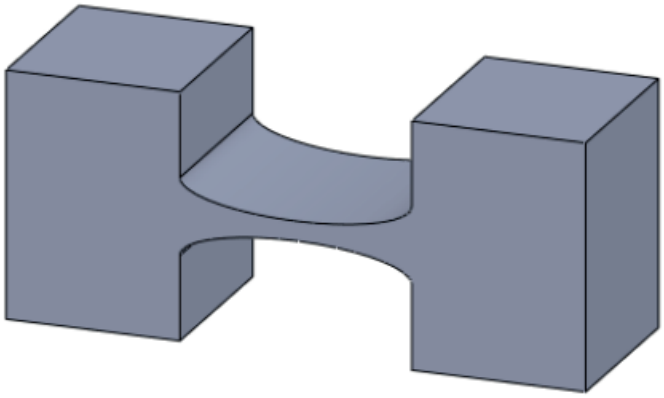

Figure 2.5: *Elliptical hinge [31]*

2.3.3 Novel Geometries

The following will be some other noteworthy geometries. These geometries are far more specialised and were noted throughout the review for their interesting advantages and, therefore, are worth quickly mentioning. These types of node geometries are likely not going to be included in the research as they are much harder to manufacture, and their niche design applications do not make it critical to gain an understanding of node geometries.

2.3.3.1 Leaf Spring

A leaf spring refers to a node that consists of a long, thin strip of material [32]. It resembles a rectangular hinge. However, due to its long length, especially when compared to its thickness, it exhibits a very large range of motion. There is a configuration of 2 leaf springs that allow for a substantial amount of rotational displacement. This configuration is called a cross spring and is commonly used when a large amount of displacement in a circle is required [8].

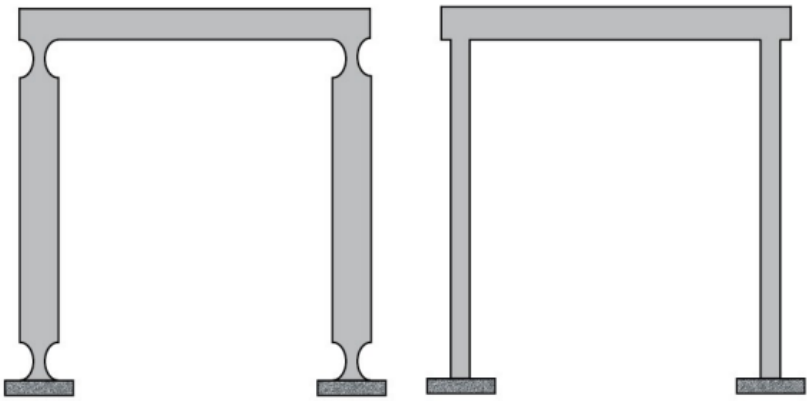

(a)

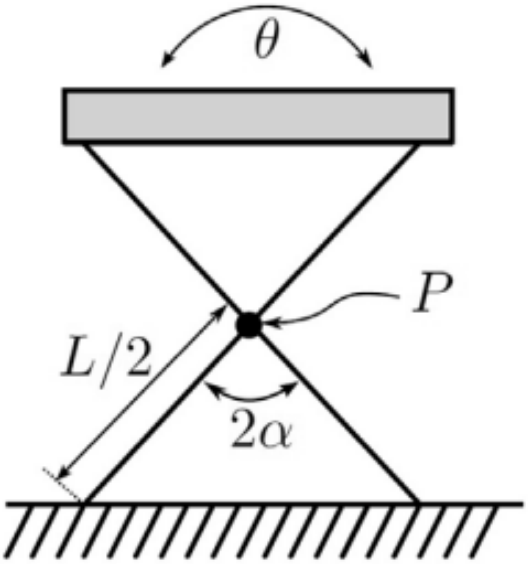

(b)

Figure 2.6: *a) Leaf spring b) Cross spring*

2.3.3.2 Butterfly Hinge

The butterfly hinge refers to a compliant hinge that is similar to the cross spring. It consists of 8 flexures and two rigid shuttles with a central x-shaped rigid block [8, 33]. A common issue with cross springs is what is called "parasitic motion". This refers to undesired motion in the mechanism, which in the case of cross springs is any motion that is not in the circular direction. Butterfly hinges counteract this by having the parasitic

motion of one pair of cross springs counteract the parasitic motion of the other, effectively negating it. It is for this reason that butterfly hinges are a common way to achieve circular motion with compliant mechanisms [7].

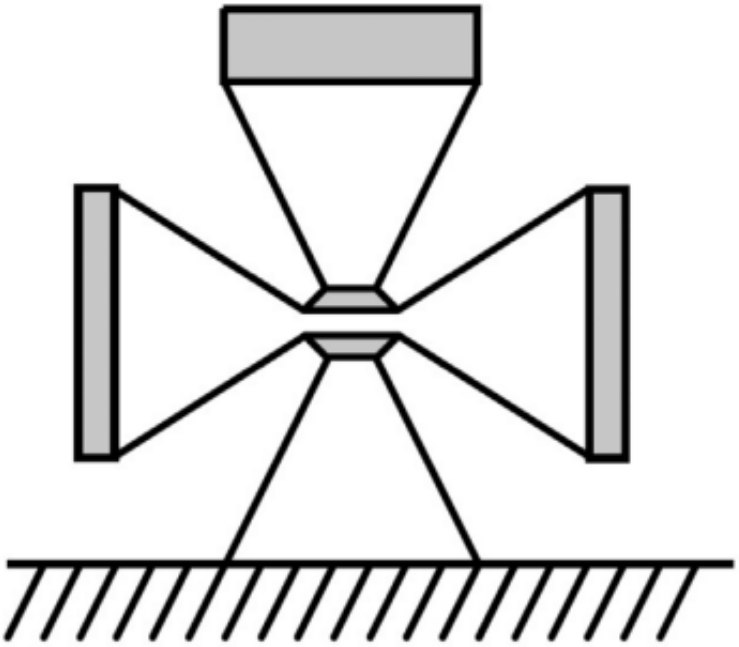

Figure 2.7: *Butterfly hinge*

2.3.3.3 Folded Flexure Hinge

When designing compliant mechanisms, there are concerns surrounding the changing stiffness of the node as the mechanism is actuated [9, 10]. To combat this concern, folded flexure hinges are used. These designs are similar to leaf springs and involve geometry arranged in such a way that at certain levels of motion, the system will gain increased stiffness or support from itself. This can be achieved by designs found in figure 2.8a 2.8b, where the flexible member is either curved to begin with, seen in 2.8a or through a design that supports itself once the members are under load as seen in figure 2.8b.

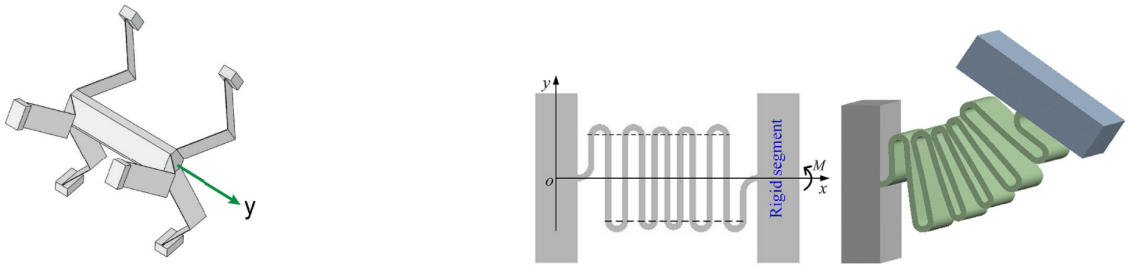

(a) *(b)*

Figure 2.8: *a) Folded leaf spring b) Pitch varying folded flexure hinge*

2.4 Preserve Region

As mentioned in the introduction, there is a rather crucial assumption that only part of the compliant mechanism experiences deformation. The largest issue with this assumption is that it ignores any strain occurring outside of the node. Comparisons made within Lobuntiu's book [6] show that the compliance matrix method can show extremely high accuracy for tip displacements of nodes using finite element analysis. In these cases, however, the model only contained the node and nothing else. This makes it not a perfect representation of a real compliant mechanism, as it is not common for the start of the node to be perfectly fixed, and the load is not necessarily right at the end of the node. In cases where these two factors are not true, meaning the load is not applied right at the end of the node and the fixed point is located somewhere else on the mechanism, there will be a preserve region present.

These occurrences within compliant mechanisms are under-discussed. The most noteworthy discussion surrounding the strain not present within the node region was a paper written by Rösner et al. [34]. In this paper, they acknowledge that when designing compliant mechanisms with lumped compliance, a noteworthy part of the flexibility is gained outside of the node as well. The goal was not to account for this flexibility on a theoretical level but to optimise simulations by reducing the number of nodes used. This was achieved by specifying a significant region model, where the model is simplified to only consider regions where there is a significant amount of strain. It does not discuss these

significant regions within the context of their effect on a theoretical approach, nor does it try to conclude the shape or size that the preserve region has for various geometries.

2.5 Applications

2.5.1 Compliant Robotic Gripper

When investigating the uses of compliant mechanisms, a wide assortment of compliant grippers can be found. A compliant robotic gripper is a pristine example of compliant mechanisms being applied to help improve an area of design. Before the large push for compliant grippers, robotic end effectors were made with traditionally jointed mechanisms [35–37]. These designs are useful in certain applications. However, there are certain properties present in compliant mechanisms that allow for a wider range of uses compared to their traditional counterparts. Following will be several examples that show the advantages of compliant mechanisms applied to robotic grippers.

2.5.2 Constant Force Gripper

A constant force gripper is a variant of the compliant robotic gripper. It is an example of the advantages of applying the theory when designing compliant mechanisms. Through the use of mathematical optimisation, a design was able to be generated where the force applied to the specimen was constant throughout the range of motion of actuation. If this were to be achieved through the use of traditional mechanisms, it would likely involve many individual parts and springs as well as sensors to ensure that the force limits are not exceeded. Through the use of the innate ability of compliant mechanisms to elastically deform and store strain energy, a design can be optimised in such a way that throughout the range, the strain energy stored within the grippers is constant, meaning the force exerted on the object is constant irrespective of where contact is made. It can achieve this

property while also maintaining the long list of other advantages of compliant mechanisms, such as the reduced part count and monolithic nature. An example of a constant force gripper was found that performed very well [38].

2.5.3 Micro Grippers

Another large advantage of using compliant mechanisms is its simplicity and high precision. It is for this reason that extremely small grippers are much easier to design when using compliant mechanisms [27, 39]. Designing with traditional mechanisms on such a scale is impractical, as trying to form such small joints would lead to such tiny parts that they would be difficult to manufacture and assemble. Designing these micro grippers using compliant mechanisms allows the entire gripper to be made out of one small mould [27]

2.5.4 Micro Electrical-Mechanical Systems

Another area of application for compliant mechanisms that cannot be ignored is Micro Electrical Mechanical Systems (MEMS) [12, 40, 41]. This design space takes advantage of the high precision and low part count of compliant mechanisms, as much like the micro grippers, traditional linkage methods would lead to an extremely difficult design process. Kota et al. [12] discusses a microstroke multiplier that showed outstanding robustness, endurance, and resistance to surface adhesion along with no apparent fatigue.

2.6 Strain Measurement Techniques

Following is a collection of strain measurement techniques that were considered to be used within this thesis. It will cover the key features of each strain measurement technique along with its advantages and disadvantages, particularly with regard to the work being done in this thesis.

2.6.1 Strain Gauges

One of the most popular methods of measuring strain is strain gauges. Strain gauges operate by outputting a voltage based on the amount of deformation in the gauge from an applied force or pressure [42]. This makes using strain gauges extremely simple, as all that is needed is to attach the strain gauge to a surface, supply it with an input voltage and read the output voltage. This ease of use, as well as the impressive accuracy, is what made strain gauges so popular [43]. The main issue for this project is that the strain gauges only measure strain in one dimension. This means that achieving a full field strain assessment would be very difficult, as this would require multiple strain gauges in multiple locations, leading to a better alternative to be investigated.

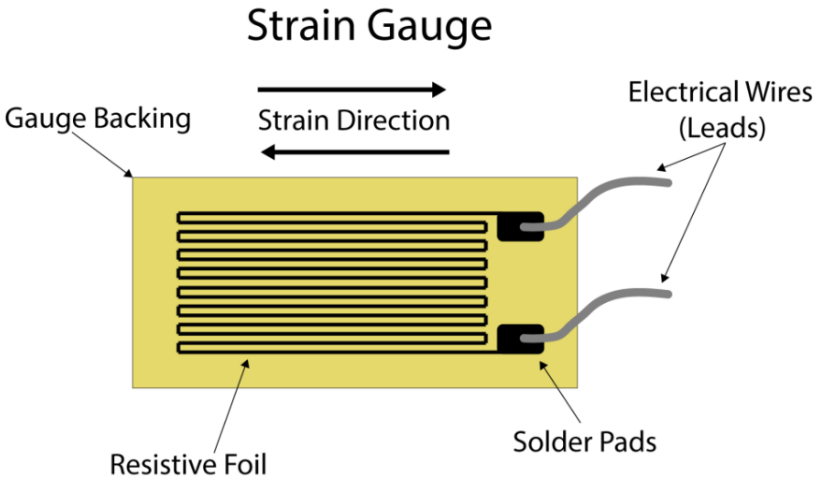

Figure 2.9: *Strain gauge diagram [42]*

2.6.2 Electronic speckle pattern interferometry

When investigating methods of strain measurement, Electronic speckle pattern interferometry came up several times [44–46]. This method is one of the earliest attempts at a wider field of strain measurement. It uses a reference film over the measured object, and by shining light or a laser at the surface, the reflected waves will create fringes upon the film [47, 48]. These fringes are then used to calculate the displacements along the

surface of an object. Although modern examples of ESPI being used do exist [49], this technique is largely outdated. It requires a very sensitive and complicated setup as well as a substantial amount of input from the observer to calculate the final displacement vectors. It is also used for much smaller scale applications than what will be required in this thesis, making this an unlikely candidate for measuring the strain across the entire surface of a compliant mechanism.

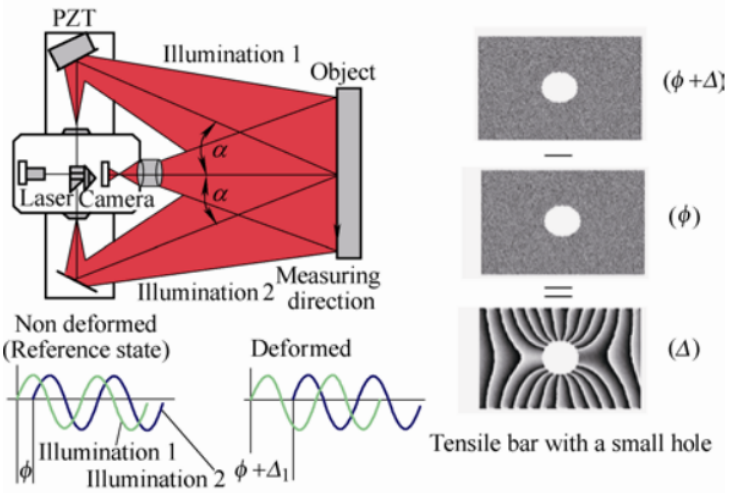

Figure 2.10: *Typical ESPI setup for in-plane displacement measurement [48]*

2.6.3 Moire technique

The Moire Technique is a more modern technique than ESPI. It also uses the movement of fringes to calculate displacement vectors, however, it does not use lasers or lights but rather a reference grid. The reference grid consists of very small slits that line up with another grid that is implanted onto the examined object. As the object deforms, the reference and object grids cause moving fringes to become present. The motion of these fringes is then interpreted to find the displacement of the object's surface [46]. This method is much easier to set up and interpret than ESPI. However, it still requires a large amount of knowledge surrounding the movement of these fringes to achieve usable data. It is also capable of a much wider area of analysis than ESPI. However, most applications use the Moire technique on a very small scale [44].

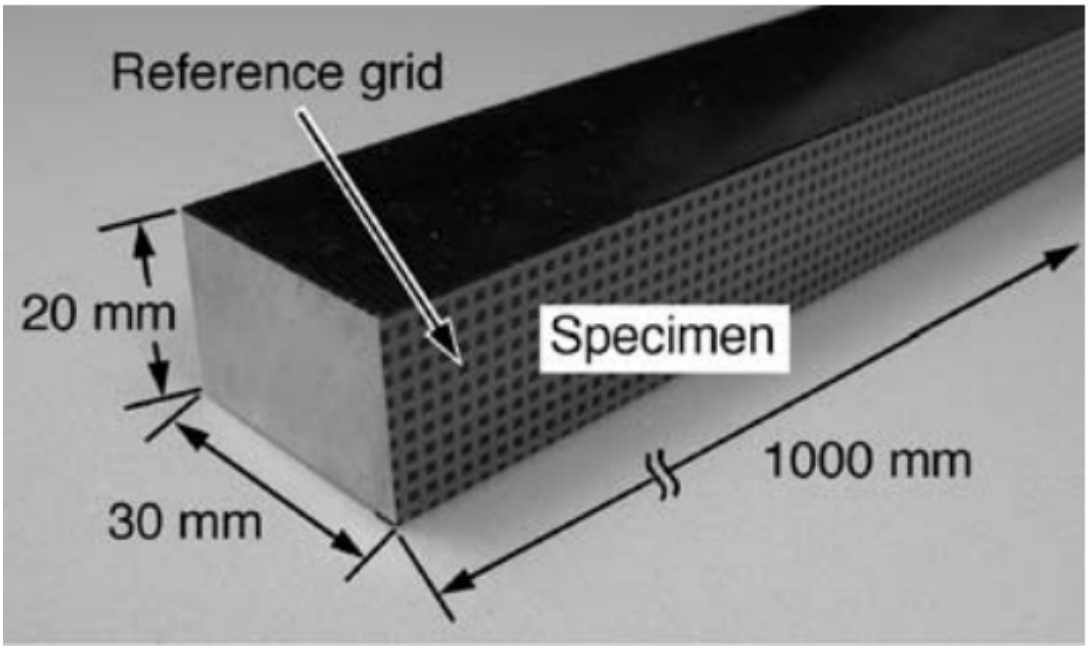

(a)

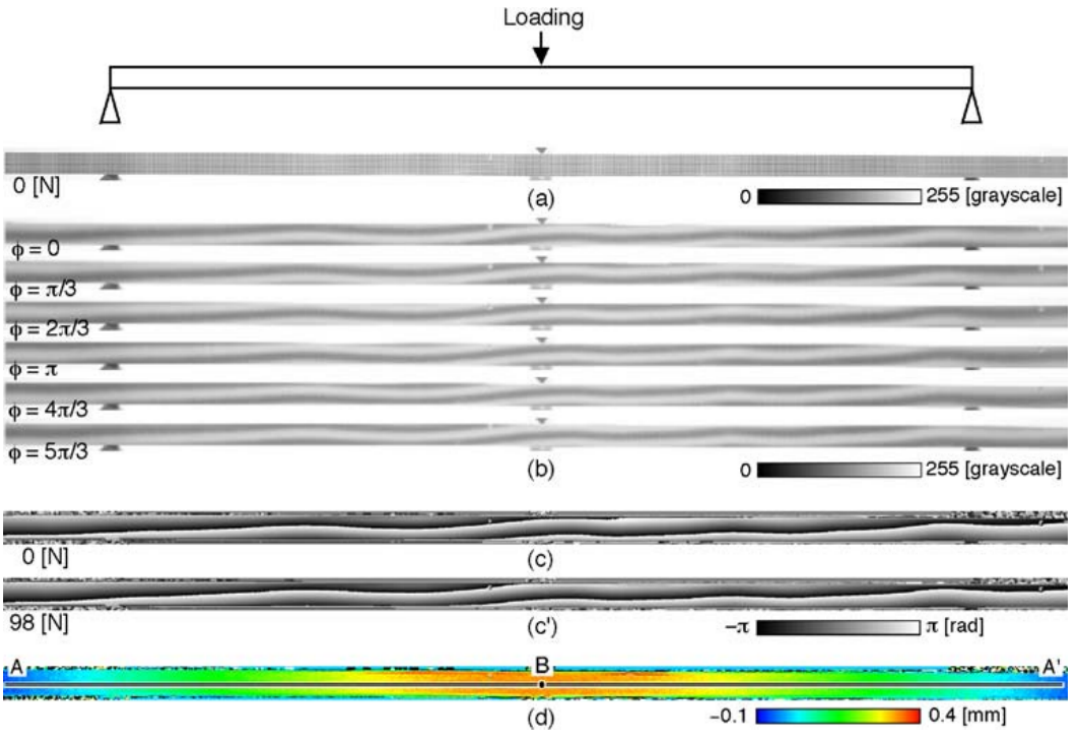

(b)

Figure 2.11: *a) Reference grid used in Moire method [44] b) Fringes forming during deformation [44]*

2.6.4 Digital Image Correlation

Digital Image Correlation, or DIC, is one of the newest forms of full-field strain measurement. It involves applying a speckle pattern across the surface of a sample and using a camera to measure displacements. DIC works by taking several images during loading. A subset of pixels is taken from the first image (known as the reference image) [50]. The software finds the position where the pixels most likely moved to. It does this for subsets of pixels throughout the entire area analysed and grants an image of all the strains across the speckle pattern. DIC is likely the best option currently for full-field strain measurement. It requires a very simple setup, very little user input to find the data, and is extremely accurate with its results (within 0.2 % error) [51]. It can also measure strain over a large range of sizes, from extremely small to relatively large components.

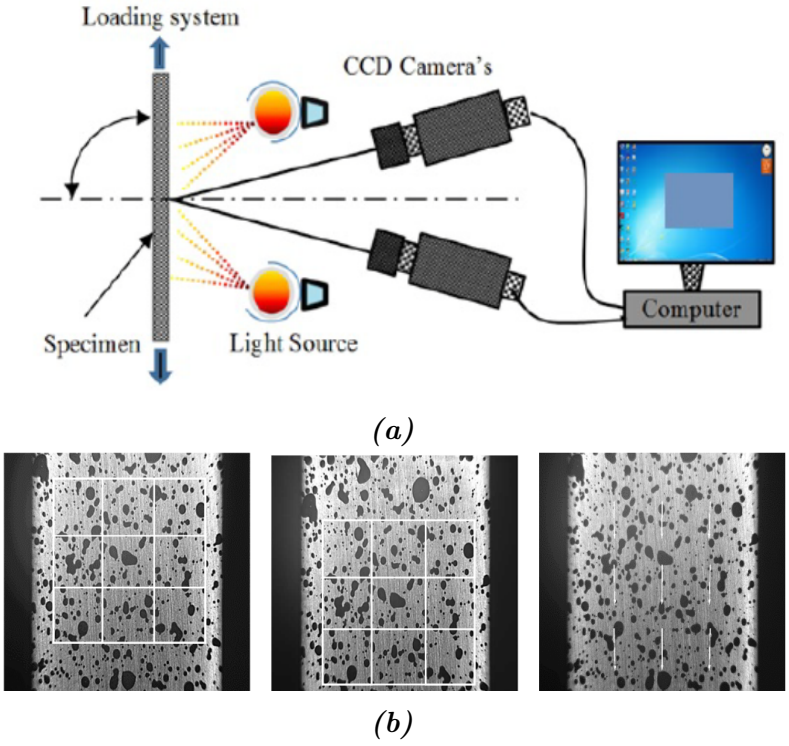

Figure 2.12: *a) DIC setup [52] b) Speckle pattern [53]*

While investigating DIC as an option for measuring strain, some examples of its application within compliant mechanisms were found.

2.6.4.1 Vision-Way Testing in Design of Small Compliant Mechanisms

In this study [54], Hricko et al. aimed to explore the modelling of compliant mechanisms, both mathematically and using FEA software. They intended to verify these models using an experimental setup that utilises a vision method of testing. In this experimental setup, they tested several different methods of displacement sensing and measured the displacement at one of the nodes of a parallelogram-compliant mechanism.

Although this study was good at concluding inaccuracies in the models and able to state that physical tests are crucial for the design of compliant mechanisms, they did not cover a large area in their analysis. The vision way of testing only measured the motion of one point and hence made no effort to understand the strain occurring outside of the nodes. In the following research, not only will the displacement of a node be analysed, but the full field of strain will be measured. This will grant a more in-depth understanding of where the errors lie and allow for a far greater comparison to the finite element analysis, as the preserve region will be captured on camera. The effect of material fabrication was also not considered in this study. They performed the testing on a 3D-printed specimen that may have had an impact on how the system would respond to a load.

2.6.4.2 Motion measurement system of compliant mechanisms using computer micro-vision

The goal of this study was to propose a new method of motion measurement, specifically measuring motion on a very small scale [55]. To achieve this, an optical flow-based technique using computer micro-vision was proposed and tested on an experimental compliant mechanism. In testing, they received both theoretical results using mathematical modelling as well as simulated the mechanism using FEA software and compared the results.

The proposed computer micro-vision technique turned out to be successful. However, to gain a better understanding of the strain propagating throughout a mechanism, this

reading does not deliver. Much like the previous paper, this study only provides data on the motion of one point on a mechanism as opposed to assessing the entire body of the mechanism. This would make sense as the purpose of this reading is not to assess the response of a compliant mechanism but rather to assess the accuracy of their measuring method. This is still proof that further research into the preserve region is required.

2.6.4.3 High-precision displacement measurement method for three degrees

Similarly to Yao et al. [55], Wu et al. [56] proposed a method to also improve displacement calculation using computer micro-vision. Wu et al., however, instead of using an optical flow technique, used a combined ring project and pseudo-Zernike method. They found experimentally that their proposed algorithm was effective at measuring the displacement, being far more accurate than the light interferometer measurement (LIM) used for comparison.

Although their proposed algorithm was very effective at measuring the point displacements of compliant mechanisms, the goal of this paper does not fill the knowledge gap that this thesis intends to investigate. This paper goes into impressive depth behind the algorithms and the calculations being done during the processing of data. However, the experiment only investigated one specimen as well as only the displacement of one point. The paper does not explore the theory and mathematical modelling of compliant mechanisms, as it was not so much an investigation of the response of compliant mechanisms as much as the accuracy of their newly proposed method.

2.7 Summary

Compliant mechanisms have seen a considerable increase in the research surrounding it. Some key observations have been made from investigating the literature. Firstly, there are mainly two mathematical approaches used to model compliant mechanisms: the compliance

matrix method and the pseudo-rigid-body model. With both of these approaches, there is a common assumption between them that lumped compliance compliant mechanisms have flexible sections and rigid sections. This, however, is not the case, as the strain will still be present in sections not categorised as nodes. There has been little consideration for this region, particularly within a theoretical approach. When compliant mechanisms are experimentally tested, researchers often validate their models by measuring only one point. Very rarely is the strain across the entire mechanism discussed. This led to the goal of the thesis, to gain a better understanding of the preserve region present when designing compliant mechanisms with lumped compliance, or more specifically:

- What is the size of the preserve region?
- What shape best describes the preserve region?
- What impact does the preserve region have on the theoretical modelling of compliant mechanisms?
- Can the strain in the preserve region be validated through the use of DIC?

Chapter 3

Method

This chapter covers the method that was used in this research to analyse the preserve region. It covers the approach taken to find the size and shape of the preserve region, as well as quantifying the effect that the preserve region has on the accuracy of the theoretical compliances. To find all this information, an emphasis has been placed on the use of FEA software to measure the accuracy of the theory by isolating parts of the compliant mechanism to gain a better understanding of the impact different regions have on the displacements of the samples.

3.1 Preserve Region Analysis

3.1.1 Single Node Mechanism

To help express the impact of the preserve region, it is best to use a scenario with the least amount of variables that may impact the results. Therefore, a very simple compliant mechanism was designed as a sample scenario to test the accuracy of the theoretical value using FEA. This sample mechanism can be seen in figure 3.1. It involves a single node attached to two sections on the left and right. The section on the left is the fixed end and

was bolted in place. The right section is where the load was applied. Multiple holes were added to the load section, as these were used to find the true compliance values using FEA. The node itself is a rectangular cross-section node with four fillets at each corner. Depending on the geometry analysed, this fillet was either circular or elliptical. For the start of each geometric variation, the whole model was used to find the total error in the mechanism, with the preserve region included.

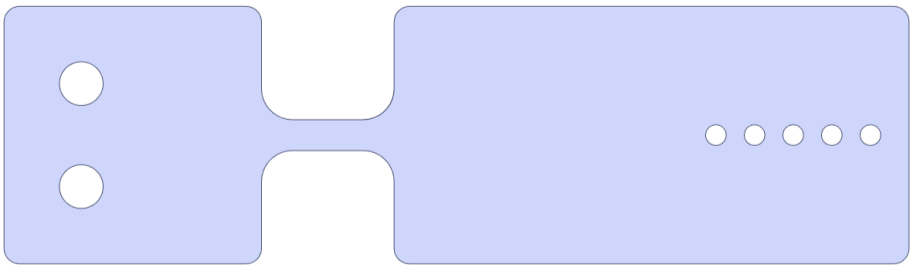

Figure 3.1: *Single node*

3.1.2 Preserve Region Size

This section answers the question about the size of the preserve region, or in essence, where the mechanism can truly be considered rigid and when it is still considered to be flexible. To answer this question, manipulation of the FEA model in figure 3.1 was used.

The first model made is in figure 3.2. The goal of this model was to see how accurate the theory is in the best-case scenario if there was truly no preserve region acting on the system. This model was made by taking the model seen in figure 3.1 and removing the left side where it was fixed. This allows the end of the node to be truly fixed, as the theory assumes it to be. Next, the right section was separated from the node, making two different bodies on the model. This allowed the two bodies to have different stiffnesses. This made a flexible body and an effectively rigid body by increasing the stiffness of

the right section to the point where it has no impact on displacement. When using this model, a substantial drop in error is expected as the strains present in both supposed rigid sections are removed.

Figure 3.2: *Model with no preserve region*

After the tip displacement was found in the scenario mentioned before, the model was then altered into what is seen in figure 3.3. In this model, instead of completely removing the left side of the model and splitting it at the right node boundary, the flexible region was expanded to include an arc on both the fixed end and the load end. In doing this, more strain can propagate past the node and begin to include parts of the preserve region. As this region is made larger and larger, the error increases. This is due to, as mentioned before, the inclusion of the preserve region in the loading scenario. Increasing and decreasing the size of this flexible region was how the size of the preserve region was determined. For the sake of the research done, the model was considered rigid once the flexible region was large enough that it included 80% of the error between the node-only model to the full model.

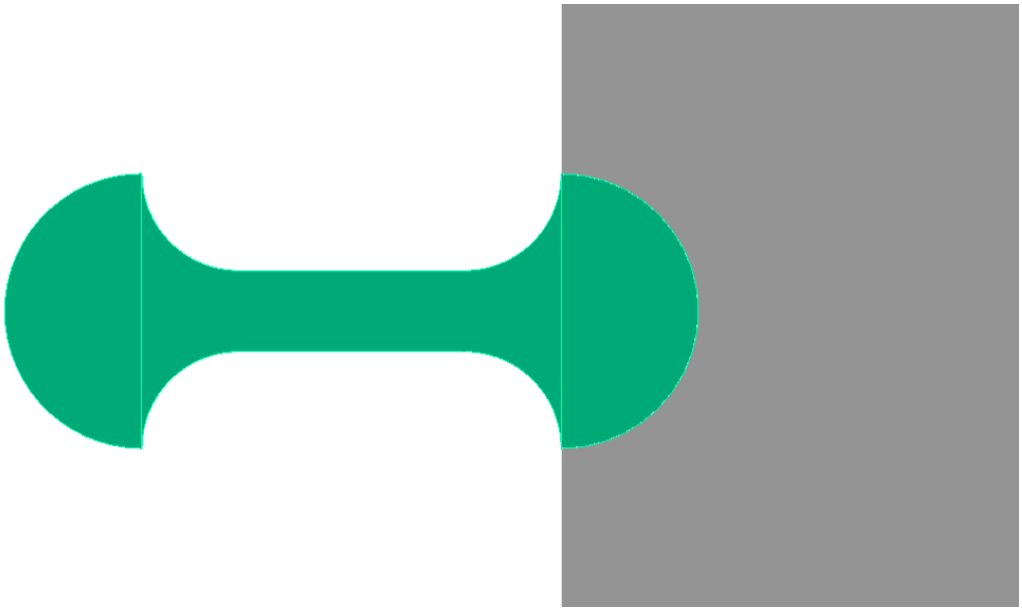

Figure 3.3: *Model with preserve region*

3.1.3 Preserve Region Shape

The next part of the analysis for each of the geometric configurations was finding a more refined shape to define the preserve region. In the previous section, an arc was used to describe the size of the preserve region, as it is a simple shape with only one variable. However, looking at figure 3.4, it is fairly clear that the shape does not resemble that of an arc. From a purely observational standpoint, the shape seems to take on a more elliptical shape when propagating past the node. Therefore, after the size of each of the preserve regions was found, a shape that better fits the strain propagation was also found. A shape is considered to fit the preserve region better if there is less variation in strain values along the line of the boundary.

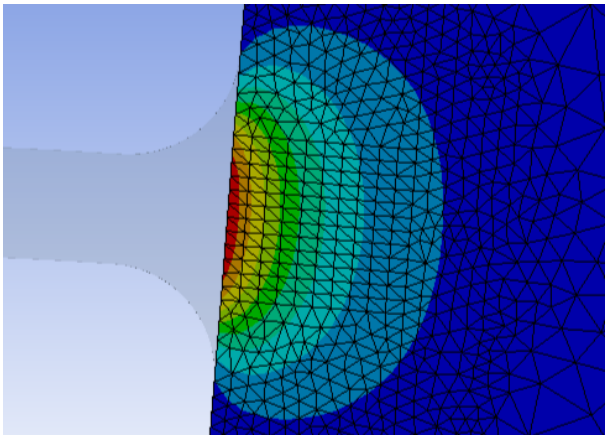

Figure 3.4: *Preserve region strain map*

To find the most suitable shape for the ellipse, an ellipse-fitting script was used [57]. It takes a set of coordinates and generates an ellipse that best fits those values, defining the major axis (A), minor axis (B) and centre (X0, Y0). This script was used in conjunction with a set of points where the strain is constant to find a shape that best describes the preserve region boundary. When selecting the value of strain that this boundary must adhere to, the largest value of strain along the arc that defines the size of the preserve region was used.

The model setup for the preserve region shape analysis can be seen in figure 3.5. It consists of an arc with multiple vertical lines as well as a horizontal line in the centre of the arc. All of these lines force the FEA software to place nodes along them. It also allows a strain probe to be placed along the line to see how the strain changes. All of the strain values from the vertical lines were then extracted and moved to an Excel spreadsheet, where the vertical destination of the node with a strain closest to the target value was found. If the nearest value of strain was more than 10% out, the simulation would be redone with a finer mesh, and if the value was between 5 and 10% out, a simple interpolation of the vertical distance was used. If the value is within 5% of the target strain value, it was considered to be the correct location.

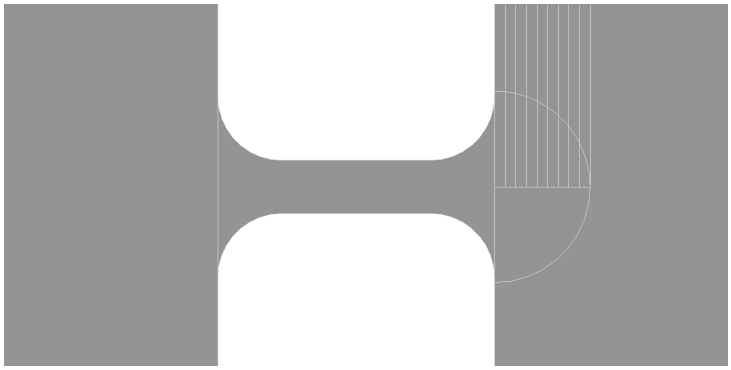

Figure 3.5: *Model setup for shape analysis*

The distance from the vertical line to the node is considered to be the x coordinate in the ellipse fitting function, while the height of the node extracted is considered the y coordinate. The horizontal line in the centre gives an x coordinate when the y coordinate is 0. In figure 3.6a, an example of the coordinates extracted can be seen. Using the elliptical fitting script, the shape is output in the form of figure 3.6b.

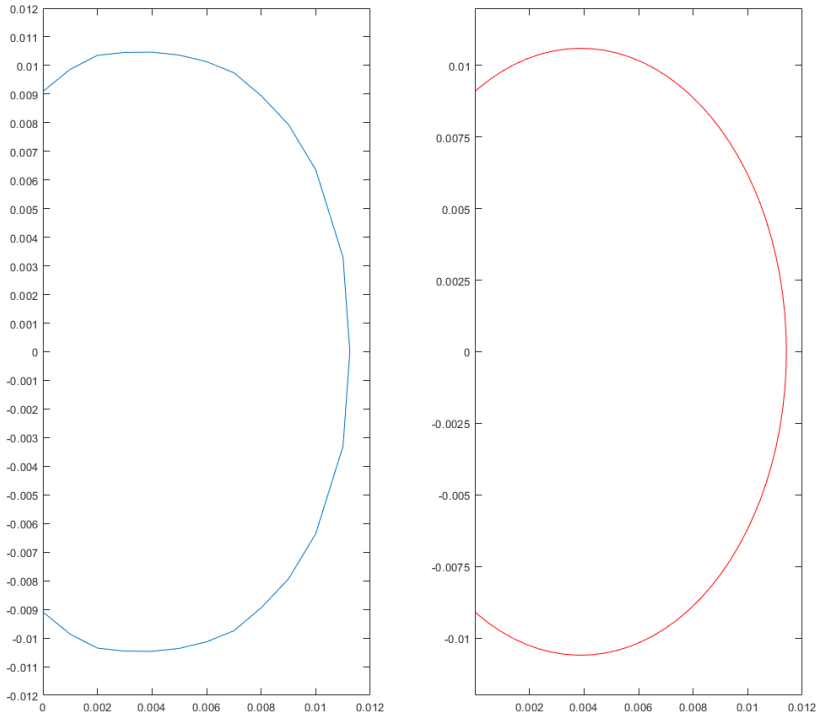

(a) ***(b)***

Figure 3.6: *Ellipse fitting a) Raw coordinates extracted b) Elliptically fitted coordinates*

To ensure that this shape accurately describes the preserve region, a final step was involved to verify. In figure 3.7, the models used to verify the accuracy of the shapes can be seen. The first model was used to see the variation in strain values. Much like in figure 3.5, the strain along the elliptical line is measured, and the variance in values is noted. The second model was used to verify that the amount of error in this shape is the same as the error found when it was described as an arc. This was done by separating the model into a flexible body and a rigid body (much like in figure 3.1.2). The flexible section encompasses the node as well as the now elliptical preserve region. The tip displacement value of this new flexible region was compared to the tip displacement using the arc found in the size analysis. In testing, the error between the elliptical shape and the arc shape never exceeded a value of 0.3%.

Figure 3.7: *Shape verification*

3.1.4 Effective Compliance

Finding the effect that the preserve region has involved an analysis of the setup using a full model with a full mesh. As seen in figure 3.8, the mechanism was fixed in place by the two holes on the left, and the load was applied to the holes on the right. The goal of this step was to establish the mechanism's true or "effective" compliance. This involved applying loads in different areas and measuring the displacements and rotations at different points to conclude what the compliance was with the preserve region included. Following will be the process used to find each of the compliances in the compliance matrix after the translation. After the translated compliances are found, they must be translated back to find the effective compliance of the node.

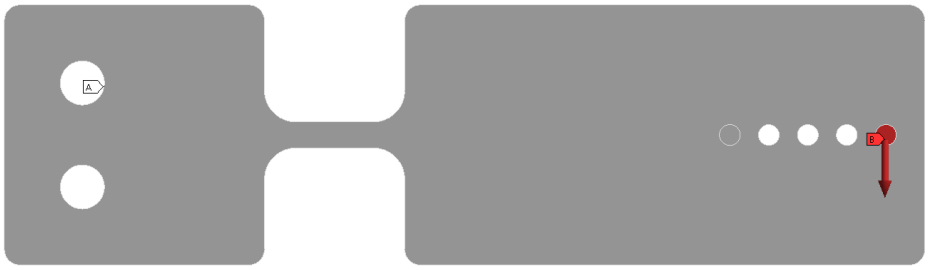

Figure 3.8: *Full model loading*

C_{ux-fx}

For the analysis performed, the compliance in the x direction due to a force in the x direction was assumed to remain the same as the theory. This is due to this compliance not contributing to the displacement in the given loading scenario.

C_{uy-fy}

The effective compliance in the y direction due to a force in the y direction was found by applying a load at one of the holes on the mechanism and measuring the displacement of the point where the force was applied. The compliance was then found by dividing the displacement in the y direction by the force in the y direction.

C_{uy-mz}

Quantifying the true compliance in the y direction due to a moment in the z direction was more involved. To achieve a moment about the z direction, a force was applied offset from the reference point O. This induced a y displacement about O due to the moment generated from the load. However, there was also a y displacement induced due to a force in the y direction at O. This led to the following force matrix about O:

$$\begin{bmatrix} 0 & Fy & D \cdot Fy \end{bmatrix} \tag{3.1}$$

An issue arose when quantifying the y displacement due to the moment, as it was not clear which portion of the y displacement was due to the force in the y direction and which portion was due to the moment about the z direction. This can be resolved by taking the compliance in the y direction due to a force in the y direction found in the previous section and multiplying it by the load. Since:

$$\begin{bmatrix} ux & uy & \theta z \end{bmatrix} = \begin{bmatrix} C_{ux-fx} & 0 & 0 \\ 0 & C_{uy-fy} & C_{uy-mz} \\ 0 & C_{uy-mz} & C_{\theta z-mz} \end{bmatrix} \cdot \begin{bmatrix} 0 & Fy & D \cdot Fy \end{bmatrix} \tag{3.2}$$

$$uy = C_{uy-fy} \cdot Fy + C_{uy-mz} \cdot D \cdot Fy \tag{3.3}$$

$$C_{uy-mz} = \frac{uy - C_{uy-fy} \cdot Fy}{D \cdot Fy}$$

As uy and D can be measured on Ansys and Fy is an input variable, using C_{uy-fy} from the previous part of the method, the compliance in the y direction due to a moment about the z direction can be found

$C_{\theta z-mz}$

Determining the angular compliance about the z direction due to a moment about the z direction required some manipulation of the equations as well. As mentioned before, this compliance refers to the change in angle per Newton meter of moment about the z axis, or $C_{\theta z-mz} = \frac{\Delta\theta z}{mz}$. The issue arises because, in a loading scenario, when a moment is present due to an offset load, the force also contributes to the angular deformation of the mechanism. As the compliance in the y direction due to a moment about the z axis has already been found in the previous section, and since $C_{uy-mz} = C_{\theta z-Fy}$, this value was used for isolating the impact that the angular compliance in the z direction due to a moment about the z direction has. Two loading scenarios were used to isolate the impact that the moment has on the angular deformation. The first loading scenario was where the load Fy was directly on the reference point O. O is $L1$ meters from the end of the node. In this scenario, there was no angular deformation due to a moment as there is no moment. This value of angular deflection was measured using a probe in Ansys and is labelled $\theta z1$. The second loading scenario was when the load Fy is applied $L2$ meters from the end of the node and offset from the O. The angular deformation was also measured using a probe and is labelled $\theta z2$. With all these variables, the following equation was found.

$$\begin{bmatrix} ux & uy & \theta z \end{bmatrix} = \begin{bmatrix} C_{ux-fx} & 0 & 0 \\ 0 & C_{uy-fy} & C_{uy-mz} \\ 0 & C_{uy-mz} & C_{\theta z-mz} \end{bmatrix} \cdot \begin{bmatrix} 0 & Fy & D \cdot Fy \end{bmatrix} \tag{3.4}$$

$$\theta z = C_{uy-mz} \cdot Fy + C_{\theta z-mz} \cdot D \cdot Fy \tag{3.5}$$

After this process has been completed, the result is the compliance matrix of the mechanism after the translation. Getting this matrix by measuring the responses using FEA means that this compliance matrix includes the compliance gained from the preserve

region. This matrix, however, is specifically about O, offset from the node. This means that this compliance matrix in its current form needed to be translated back to the node allowing the true compliance matrix of the node to be found. This true value of compliance will be more accurate than the compliance found using the theory alone, as it encompassed the preserve region as well. The equation for finding the true compliance matrix of the node was found using the following method:

$$[C^t] = [T]^T \cdot [C^n] \cdot [T]$$

$$\begin{bmatrix} C^t_{ux-fx} & 0 & 0 \\ 0 & C^t_{uy-fy} & C^t_{uy-mz} \\ 0 & C^t_{uy-mz} & C^t_{\theta z-mz} \end{bmatrix} = \begin{bmatrix} 1 & 0 & 0 \\ 0 & 1 & -\Delta x \\ 0 & 0 & 1 \end{bmatrix} \cdot \begin{bmatrix} C^n_{ux-fx} & 0 & 0 \\ 0 & C^n_{uy-fy} & C^n_{uy-mz} \\ 0 & C^n_{uy-mz} & C^n_{\theta z-mz} \end{bmatrix} \cdot \begin{bmatrix} 1 & 0 & 0 \\ 0 & 1 & 0 \\ 0 & -\Delta x & 1 \end{bmatrix}$$

$$C^t_{uy-fy} = C^n_{uy-fy} - 2C^n_{uy-mz} \cdot \Delta x + C^n_{\theta z-mz} \cdot x^2 \tag{3.6}$$

$$C^t_{uy-mz} = C^n_{uy-mz} - C^n_{\theta z-mz} \cdot \Delta x \tag{3.7}$$

$$C^t_{\theta z-mz} = C^n_{\theta z-mz} \tag{3.8}$$

The above matrix of equations can then be rearranged to find the true compliances of the node. These values were compared and contrasted to the value expected to be seen by the theory and were found for varying geometries to see if a trend formed between the change in certain dimensions and the change in certain compliances.

3.2 FEA Validation

As many of the conclusions were drawn through the use of FEA simulations, experimental data was needed to see if they were true for practical applications. Seeing as these conclusions were heavily related to the way strain propagated past the node, it would

prove very useful to have a type of testing that can analyse strain across an area of a sample. It is for this reason that digital image correlation (DIC) was used. DIC allows for a full 2D analysis of strain across a sample. It also allows strain values to be extracted from the different points on that sample.

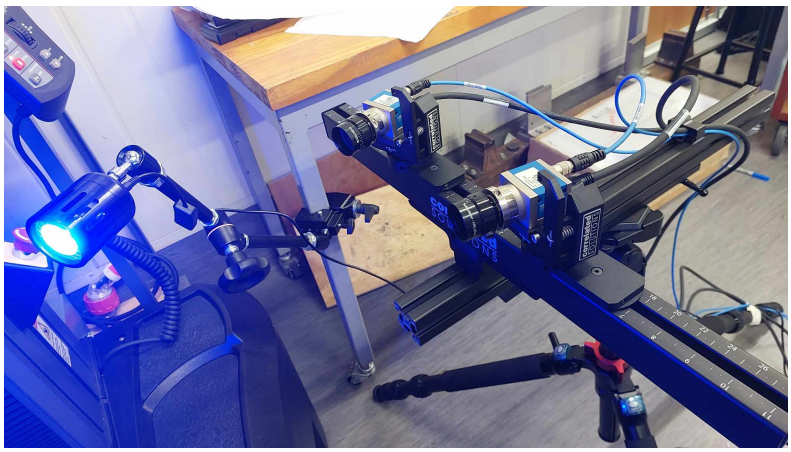

Figure 3.9: *Digital image correlation setup*

3.2.1 Experimental Samples

The samples that were used with the DIC system were similar to those used in the FEA. In total, there were four different samples tested. These mechanisms were modelled in SolidWorks, after which they were used in Ansys to acquire the FEA results. The models were then cut from a 10mm thick sheet of polypropylene using a CNC mill for experimental testing. Polypropylene was selected as the material as it is one of the best materials to make compliant mechanisms from and also due to its availability and ease of manufacture. These cut parts were then spray painted and speckled to be used with the DIC setup. The strain values across the preserve region were analysed and compared.

The first type of node investigated was the circular hinge, as seen in figure 3.10a. This refers to a node type that has a varying thickness that is represented by a circle. This type of node only has two geometrical variables to consider: the radius of the circle (R) and the minimum thickness of the node (T). The radius of the circle affects both the fillet size and the length of the node.

The second type was the circular filleted node and can be seen in figure 3.10b. This is very similar to the circular hinge. However, it also includes a flat section in the middle where the node is rectangular. This node shape is very common and, therefore, was the baseline for many of the results during the preserve region analysis. This node shape contains three different geometrical variables that can be considered: the length of the node (Ln), the minimum thickness of the node (T) and the radius of the fillet (R).

The third type of node was the elliptical hinge, which can be seen in figure 3.10c. This node varies in thickness in the shape of an ellipse. With the previous two analyses, when changing the radius of both the circular hinge and the fillets on the circular filleted node leads to both an increase in the overall thickness of the node as well as an increase in the thickness of the interface between the node region and the rigid region. Investigating an elliptical shape allowed conclusions to be drawn about whether the impact a circular fillet has on the accuracy of the results is due to just an overall thicker sample or due to the different sizes of the interface between regions. With this node, there are three main geometrical values that can be adjusted: the minimum thickness of the node (T), the major axis of the ellipse (A) and the minor axis of the ellipse (B). Similarly to the circular hinge, the length of the node is dependent on the size of the major axis of the ellipse, making it unclear if any changes in accuracy are due to the increase in length of the node or due to the change in the value of the major axis.

The final node geometry investigated was the elliptically filleted node and is shown in figure 3.10d. For the same reason both the circular hinge and the circular filleted hinge are investigated, the elliptically filleted hinge allows the impact the major axis has on accuracy to be isolated by including a flat section in the centre of the node. This node has the most possible variables worth analysing, that being the length of the node (Ln), the minimum thickness of the node (T), the major axis of the fillet (A) and the minor axis of the fillet (B).

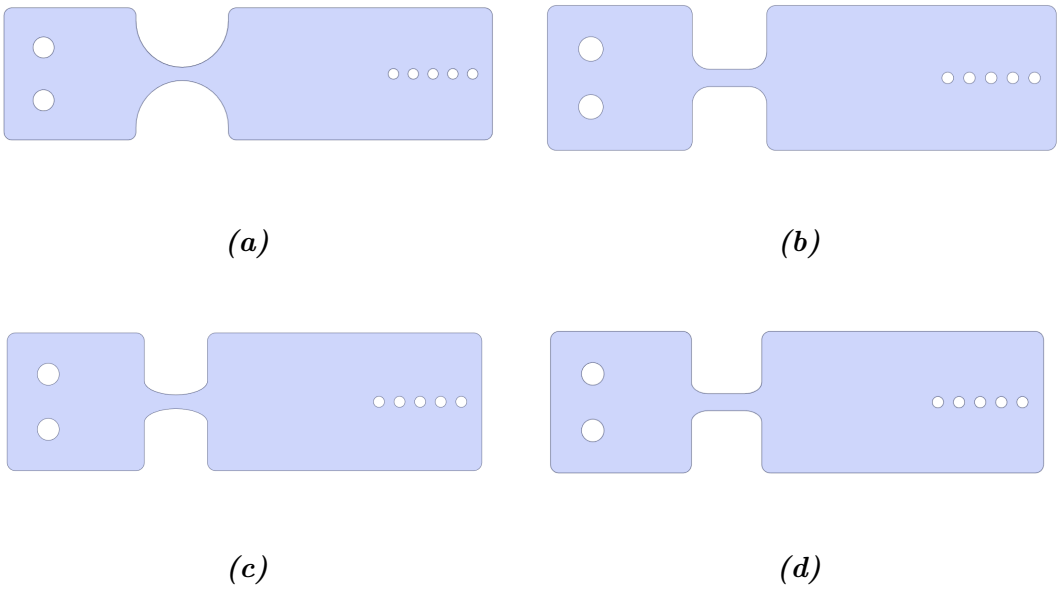

Figure 3.10: *Key node geometries analysed: a) Circular hinge b) Circular filleted hinge c) Elliptical hinge d) Elliptically filleted hinge*

To help gain an understanding of how the type of geometry can impact the accuracy of the results, the sample's dimensions were carefully considered. When deciding on specific geometries, the first mechanism designed was the circular hinge mechanism. This was used as a baseline for all the other geometric configurations, as this one had the least amount of variables that could be changed, allowing for more freedom when making all the samples. For this configuration, a circular hinge with a radius of 17.5mm and a minimum thickness of 5mm was decided upon. These geometries were selected as they allowed for a substantial amount of tip displacement while maintaining a maximum stress value that is below the yield stress of polypropylene.

With this baseline mechanism designed, the compliances were theoretically calculated using the method mentioned in section 2.1.1. The compliance in the y direction due to a force in the y direction was then selected as the target value. This target value is what the other geometric configurations try to achieve. To do this, each geometric configuration had a geometric variable that was set as unknown. Having one geometry unknown but knowing what the compliance of the mechanism must be, means that there is only 1

unknown variable. This means that instead of solving the compliance equation for C_{y-fy}, the equation is now solved for an unknown geometry for each node type.

Table 3.1: Unknown dimensions values

Geometric Configuration	Unknown Variable	Value (mm)
Circular hinge	Radius (R)	17.5
Circular filleted	Node Length (Ln)	25.75
Elliptical hinge	Major Axis (A)	11.5
Elliptical hinge	Node Length (Ln)	24.95

The remaining dimensions were as follows. The circular filleted node had a thickness of 6mm and a radius of 6mm. The elliptically filleted node had a thickness of 6mm, a major axis of 6mm and a minor axis of 4mm and the elliptical hinge had a thickness of 5mm and a minor axis of 5mm.

All of these nodes mentioned above theoretically have a compliance of 6.28E-4 after being translated to point O. This means that, in theory, all of them should displace 3.01 millimetres due to a force of 4.8N in the y direction. In the results section, observations were made into how each of the types of geometric configurations differed in results.

3.2.2 Experimental Setup

To compare the results from the FEA to DIC, a means of applying the load is required. It is for this reason that a testing rig was designed to apply a force accurately to the samples discussed in section 3.2.1.

In figure 3.11, the rig used to test the samples can be seen. It used minitec cross sections to allow for the testing sample to be elevated above the bench. The samples were bolted onto the minitec with washers between the sample and the rig to ensure that there was no friction present. The sample then had a weight placed on the end of 500g. The reason weights were used is to try to minimise the effect of creep by loading the samples instantaneously as opposed to gradually.

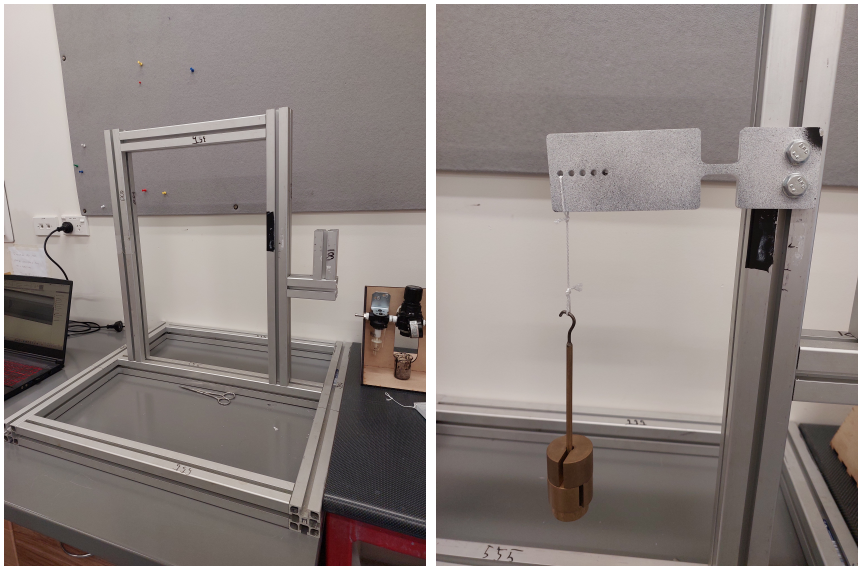

Figure 3.11: *Testing rig*

3.2.3 DIC Method

3.2.3.1 Sample Preparation

Before data was collected, the samples needed to be prepared. For digital image correlation to function properly, it requires a non-recurring, highly contrasted pattern. This is usually in the form of a speckle pattern. This speckle pattern consists of a white base on the sample and black dots painted on top of it. For the samples used in this research, a white primer was put onto the sample surface, and then a matte white spray paint was put on top of that. This acted as the white background for the test images. To speckle a sample, a roller is often used that imprints a speckle pattern with black ink. For the samples proposed for this research, however, the area being analysed is too small relative to the roller speckle pattern. This leads to dots on the sample that are too large, reducing the accuracy of the results. This was why a different method of speckling was used in the form of black spray paint. Using a can of spray paint from a distance allows black dots to appear across the surface of the sample in a non-recurring pattern. The results can be seen in figure 3.12, a non-recurring, high-contrast speckle pattern.

Figure 3.12: *Speckled sample*

3.2.3.2 Image Analysis

Image collection was done by taking an image every 200 milliseconds over 10 seconds of the sample loading. The speckled sample was first placed in the testing rig in front of the cameras. The recording then began, and the weights were placed on the sample. After the images were taken, they were moved into the image analysis software VIC-3D to analyse the strain across the sample.

The goal of analysing the images was to find information that can be easily compared to that of the FEA simulation. To get this data, the Area of Interest (AOI) was used on the VIC-3D software. To start with, the AOI was drawn to measure data at the tip of the mechanism. This was used to compare the tip displacements seen on the FEA compared to the DIC. The AOI was changed to measure data around the preserve region. This provided a strain field of the preserve region, showing the shape of the strain propagation. This was recreated in FEA as shown in figure 3.13, and observations were made. This part of validating the FEA was purely observational in that the strain maps were compared, and the similarities were commented on. To quantify the differences in DIC to FEA results, individual lines of strain were measured.

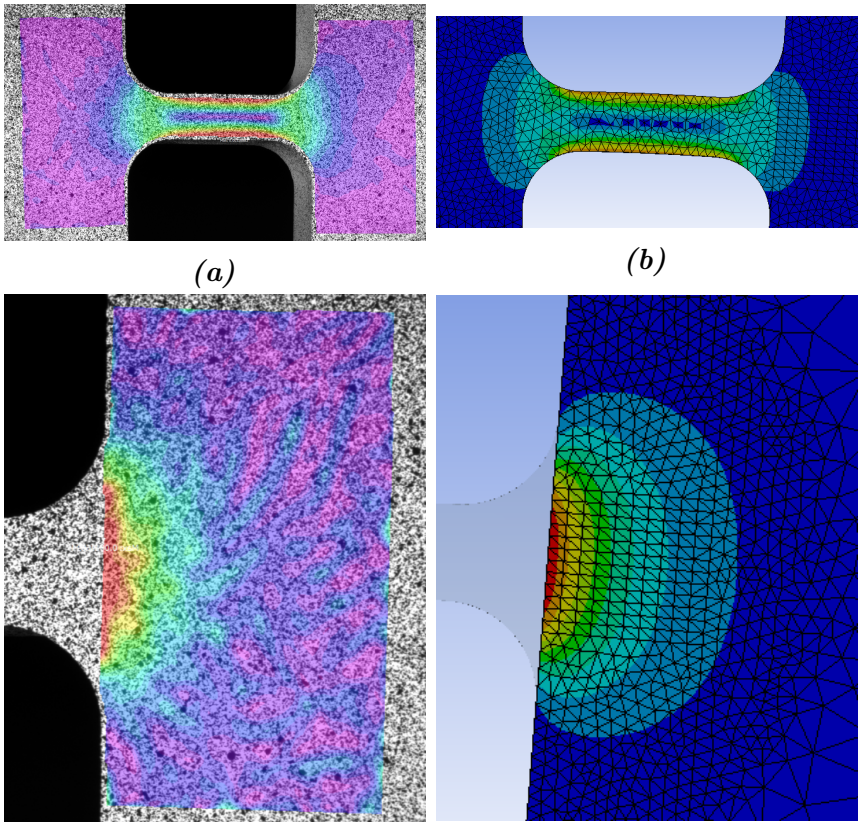

Figure 3.13: *Image analysis: a) AOI node inclusive b) FEA node inclusive c) AOI preserve region d) FEA preserve region*

To quantify the error in the FEA, the analysis was narrowed. Instead of using an area of interest to observe the strain, a series of lines were placed on the DIC analysis, and the strain was measured along these lines. A line of nodes was drawn on FEA in the same location, and the variation between the two was observed. This set of horizontal lines was drawn on VIC-3D. The location of the lines was verified by looking at their x and y coordinates on the software and ensuring that the horizontal lines were the correct distance apart and the correct horizontal length. For all the samples, a spacing of 1.5 mm was used between the lines to grant an image of how the strain looks over a wide area in the preserve region, with the only exception being the circular hinge as the boundary between the node and the preserve region was so large that a line was placed every 2 millimetres. A strain value was taken from these lines every millimeter for 10 millimeters, giving 10 data points for each horizontal line. As there was a substantial amount of noise

in this test, the average value of strain at these points was taken over 20 images after the loading had occurred. This set of lines was recreated on FEA, and the strain was measured along them to see how similar they were to the experimental data.

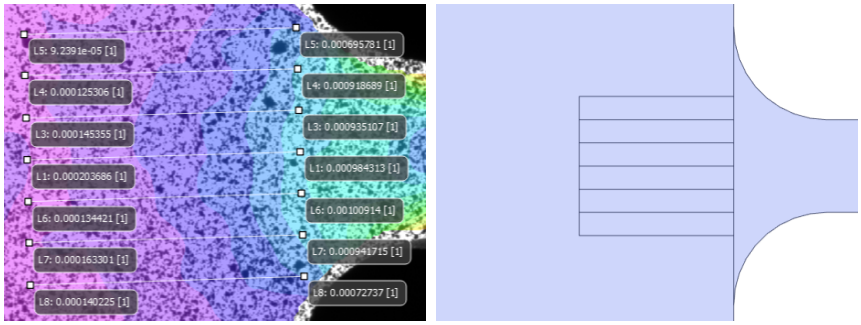

(a) ***(b)***

Figure 3.14: *Strain measurement*
a) Horizontal line analysed (DIC) b) Horizontal line analysed (FEA)

To ensure that the parameters used in the simulations are correct, dogbone samples were made from the polypropylene used for the samples to test for the material stiffness. Another parameter that is important to know is the Poisson's ratio of the material. There was no readily available equipment to find this value, so a value was used from other research [58]. The dogbone dimensions were by the ASTM standard for a plastic sample with a thickness of 10mm [59]. The dogbones were placed in an Instron tensile tester, and the stiffness was found.

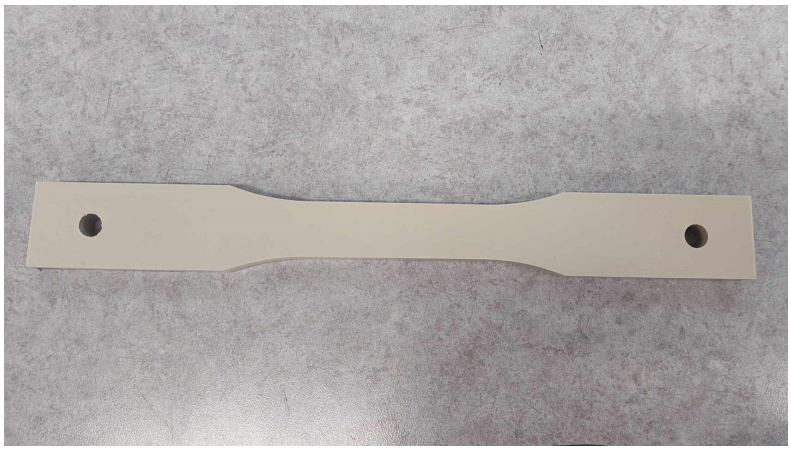

Figure 3.15: *Dog bone sample*

Chapter 4

Results and Discussion

This chapter presents the results collected using the method described in Chapter 3. It began with a sensitivity analysis to help gain an understanding of key variables that have a noteworthy impact on the error. It was then followed by the in-depth preserve region analysis, where these sources of error were isolated and analysed. Finally, the FEA was validated using DIC to verify strain values found on Ansys to help ensure the data found was true.

4.1 Sensitivity Analysis

Before the in-depth analysis of the preserve region, a study was undertaken to understand the impact that varying key node geometries have on the accuracy of the theory compared to FEA. To do this, a Matlab script was written that finds the change in tip displacement of the sample shown in figure 3.1 when changing certain dimensions. These dimensions were then recreated on Ansys and were used to verify the accuracy of the calculations. The results from this analysis granted insight into which variables are likely going to impact the preserve region and which do not need consideration, by viewing their impact on the error as a whole.

4.1.1 Length and Thickness

A circular filleted sample with a fillet radius of 6mm and a width of 10mm was used. The length was set to 17mm and increased in 1mm increments until it reached 25mm. This range of values was then repeated at thicknesses starting at 4mm and growing also by 1mm until it reached 8mm. The load was set to 10N at an offset of 92.5mm, and the stiffness was set to 1.725 GPa.

Figure 4.1 shows the errors for different combinations of lengths and thicknesses. Decreasing the thickness and increasing the length led to a larger displacement at the tip. Looking at the differences between the theory and the FEA some observations can be made. The changes in relative error in figure 4.1b show the thickness of the sample to increase the amount of error between FEA and the theory, increasing from 9.52% to 27.71% from 4mm to 8mm at a node length of 17mm. Looking at the change in relative error about length, the longer nodes have a lower amount of relative error, decreasing from 9.52% to 4.66% when the length was increased from 17mm to 25mm.

Looking at the results in terms of absolute error shows a different relationship. As can be seen in figure 4.1c, when the thickness is kept the same, and only the length is increased, the absolute error does not change. This means that the reason relative error is decreasing with the increase of length is due solely to the fact that with a longer node, the tip displacement will be greater. This increased displacement means the error that is present is a smaller portion of the overall displacement. This same graph shows that the change in the thickness of the sample technically reduces the absolute error present. However, this reduction is far less than the reduction of the overall tip displacement, resulting in a severe impact on relative error.

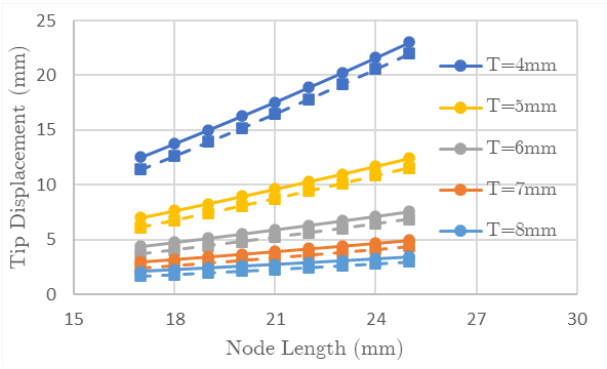

(a)

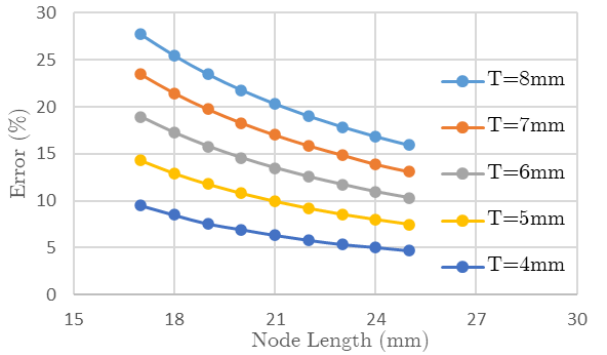

(b)

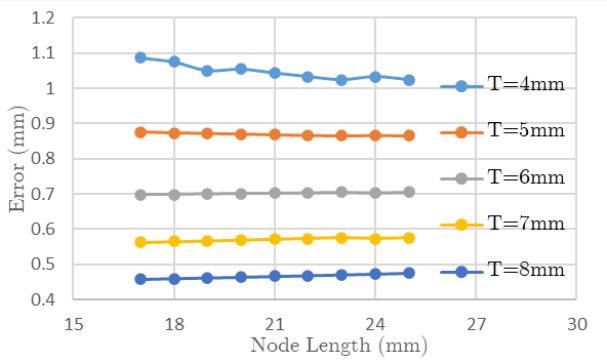

(c)

Figure 4.1: *Tip displacement as thickness and length varies: a) FEA and theoretical results b) Relative error c) Absolute error*

Using these results already granted insight into what variables impact the preserve region. As mentioned in the method, during the in-depth analysis of the preserve region, the size is defined by where most of the total absolute error is encompassed. Therefore, altering the length should have a very similar preserve region, as the absolute amount of error remained the same. For thickness, there are likely going to be some changes to the preserve region, as there is an impact on the absolute error when changing this variable.

4.1.2 Load offset distance

This section investigated the impact the load offset has on the accuracy. To test this, a circular hinge node was used, with a minimum thickness of 5mm and a radius varying from 7.5mm to 17.5mm, increasing in increments of 2.5mm. For each of the radii, 5 different offset distances were used. This refers to the distance from the end of the node to the location where the load of 10N was set. These offset distances were between 62.5mm to 92.5mm, increasing in increments of 7.5mm. A circular hinge was selected as changing the radius of the hinge impacts 3 different aspects of the node, that being its length, overall thickness and fillets. This means that if there is a compounding effect, e.g. if changing the offset distance has a different effect at different combinations of lengths and thicknesses, it would be seen. However, if there is no change in the effect the offset distance has over different radii, it would be clear that it has no effect.

The graphs in figure 4.2 show the relationship between the FEA results and the theoretical results as the offset distance was altered. As the offset distance increases the tip displacement also increases. This is due to the load being further away, causing a larger bending moment and, therefore, a larger displacement at the tip. Looking at the relative error, there is only a very minor increase as the offset distance increases, increasing 7.95% to 8.63% for a 17.5mm radius hinge. This minor increase is likely because moving the load further down the mechanism leads to more material experiencing strain in the FEA. This extra strain is not accounted for in the theory.

The graph showing the absolute error in figure 4.2c showed that as the offset increases the absolute value of error also increases. However, as mentioned before, the relative error remained nearly the same. This implies that the impact of the offset distance is negligible as it simply increases both the strain inside and outside the node at the same rate.

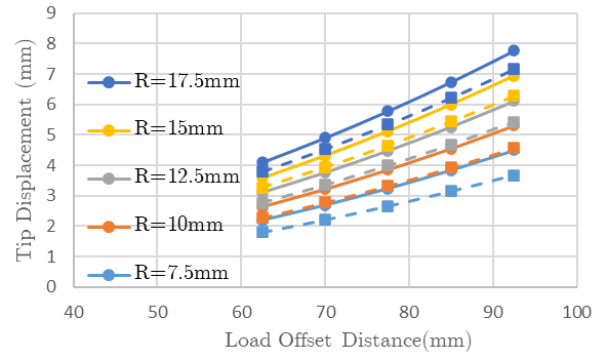

(a)

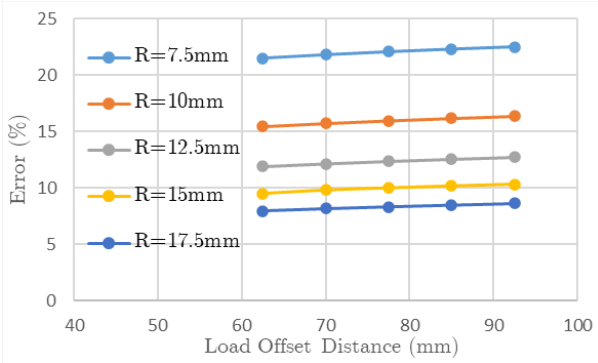

(b)

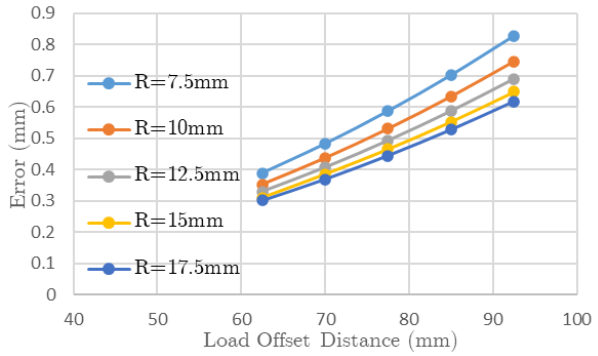

(c)

Figure 4.2: *Tip displacement as offset distance and radius varies: a) FEA and theoretical results b) Relative error c) Absolute error*

4.1.3 Fillet Variation

This section covered the impact that changing the fillet has on the accuracy of results. This encompasses both elliptical fillets (fillets with a different major and minor axis) and circular fillets (fillets where the major and minor axes are equal). The dimensions that

remained constant were the width at 10mm, the thickness at 6mm and the length of the node at 25mm. The fillets began with the major axis at 2mm and increased to 8mm in increments of 1mm. For each value of the major axis, the minor axis was also varied from 2mm to 8mm in increments of 1mm. For the circular fillet dimensions, the values where the major and minor axes were equal were extracted and analysed.

4.1.3.1 Elliptical Variation

Figure 4.3 shows the results from the elliptical testing. Similar to varying the thickness, increasing either the minor or major axis leads to a decrease in tip displacement. The relationship between these variables and the error is more interesting than in previous sections. Looking at the graph in 4.3b, the relative error of these geometries can be seen. As a whole, increasing the size of the major axis up to a point reduces the error, whilst increasing the minor axis increases the error. When the major axis is increased from 2mm to 8mm at a minor axis value of 6mm, the error improved from 11.76% to 9.36%, a difference of 2.4%. It is worth noting that each millimeter of change in the major axis has a far more substantial effect at lower values. From a 2mm to a 3mm major axis for the same minor axis value, the error was reduced by 0.86%, while increasing the major axis from 7mm to 8mm only saw an error reduction of 0.06%. This is because, at these very low values for the major axis, it begins to resemble a sharp corner, causing stress concentration and, therefore, a larger amount of error. It is likely this concept of stress concentration that causes the interesting trend seen when varying the minor axis as well. When the minor axis is increased, for all the sizes of the major axes tested, it initially decreases the error. for a 6mm major axis, the error reduced from 9.41% to 9.10%. Immediately after this value, the error begins to increase, going from 9.10% to 9.13%. This means that decreasing the minor axis would also decrease the error. However, if the minor axis is decreased too far, it will cause stress concentration and, therefore, increase the error instead. It should be noted that the cutoff for when the stress concentration begins to increase the error as opposed to reducing it may be subject to the other variables present in the node, as this stress concentration error is more prevalent at higher values of minor

axes depending the size of the major axis.

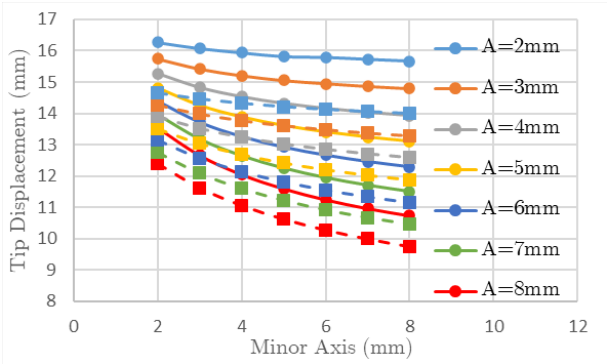

(a)

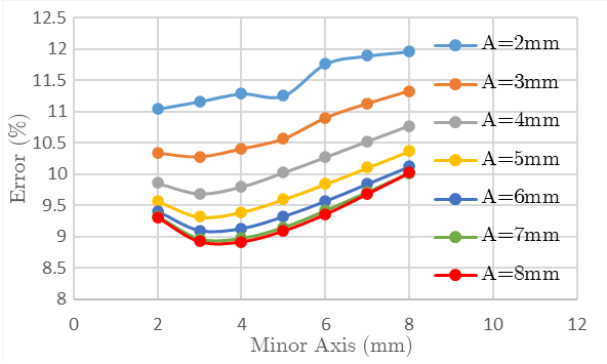

(b)

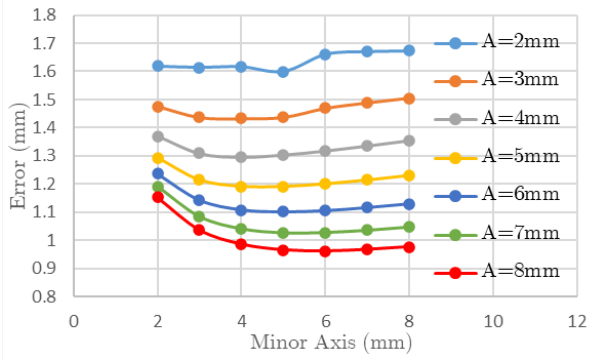

(c)

Figure 4.3: *Tip displacement as major and minor axis varies: a) FEA and theoretical results b) Relative error c) Absolute error*

4.1.3.2 Circular Variation

As circular fillets are a very common choice for node design, an investigation was done on the impact they have on accuracy. The data set for the circular fillet results were

extracted from the previous section 4.1.3.1 where the major and minor axes were the same.

In figure 4.4, the results for circular fillets were extracted. Much like the elliptical fillets, the larger the fillet, the larger the overall thickness, and hence less displacement at the tip. However, looking at the relative error as the radius increases shows an interesting relationship. Initially, the error appears to decrease as the radius increases. However, once the radius reaches 6mm, it begins to increase again. It has been seen in other readings that as the radius of the fillet increases, the error will reduce [6]; however, for these, it was for situations where there was only a node and no other part to the mechanism. This means that the relationship between error and fillet radius may become more complicated with the introduction of a preserve region. What proportion of this error is gained from the preserve region and what is present only in the node will be investigated further in section 4.2

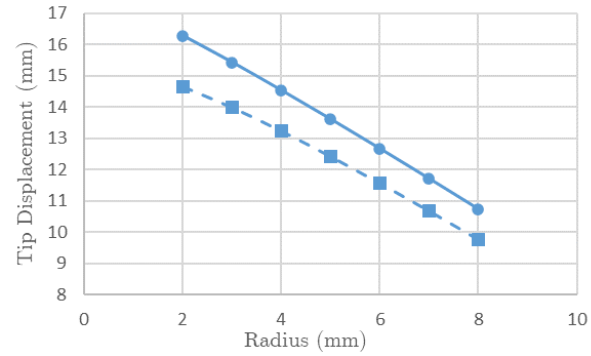

(a)

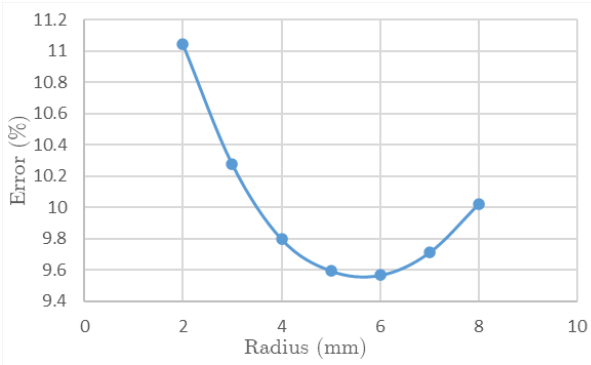

(b)

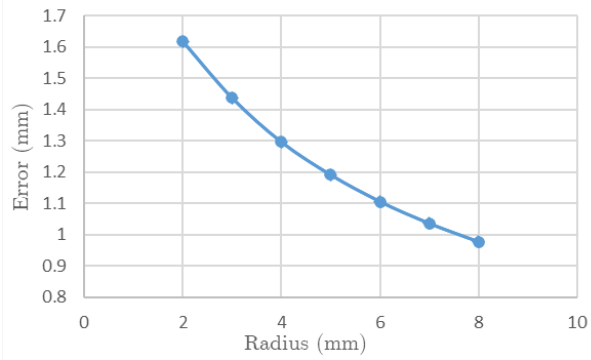

(c)

Figure 4.4: *Tip displacements as fillet radius varies: a) FEA and theoretical results b) Relative error c) Absolute error*

4.1.4 Force and Stiffness

The last two variables that were investigated before the preserve region analysis, were the size of the load and the stiffness of the material. As the goal of the thesis is to provide designers with an understanding and ability to design around the preserve region, if the

load size and material stiffness had a substantial impact on results, the applicability of the conclusions would be far narrower. To test the impact of these two factors, the loads and stiffnesses were altered on FEA over a range of values and the error was assessed between these values and the theory. The values selected were a range of force values from 17.5N to 10N with increments of 2.5N, and a range of stiffness values between 2000MPA and 1000MPA with increments of 250MPA.

When analysing the error as the force and stiffness vary, it was made clear that there is virtually no amount of variation. The force had a max variation of 0.044% and stiffness had a max variation of 0.026%. In figure 4.5, two graphs can be seen. These graphs are the values of strain in a horizontal line past the node. These graphs show that although the strain values are all higher for a higher value of force and a lower value of stiffness, the trend is identical. The reason for this relationship is that increasing the force and decreasing the stiffness increases the amount of strain occurring on all of the points of the mesh. Since all of these points experience the same increase in strain, the impact of any errors from either the preserve region or errors within the nodes does not change, as all the values are increased proportionally. This concluded that force and stiffness did not have any significant impact on the error between the FEA and the theory.

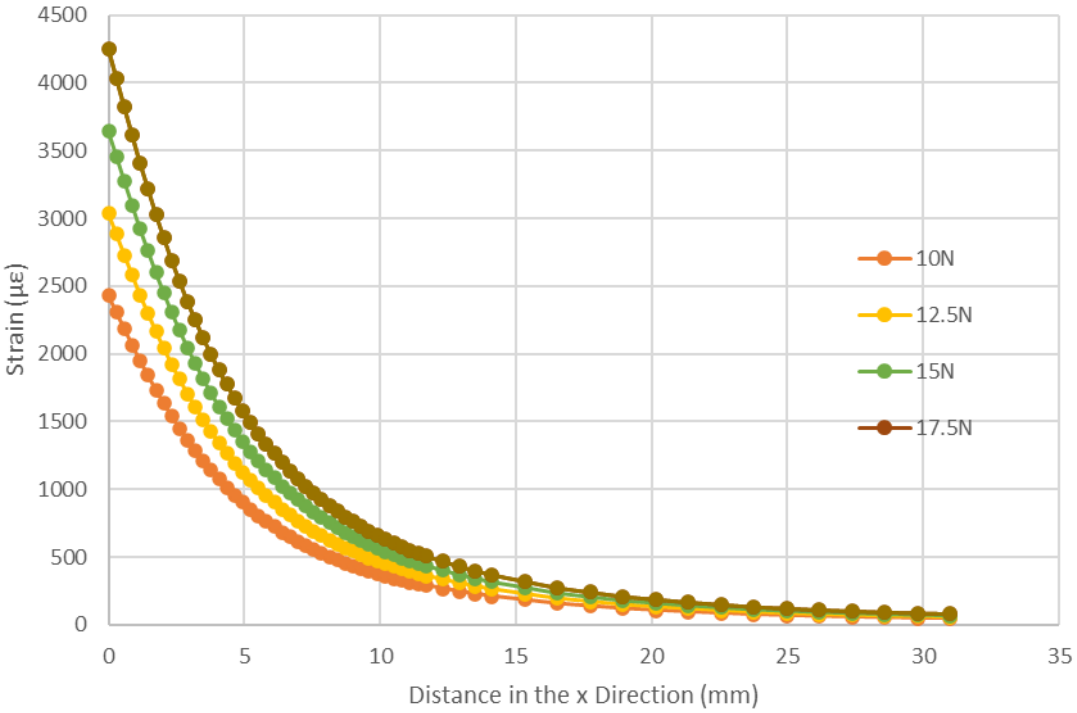

(a)

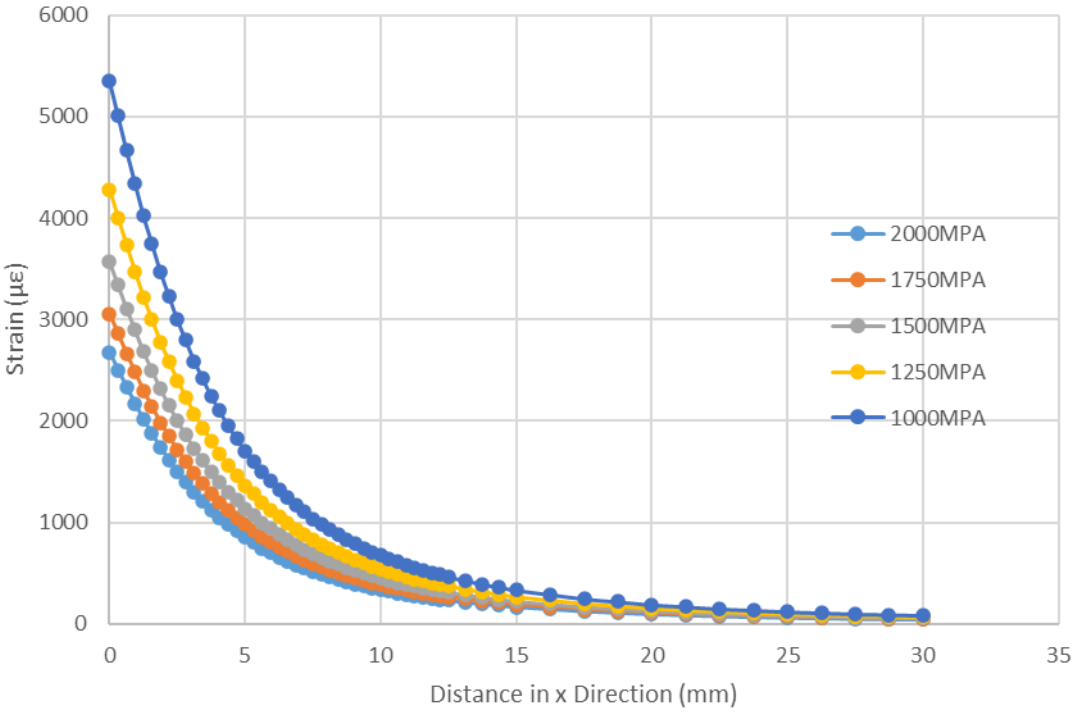

(b)

Figure 4.5: *Strain horizontally outside of node:*
a) as force varies b) as stiffness varies

4.1.5 Sensitivity Analysis Summary

This section of the research proved valuable in helping narrow down what variables to be aware of. From this section, it has been concluded that attributes of the node, such as the thickness and the fillets, can have a noteworthy impact on the error present between the theoretical models and the FEA simulations. As the load offset distance, load size and stiffness of the material had no impact on the relative error of the mechanism, it was excluded from the in-depth preserve region analysis. The length, however, was still included in the analysis, despite the absolute error not changing. This will be to confirm whether or not the preserve region remains identical just like the error did.

4.2 Preserve Region Analysis

This section covered the largest portion of the results. It includes a collection of results from investigating the key variables that are believed to have an impact on the accuracy and the preserve region using the method described in the chapter 3. Each section contains a collection of graphs expressing the change in certain attributes of the preserve region due to altering the geometric variable for the given section.

4.2.1 Length Variation

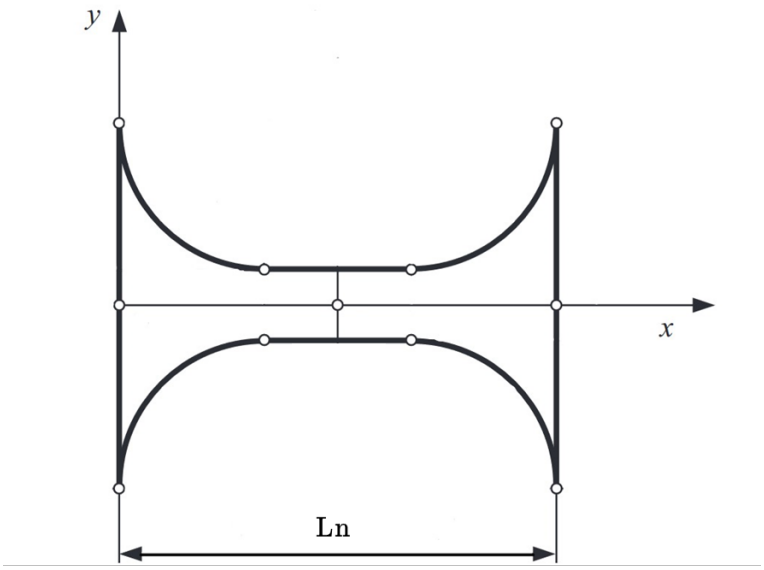

Figure 4.6: *Length labelled*

The first variable analysed is the length of the node. As mentioned in the sensitivity analysis in section 4.1, the expectation was for this variable to not have much effect on the preserve region due to the impact it had on the absolute error. For the testing, the thickness was kept at 5mm, the radius of the circular fillet was kept at 6mm, and the width was 10mm. The material was assumed to be polypropylene with a stiffness of 1.725 GPa. The load was 10N acting down vertically at an offset distance of 92.5mm from the end of the node.

4.2.1.1 Tip Displacements

Figure 4.7 is a set of graphs that grant a deeper insight into the error present when varying the length. As expected from the preliminary investigations, changing the length of the node has very little impact on the absolute error from the preserve region. This can be seen definitively in the graph found in 4.7b, where the sources of error were isolated and the preserve region's error remained constant. There is a very minor increase in absolute error for both the preserve region and the node as the length increases. This

is because increasing the length of the node whilst keeping the load offset distance the same leads to a very slight increase in the moment at the start of the node on the left. This increase in the moment is accounted for in the theory within the node boundary, however, the increase in moment in the preserve region to the left of the node is not. It is important to note, however, that these very slight increases in absolute error are insignificant when compared to the increase in displacement. The absolute error total increases from 1.126mm to 1.173mm, an increase of 4.17%. For this increase in absolute error, the overall tip displacement increased from 11.26mm to 14.22mm, showing the insignificance of the 0.047mm increase.

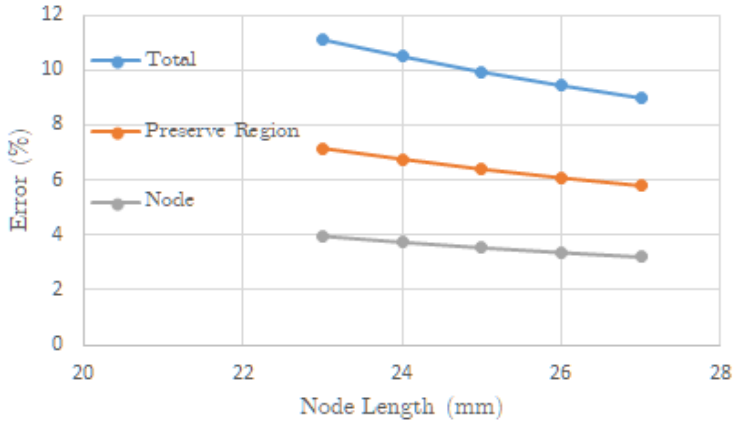

(a)

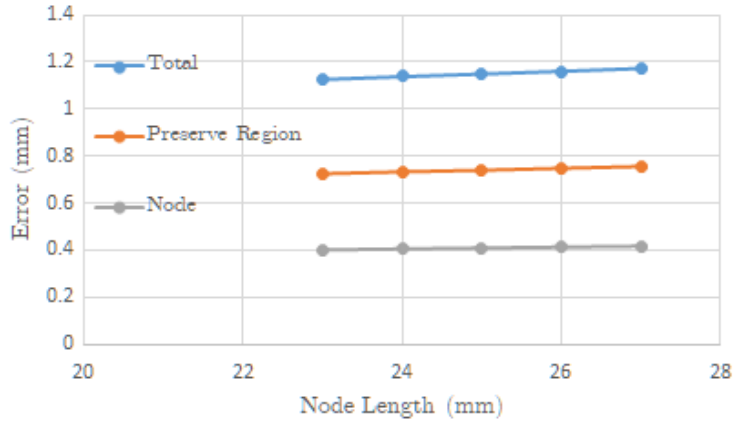

(b)

Figure 4.7: *Error sources as length varies: a) Relative error b) Absolute error*

4.2.1.2 Preserve Region Size and Shape

Figure 4.8 shows the graphs with the sizes of preserve regions when described as an arc in figure 4.8b. When varying the length, the size analysis of the preserve region showed very little variation. Changing the length from 23mm to 27mm did not cause the preserve region's size to change by even 0.25mm, hence why they all had a value of 9.5mm. Not only the size but the shape was also nearly identical for all values of length. In the graph in figure 4.8a, the preserve regions for each value of length can be seen. Much like the size, these are extremely similar, showing that the distribution of strain past the node also yields almost identical results irrespective of the length of the node.

As mentioned previously, the way the quality of the shape defining the boundary of the preserve region was measured, was through the variation in the strain along the boundary. When changing the length of the node, it consistently maintains the shape of an offset ellipse. This can be seen in the graph found in figure 4.8c. This graph shows the strain values along the elliptical boundary found during the analysis. It is worth noting that during the previous part of the analysis, the boundaries were found to be nearly identical. This means that the strain values along the ellipse are not only identical in value but also identical in location. This further reinforces the hypothesis that the length of the node has very little impact on the preserve region and its effects, as the way strain propagates is identical past the node. As far as variation goes, the shape appears to be very suited to an ellipse. There is a slight up-and-down fluctuation at the start and end of the elliptical line. This is, however, because the line technically enters the node region at the corners. Even with this region included, the variation is small. For all of these variations, the target strain for the boundary was $470\mu\epsilon$. Including the parts of the boundary that are slightly inconsistent, the highest deviation value was 12.6% below the target value. Ignoring the start and the end of the boundary line though, the strain appears extremely consistent, showing a maximum variance from the target value is 4.0% below the target value.

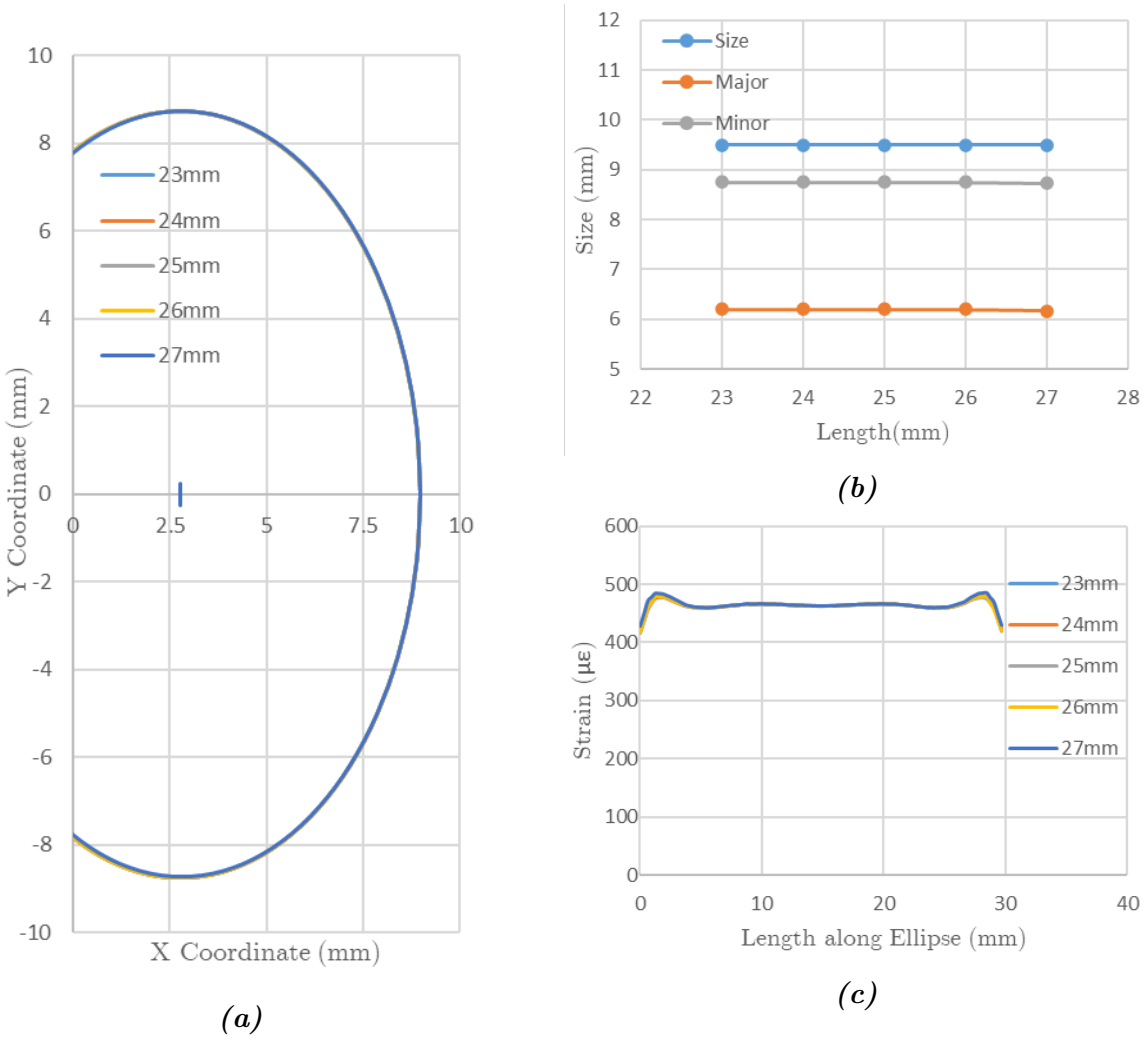

Figure 4.8: *Preserve region attributes as length varies:*
a) Shape of the region b) Size of the arc c) Strain values along the boundary

4.2.1.3 Effective Compliance

The results from finding the effective compliance of the nodes when varying the length can be seen in figure 4.9. It is evident that as the length increases the compliance in the y direction due to a force in the y direction becomes more accurate. When these values for effective compliance were used for a different loading scenario, it yielded far more accurate results when compared to the FEA, with the values for error never exceeding 0.2%. This implies that although the compliance is a vastly different number, sometimes being more than 45% different to that of the theoretical compliance, it still accurately accounts for all

the error found in the preserve region. The trend for the compliance in the y direction due to a moment in the z direction shows little change compared to that of the compliance in the y direction. This compliance error is hardly affected by the length of the node, having all values being around 6-8% error and no trend showing it is increasing or decreasing with the length.

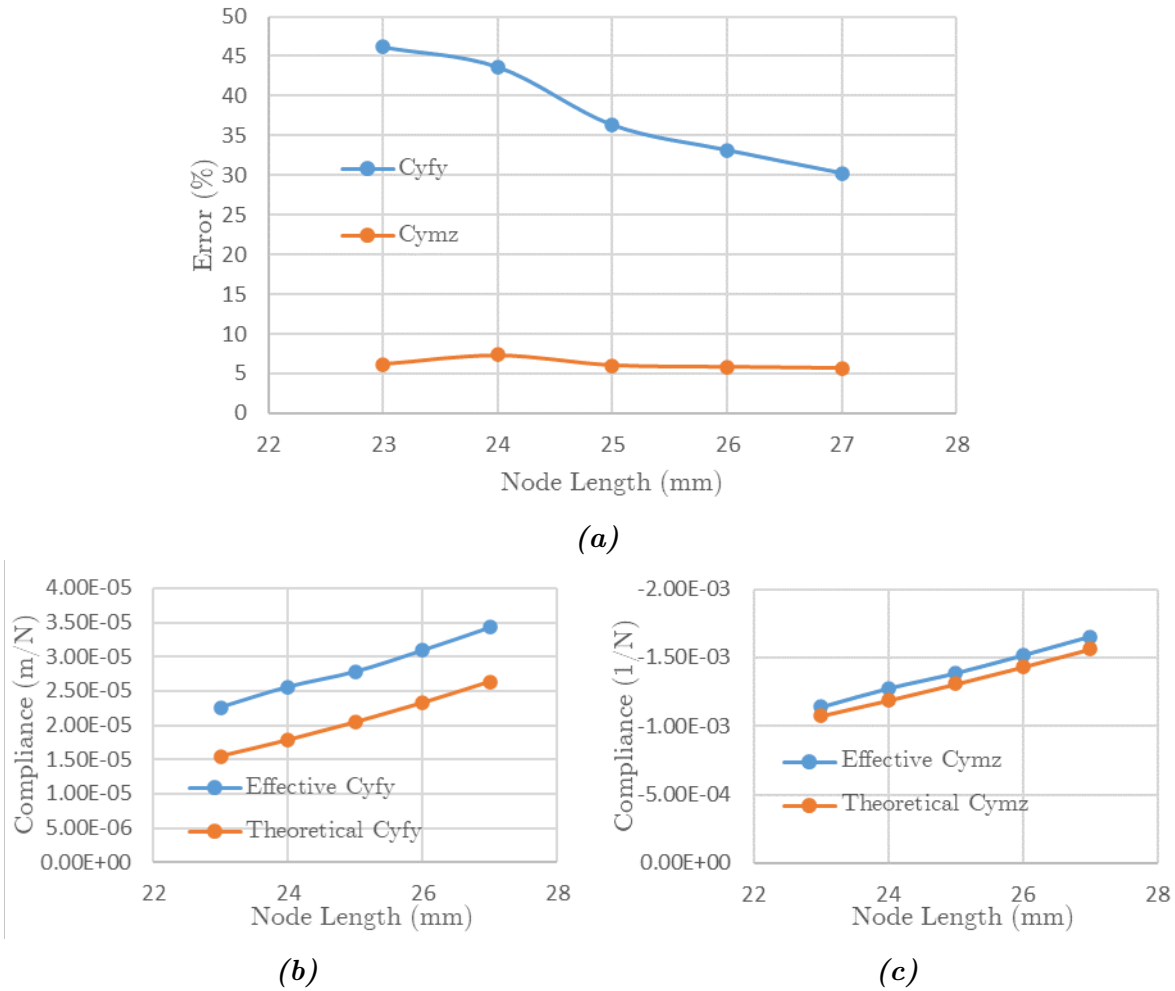

Figure 4.9: *Effective compliances as the length varies a) Relative Error b) C_{y-fy} c) C_{y-mz}*

4.2.2 Thickness Variation

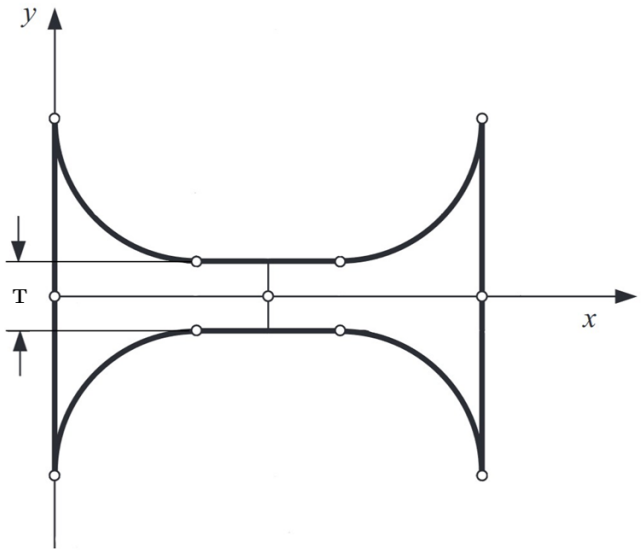

Figure 4.10: *Thickness labelled*

The next variable investigated was the thickness of the node. In the sensitivity analysis in section 4.1, a hypothesis was drawn that changing the thickness will have a substantial effect on the preserve region and its impact. Conclusions were made in this section as to whether or not this was true. For the testing, the length was kept at a constant 25.75mm, the radius of the fillet was always 6mm, and the width was kept at 10mm. The material was assumed to also be polypropylene with a stiffness of 1.725 GPA. The load was 10N acting vertically at an offset distance of 92.5mm. The thickness was varied from 4mm to 8mm in increments of 1mm.

4.2.2.1 Tip Displacements

Looking at the error sources present when varying the thickness in figure 4.11 shows some very clear trends. As a whole, increasing the thickness of the node can lead to extremely detrimental results when it comes to accuracy. The error increased from 6.84% to 18.9% for thickness 4mm to 8mm. Further investigation as to where this error comes from shows that a substantial amount of this increase is present in the preserve region. The preserve

region error increased from 4.13% to 14.74%, more than a 10% error gained, while the error within only the node saw an increase from 2.71% to 4.15%. This shows that a large portion of the inaccuracy of the theory for thicker nodes comes from the preserve region's impact increasing.

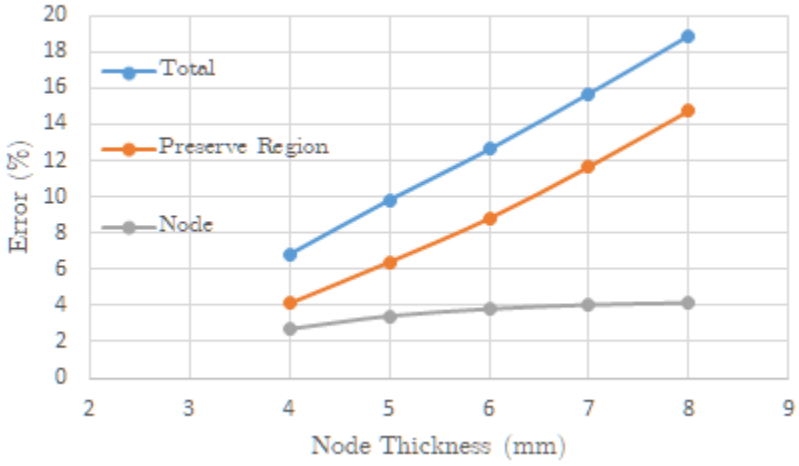

(a)

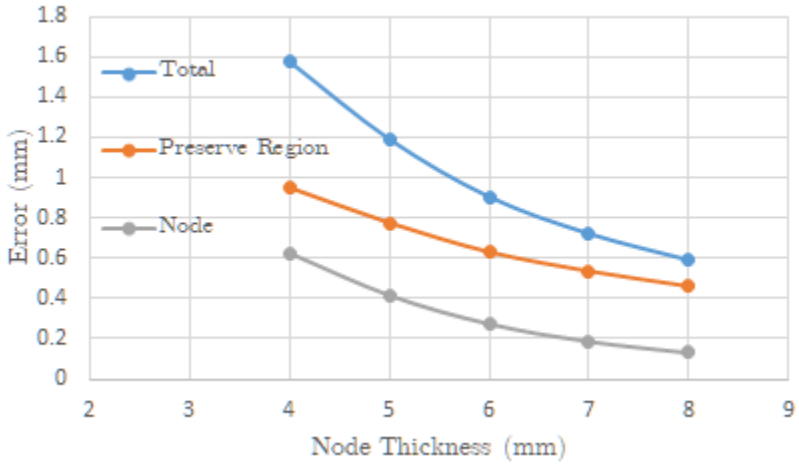

(b)

Figure 4.11: *Error sources as thickness varies: a) Relative error b) Absolute error*

4.2.2.2 Preserve Region Size and Shape

In figure 4.12 are the shapes and sizes of the preserve regions as the thickness is varied. It is clear that as the thickness increases, the preserve region size increases. The radius of the arc that describes the preserve region increases from 8.5mm to 13mm. This means that the amount of substantial strain outside of the node is distributed further past the node. The reason for this is that there is less strain both inside and outside the node. This means that the strain within the preserve region will overall be lower, meaning that it needs to be larger to encompass most of the absolute error outside the node.

The trend of the shape is also very consistent. The preserve region shapes can be seen in figure 4.12a. As the thickness increases, the size of the ellipse increases as well. The centre of each ellipse is marked on the graph in the same figure and is shown to gradually shift to the right with the increase in thickness. This means that the further away the preserve region boundary is, the largest and more offset the ellipse defining it will be.

In figure 4.12c the strain variation along the boundary line can be seen. The first noteworthy feature is the target amount of strain for each geometric variation. For the thicker nodes, the strain value that the boundary is trying to maintain reduces. This is due to, as mentioned before, the fact that the thicker nodes require less strain to have an impact on error. For that reason, the preserve region expands further past the node and the boundary is at a lower value of strain. Analysing the variation of strain along the boundary shows that an elliptical shape describes the preserve region very well. Similar to that of the length variation, the points on the boundary closest to the node show the most variation. As discussed in that section, this is likely since, at these points, the strain shows some irregular effects from being inside of the node. This led to the most variation being present in the 5mm node at 10.22%. This value is right at the start and the end of the boundary. Excluding this value from the analysis leads to a variation of 2.34% over most of the boundary. This variation only reduces as the thickness increases, going down to 5.217% at 8mm thickness including the irregular edges of the boundary.

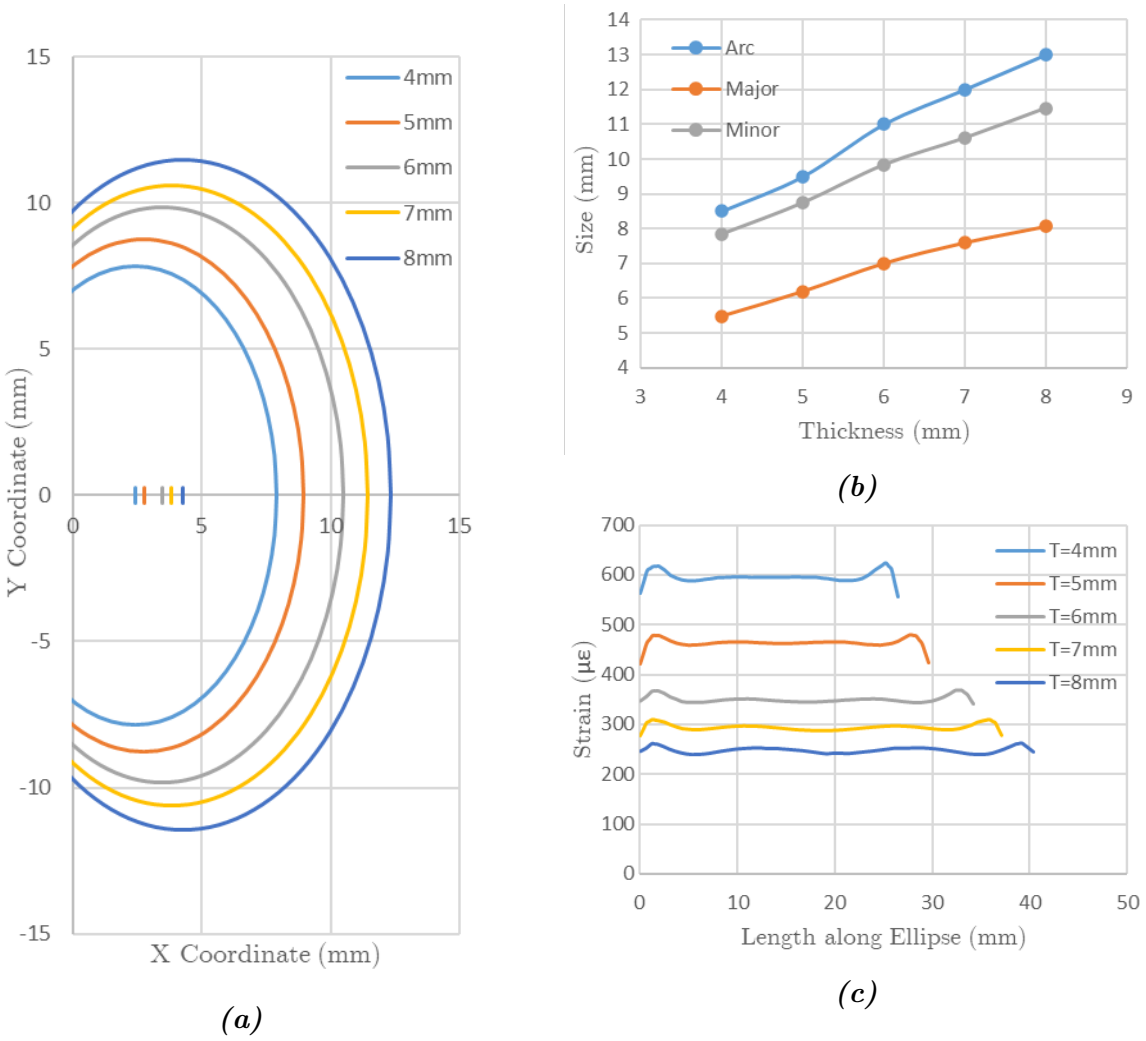

Figure 4.12: *Preserve region attributes as thickness varies: a) Shape of the region b) Size of the arc c) Strain values along the boundary*

Figure 4.13 shows the strains in a horizontal line past the node. On this graph, it is clear that all the values of strain trend toward the same number. However, due to the strain being overall less for a thicker sample, the value of strain that no longer impacts the total error of the preserve region is much lower and will, therefore, take longer to reach. The 4mm node takes 10.3mm before the strain value is 10% of what it was right at the node boundary, while the 8mm node is at 11.16% of the initial value at 15mm

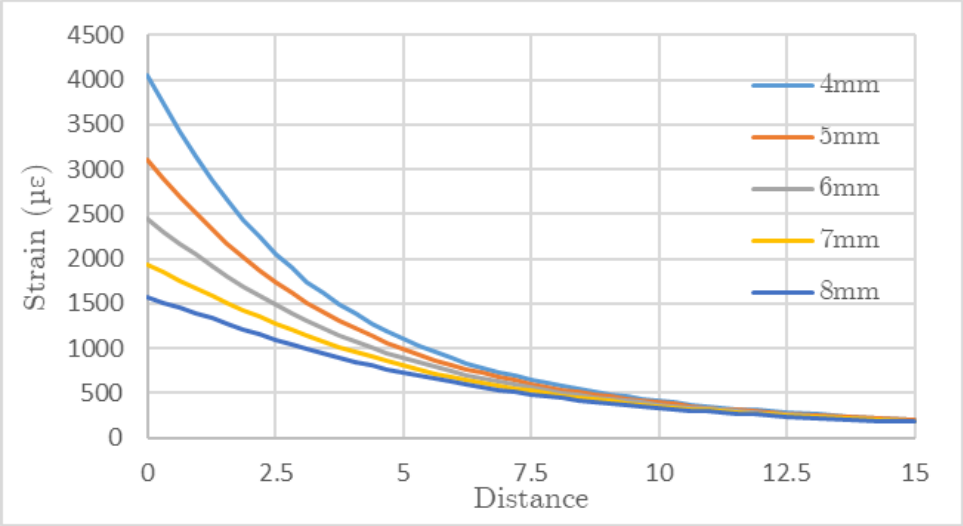

Figure 4.13: *Strain propagation horizontally as thickness varies*

4.2.2.3 Effective Compliance

Investigating the true compliance of the system leads to some interesting results. Firstly, the trend of the effective compliance and the theoretical compliance is very similar for both the compliance in the y direction due to a force in the y direction as well as a moment in the z direction. There is a substantial increase in error for the compliance in the y direction due to a force in the y direction. This increase is in large part due to the preserve region. As shown in the previous part of the analysis, the majority of the unexpected displacement at the tip is due to the preserve region, particularly for the thicker samples. Although the absolute error between the theory and FEA does not change drastically, as the compliance value gets smaller and smaller due to the thicker nodes, the impact it has ends up being very intense. This led to the compliance of the node initially being 20.53% larger at 4mm to being 102.18% larger at 8mm when measured on FEA. It should be noted that although the y compliance is double for the thickest nodes, that does not mean the displacement at the tip will be double what is expected, as when the compliance of only the node gets translated to where the load is placed, the other compliances plays a role in the accuracy as well. Much like with varying the length, the error of compliance in the Z direction remained largely the same. It has no distinguished trend and seems to hover around the 5% value.

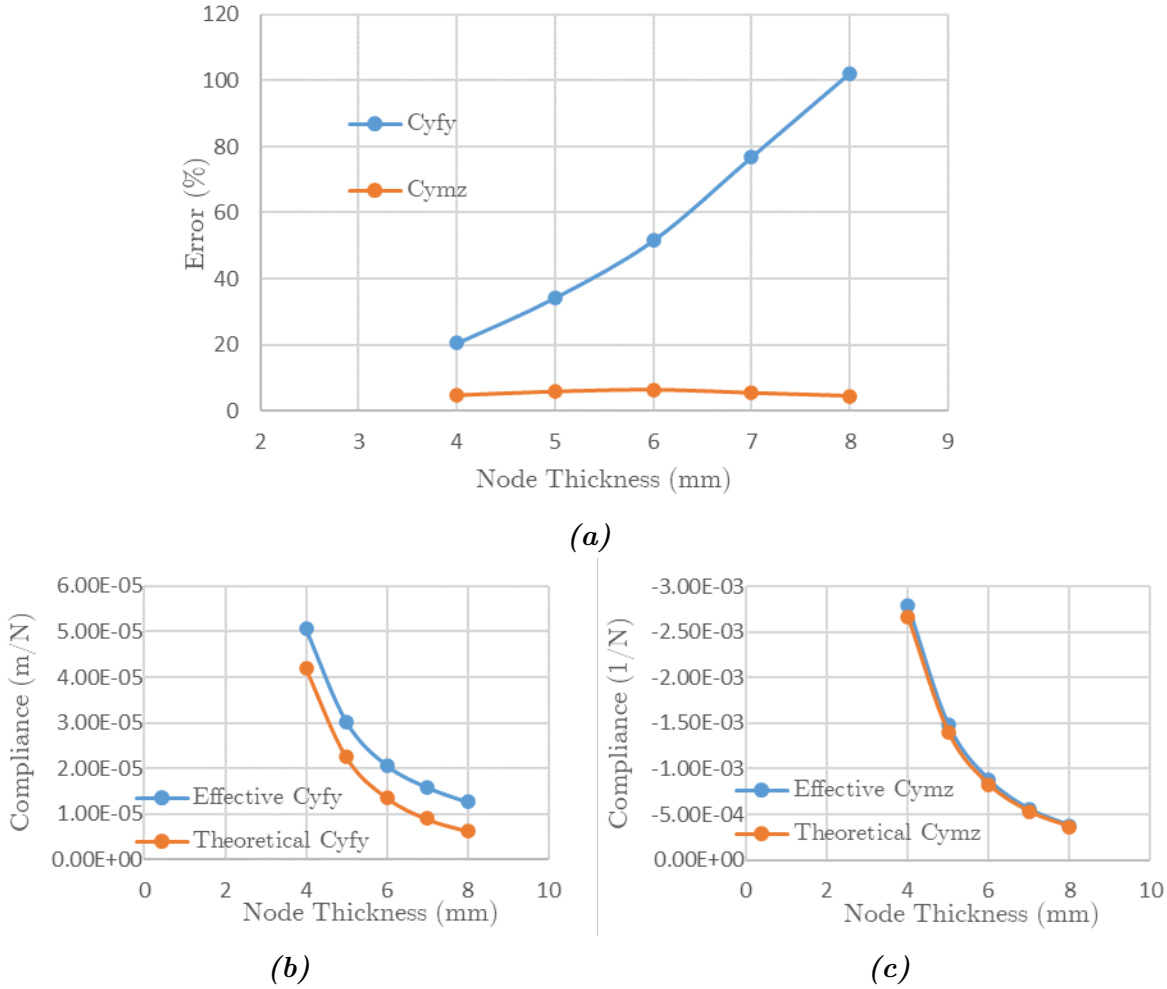

Figure 4.14: *Effective compliances as the thickness varies a) Relative Error b) C_{y-fy} c) C_{y-mz}*

4.2.3 Circular Fillet Variation

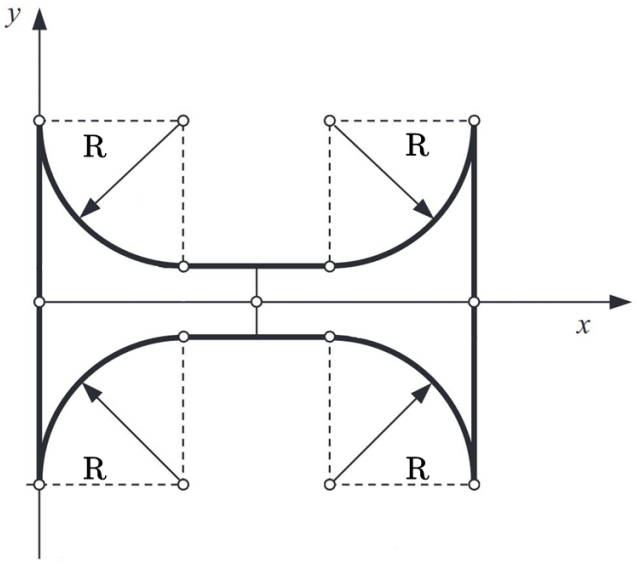

Figure 4.15: *Radius labelled*

This part of the analysis surrounded the impact that the filleting of the node has on the preserve region, specifically with using common circular fillets. During the sensitivity analysis section, it was hard to establish the exact effect that varying the radius would have on the accuracy of the results. It is suspected that this is because having extremely small fillets leads to stress concentration as an additional source of error. The nodes in this analysis were kept at a constant length, thickness and width of 25.75mm, 4mm, and 10mm respectively. The radius was varied from 4mm to 8mm with 1mm increments. The material was assumed to be polypropylene with a stiffness of 1.725 GPa, and the load was set to 10N at an offset of 92.5mm from the node.

4.2.3.1 Tip Displacements

In figure 4.16 are the graphs showing the sources of error found when varying the fillet radius of the node. As mentioned in the sensitivity analysis section, the overall error appears to change unexpectedly. It seems that as the radius increases, the error first

decreases and then progressively increases. An understanding was gained as to why this is the case. When breaking down the source of error, it can be seen that as the radius increases in size, the error that is gained from the preserve region decreases, going from 5.32% to 3.23% from a 4mm fillet to an 8mm fillet. This would make sense as there is less stress at the corners of the node and, therefore, less strain in the rigid section. However, increasing the radius of the fillet also increases the error present in the node, increasing from 1.52% to 3.73%. There is a point when varying the radius of the fillet where the sum of these two sources of error is minimised, however, the points before and after this show this sum increases.

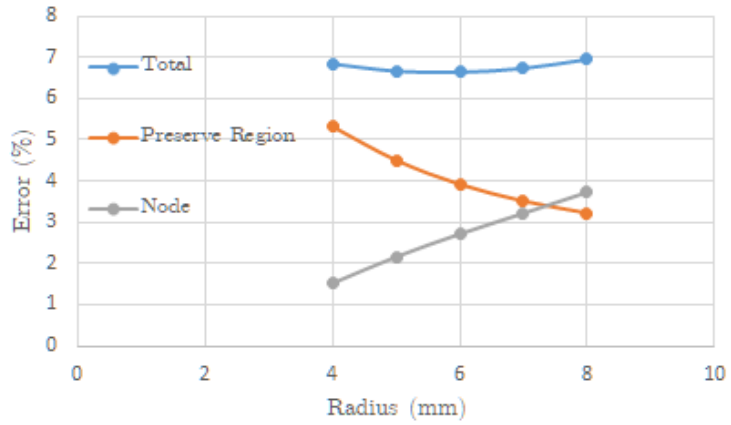

(a)

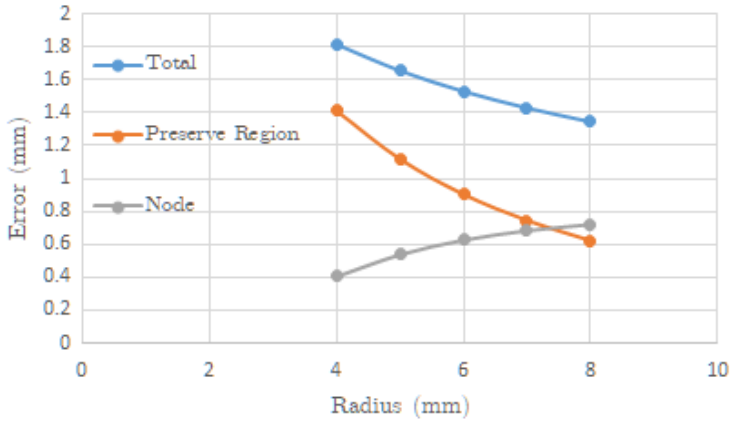

(b)

Figure 4.16: *Error sources as fillet radius varies a) Relative error b) Absolute error*

4.2.3.2 Preserve Region Size and Shape

In figure 4.17 are the graphs showing the size and shape of the preserve region. Interestingly, it was found that the error of the preserve region decreased as the fillets became larger, while the size of the preserve region increased. This is the opposite relationship as seen in the thickness analysis, where both the impact and the size of the preserve region increased as the thickness increased. The most likely explanation as to why this trend is observed is that the smaller fillets cause more strain to be localised just outside of the node. The larger fillets allow for a wider interface between the node and the rigid section, which in turn means that the strain can be distributed between a larger set of points.

Figure 4.17c is a graph showing how the strain varies along the elliptical boundary line of the preserve region. As mentioned previously, the smaller radii cause a larger concentration of strain at the end of the node. This concentration leads to most of the error being found shortly after the node, and therefore, the preserve region boundary is closer to the node as well. This closer boundary holds larger values for strain, as the strain has not yet been able to dissipate. As far as variance goes, the same issue is present as in the previous two analyses. The method used for defining the preserve region was shown to be effective apart from the corners of the boundary. These corners start lower than the target value of strain and then exceed it shortly after. After these points, the strain flattens to a value close to the target strain and remains very constant. The largest variance in strain is found in the 4mm and 5mm fillet radius nodes, where the largest deviation from the target value is 15.70% and 14.16% respectively. Outside of these results, the rest of the variations showed far better accuracy, with the worst being a 7mm fillet radius with a maximum variance of 6.17%. It should be noted that all of these values include the corners of the elliptical fillet, which, as mentioned before, could be considered outliers as they are affected by geometries only present at these corners. The values excluding these are far more consistent, with the worst variation after the corners being the 4mm fillet radius with a deviation from the target of 2.6%.

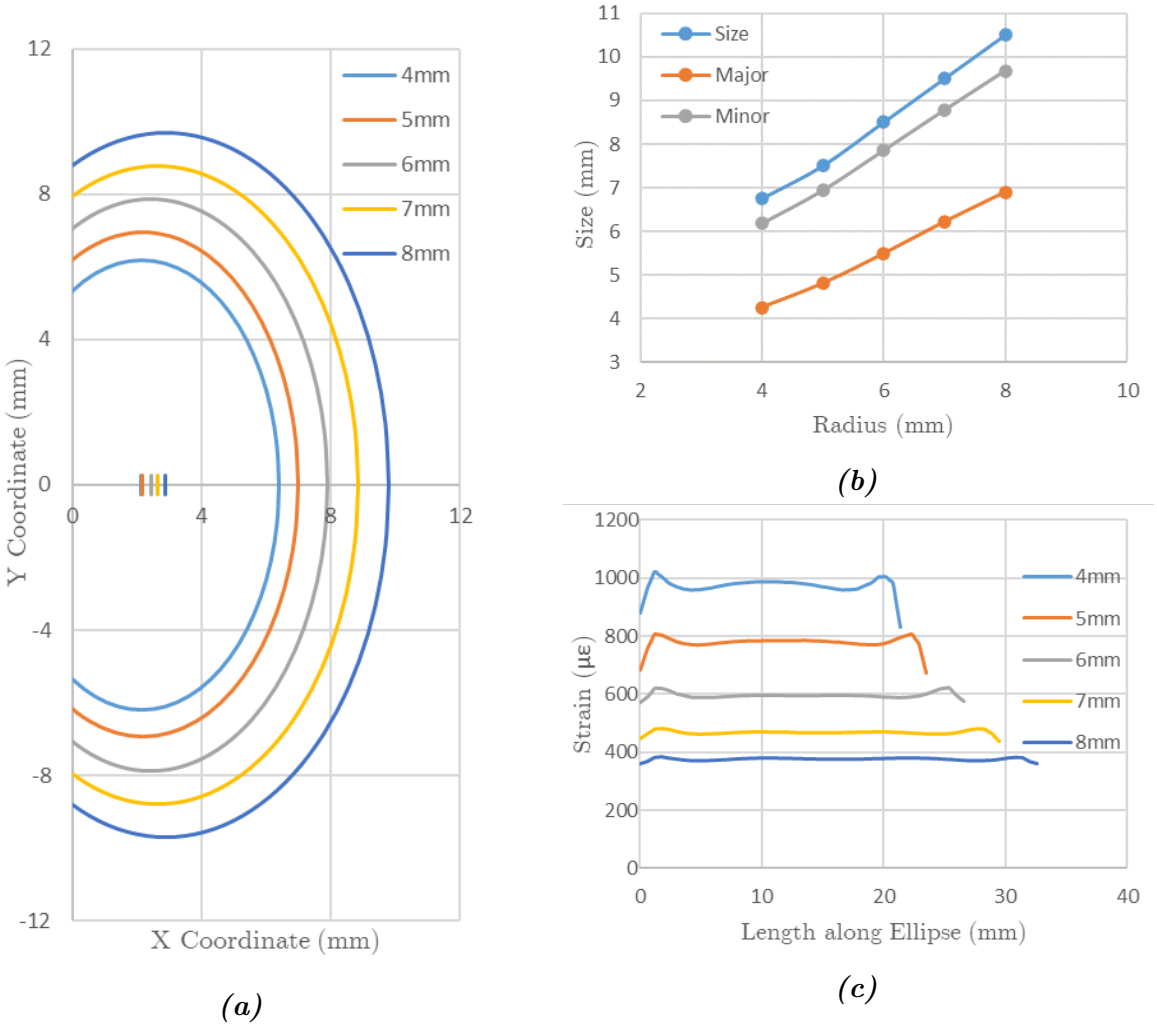

Figure 4.17: *Preserve region attributes as fillet radius varies*
a) Shape of the region b) Size of the arc c) Strain values along the boundary

To further reinforce the points made earlier in this section, the graph in figure 4.18 was made. This graph shows the strain values in a horizontal line past the node. As expected, the strain values just outside of the node are much lower for higher radii, the reason for the preserve region increasing in size as the radius is increased. At a fillet radius of 4mm, it takes 8.5mm for the strain to reach 10% of the value shown at the start of the preserve region, while an 8mm fillet takes 11.8mm to reach 10%.

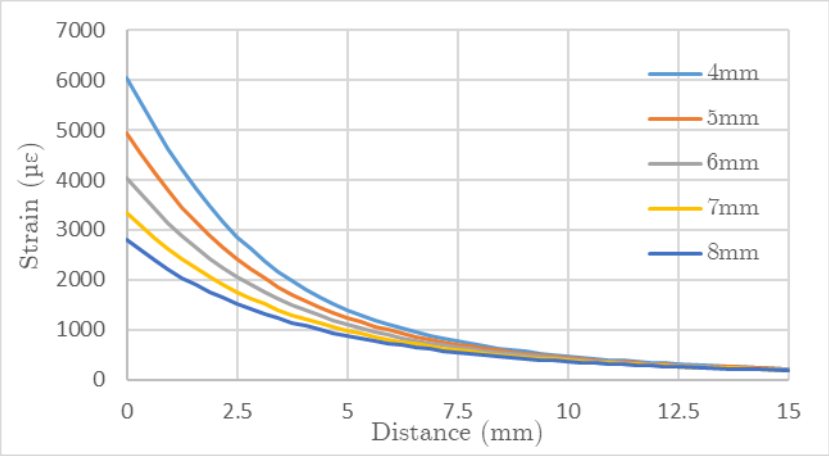

Figure 4.18: *Strain propagation horizontal outside of node as fillet radius varies*

4.2.3.3 Effective Compliance

The figures above show the change in compliance as the radius of the fillet is varied. When performing the part of the analysis that finds the effective compliance, it is worth noting that the results are very sensitive. If the values extracted from the Ansys are altered even slightly, it can have a drastic impact on the error present. For the last 2 analyses, this did not cause any issues in these sections as the variation in error is very large, and any inaccuracies in the simulation did not impact the overall conclusions. During the analysis of the radius of the fillet, it may have had an impact on one of the data points. There is only an outlier in the value of the 5mm radius fillet, where it seems as though the value is higher than the trend would have implied. Overall, the error is not nearly as impacted by the radius of the fillet when compared to the length and the thickness. The lowest value of error was at 6mm with 16.41%, and the largest error (ignoring the outlier) was 19.35% at 4mm.

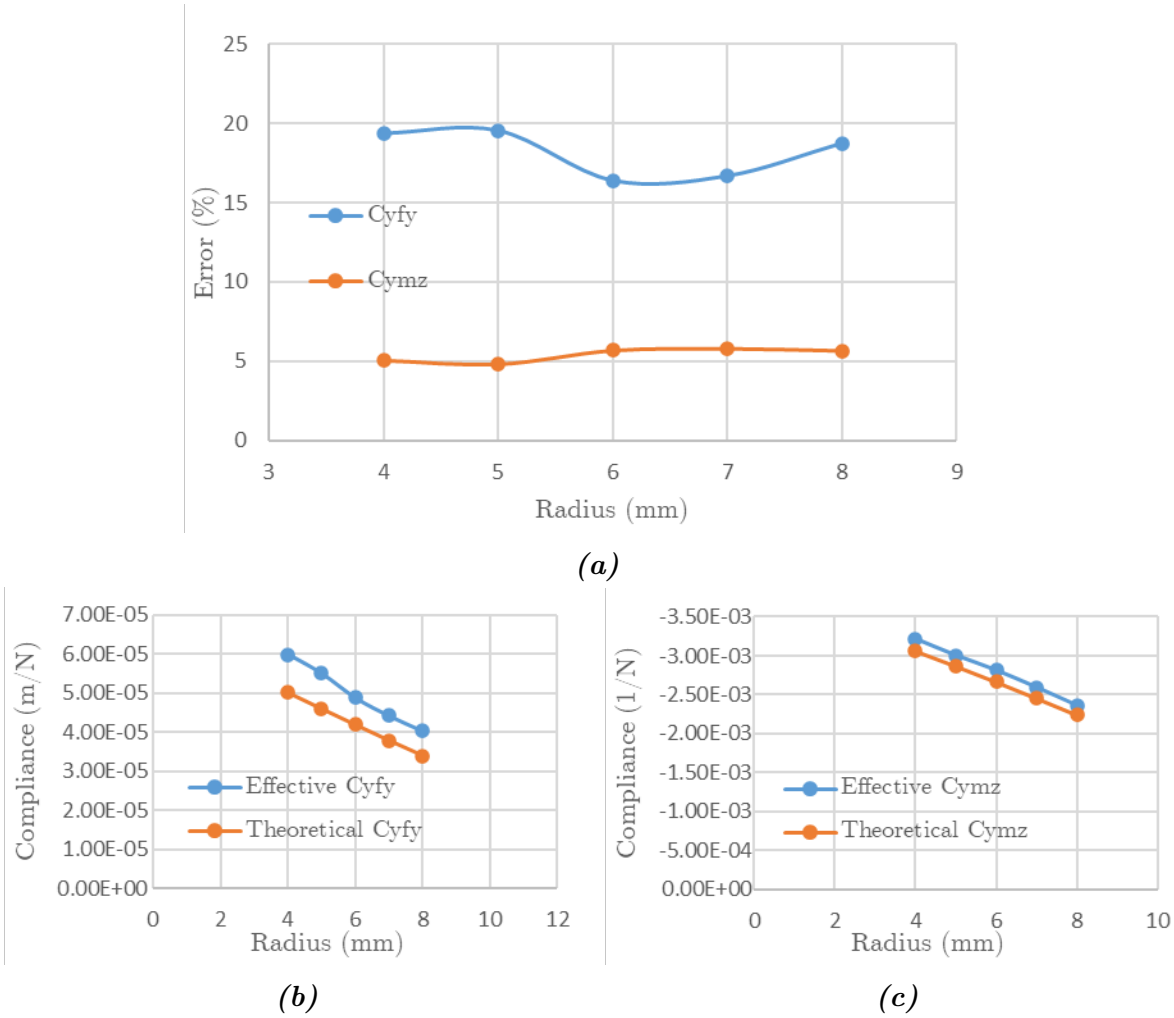

Figure 4.19: *Effective compliances as the fillet radius varies a) Relative Error b) C_{y-fy} c) C_{y-mz}*

4.2.4 Elliptical Fillet Variation (Major Axis)

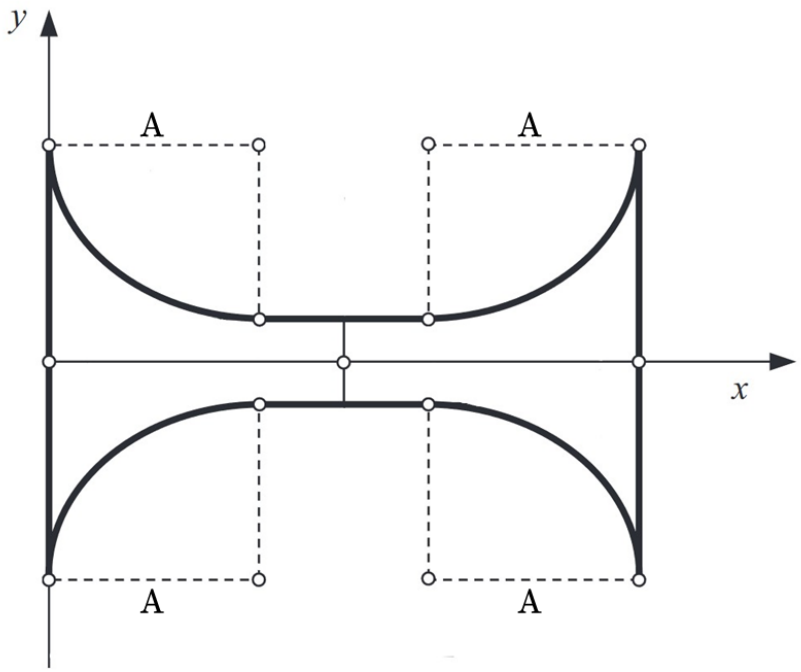

Figure 4.20: *Major axis labelled*

To help understand what part of the fillet caused the trends seen in the previous section, elliptical variations of the node fillet were analysed. When the fillet is made into an elliptical fillet as opposed to a circular fillet, it is no longer defined by only a radius, but instead a major and minor axis. For this section, the major axis will be investigated. From the sensitivity analysis, it was difficult to pinpoint the exact impact that changing the major axis had on the accuracy of the results. For this part of the analysis, the length was kept at a constant 25mm, the minor axis was kept at 6mm, the thickness was 5mm, and the width was 10mm. The stiffness is assumed to be 1.725 GPa, and the load was at an offset of 92.5mm. During the analysis, there is a point where the major axis becomes smaller than the minor axis. This technically means that the minor axis should now be defined as the major axis, however, for simplicity the label remains the same throughout.

4.2.4.1 Tip Displacements

Figure 4.21 shows the data gathered when investigating the major axis of the node fillets. From an accuracy point of view, the impact that the major axis has is not as substantial as other variables. As the major axis increases in size, the error overall shares the same trend as the radius. Initially, increasing the major axis reduces the error, however, after the major axis reaches 6mm, it begins to increase the error. The error is at its lowest when the major axis is closest to the minor axis, this is likely due to the irregular geometry causing the fillets to be sharper, and causing stress concentration at those points. As far as isolating the error, for smaller major axis values, the error is present more in the preserve region, while for larger values the error reduces in the preserve region and is more within the node itself. It is worth noting that the changes in this section are far smaller than in previous sections. The trend seen with increasing the major axis appears rather similar to the trend seen when increasing the fillet radius, where increasing both of these values leads to a smaller error in only the preserve region and a larger error in the node. When analysing the radius, however, the error in the preserve region dropped from 5.32% to 3.23%, compared to the reduction in preserve region error in the major axis from 7.38% to 6.23%, a far less substantial reduction.

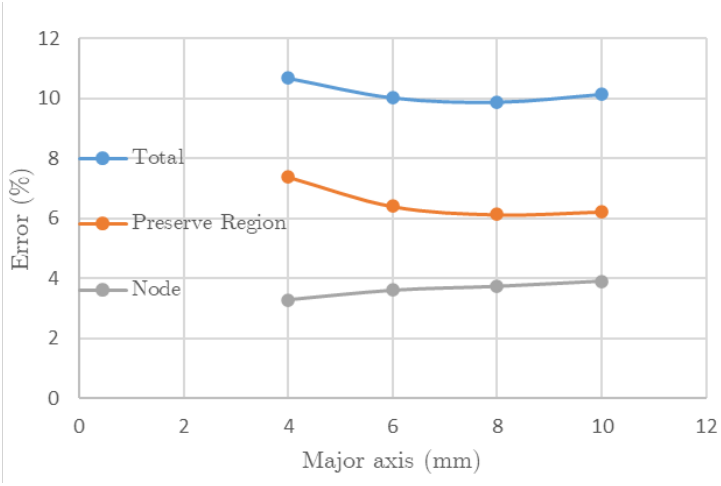

(a)

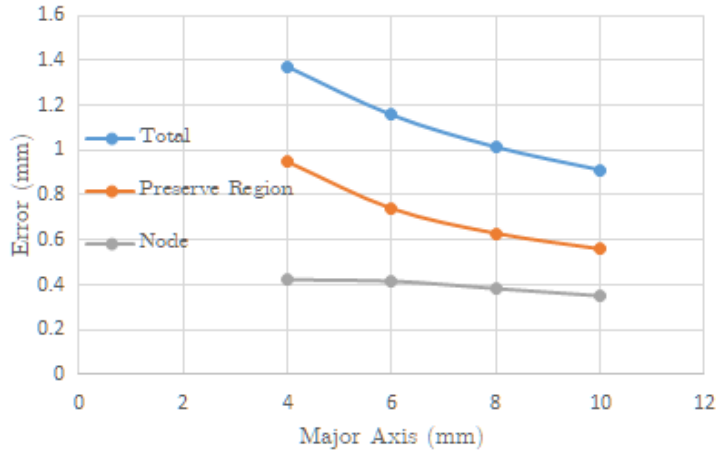

(b)

Figure 4.21: *Error sources as major axis varies: a) Relative error b) Absolute error*

4.2.4.2 Preserve Region Size and Shape

Looking at figure 4.22, the size and shape of the preserve region can be seen. As the major axis of the fillet increases, the size of the preserve region increases. When the major axis was increased from 4mm to 10mm, the preserve region size increased from a radius of 7.5mm to 10mm. The reason for this increase is likely very similar to why the preserve region size increased with the increase in thickness. As the size of the major axis increases, the overall thickness of the node will also increase. This leads to a smaller amount of strain inside and outside of the node, meaning the strain further away from the node will

have a larger impact.

Looking at the strain distribution in figure 4.22c the strain variations along the elliptical boundary can be seen. Again, it appears as though an elliptical shape is a good shape to define the boundary of the preserve region. Much like the previous sections, the beginning and end of the boundary line often have the largest amount of variance in strain. The most variance was found in the largest major axis, where the strain was found to be 16.7% lower at the corner. Eliminating the corners, however, leads to a far lower amount of variance 5.8%.

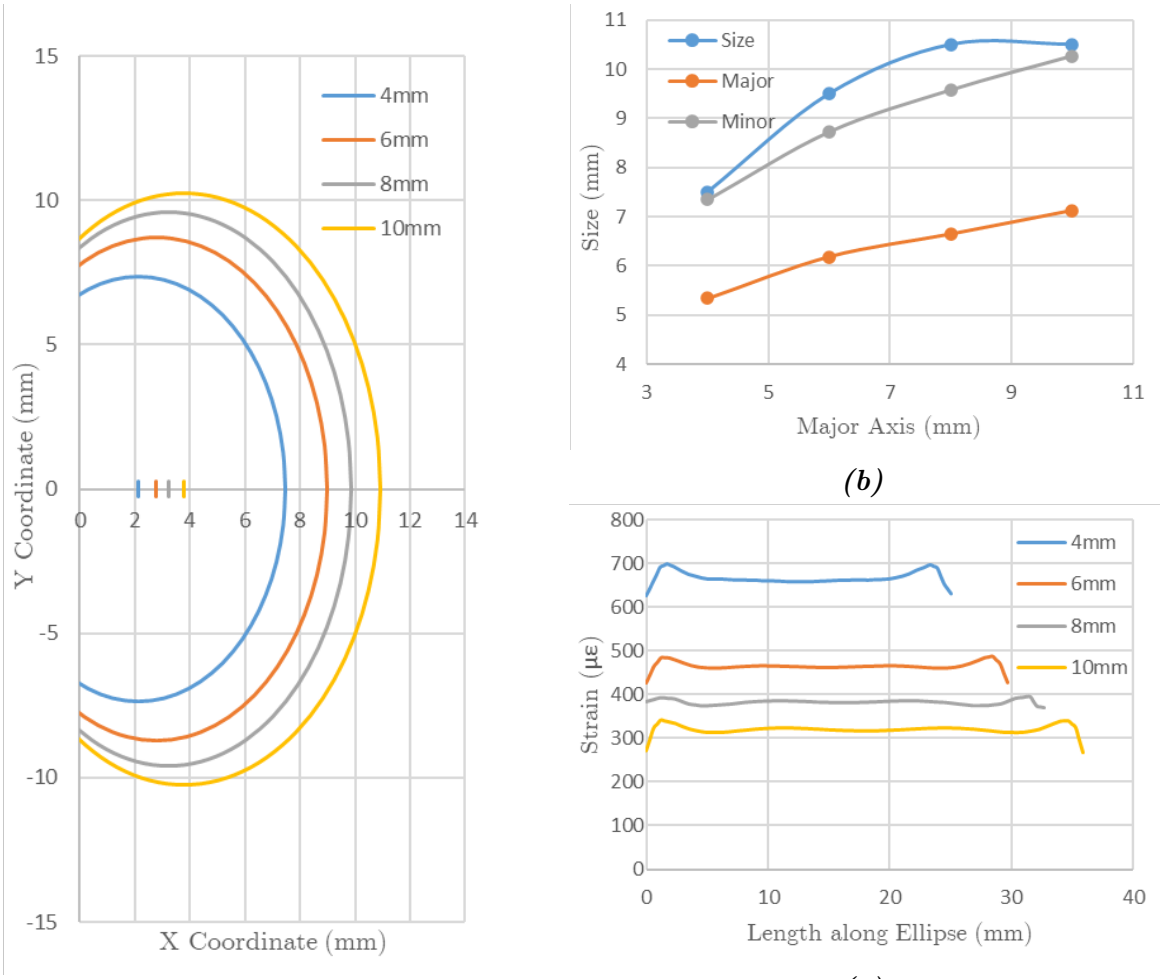

(a) *(b)* *(c)*

Figure 4.22: *Preserve region attributes as major axis varies: a) Shape of the region b) Size of the arc c) Strain along the boundary*

Figure 4.23 is the graph showing the strain in a straight line past the node. Looking at figure 4.23, it is clear that as the major axis becomes larger, the strain outside of the node decreases. This means that the reason the preserve region is larger for larger major axes is due the lower amount of strain outside of the node, making the region required to cover more area outside the node to achieve a significant amount of error. The strain at the boundary of the node saw a drop of 51.83% when the major axis increased from 4mm to 10mm. For the 4mm major axis, it took 9.8mm for the strain to drop by 90%, while the 10mm major axis took 14mm to drop strain by 90%, to further reinforce the wider distribution of strain.

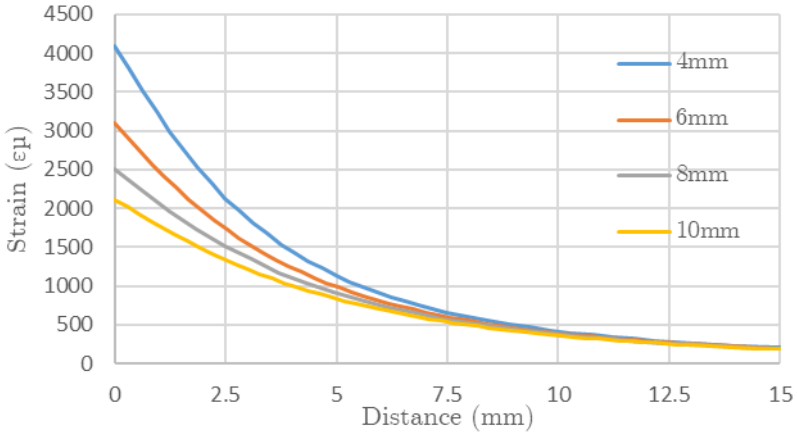

Figure 4.23: *Strain propagation horizontally as major axis varies*

4.2.4.3 Effective Compliance

In figure 4.24 the effective compliance for the different major axes can be seen. Much like the error in displacement, changing the major axis had only a minor effect on the error present in the compliances of the node. However, it can still be observed that as the major axis is increased the error in the y compliance due to a force about y and a moment about z both increase and decrease respectively, with the y compliance error increasing from 26.15% to 30.76% and the z compliance error decreasing from 6.50% to 4.66%. The smallest value tested at 4mm is the only value that appears to not fit the trend as strongly as the rest of the values. Increasing the major axis from 4mm to 6mm decreased the accuracy of the y compliance by 0.51% while increasing the major axis

from 6mm to 8mm increased the error by 2.18%. This is due to the fact that very small values of a major axis lead to the fillet becoming more of a sharp corner, causing stress concentration which in turn creates more unaccounted-for strain in the theory. Therefore, fillets with smaller major axes should be avoided.

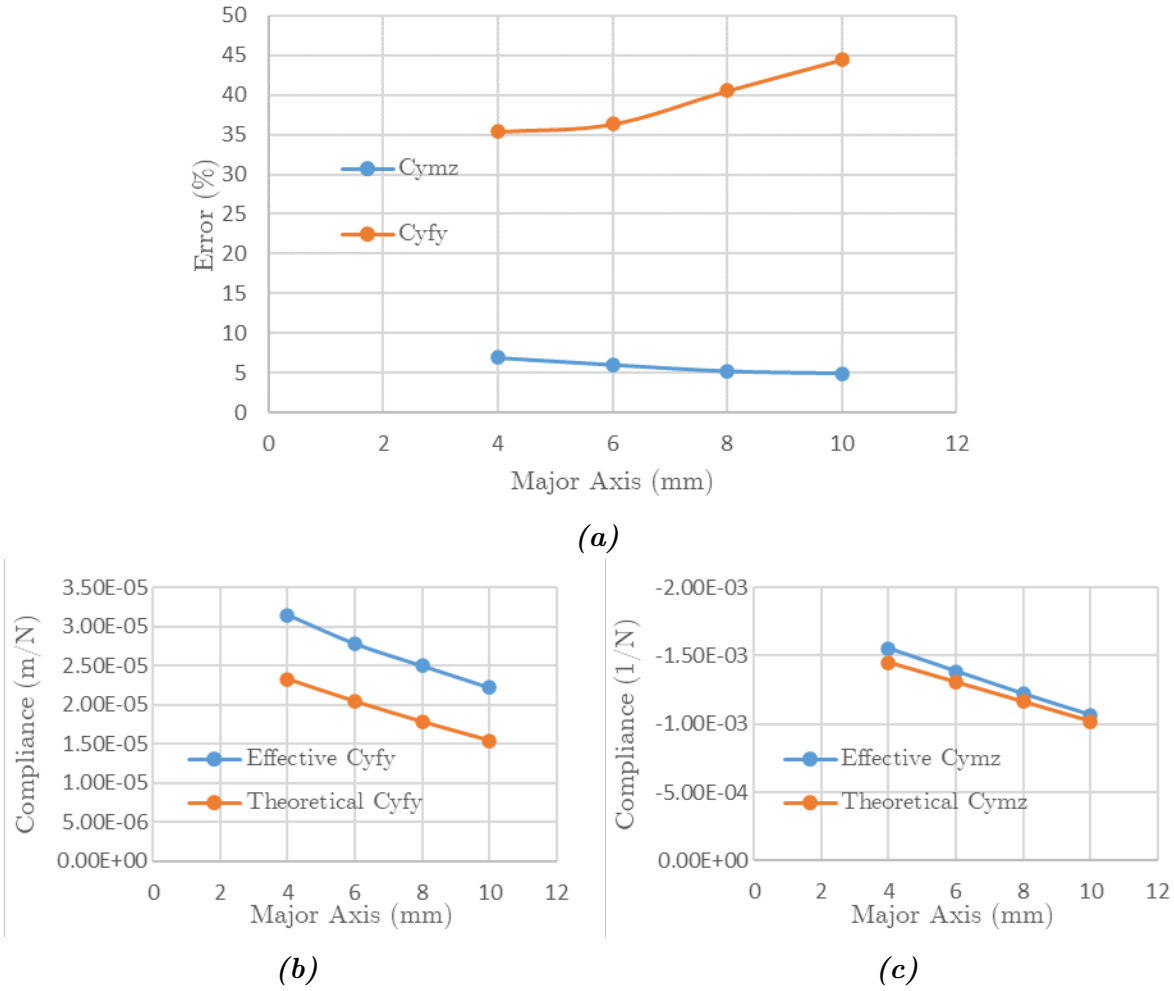

Figure 4.24: *Effective compliances as the major axis varies a) Relative Error b) C_{y-fy} c) C_{y-mz}*

4.2.5 Elliptical Fillet Variation (Minor Axis)

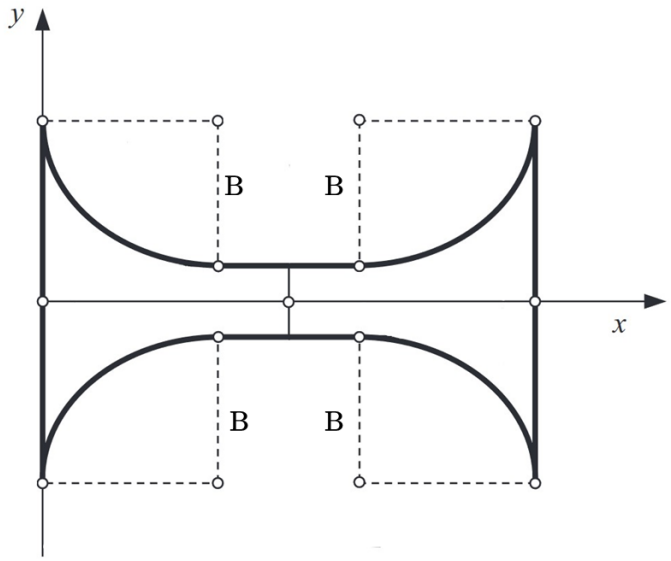

Figure 4.25: *Minor axis labelled*

This section covers the second part of investigating elliptical fillets. Instead of increasing the major axis (i.e. horizontal component), the minor axis or vertical component of the ellipse will analysed. Increasing the minor axis in the sensitivity analysis had both a positive and negative impact on the accuracy of the results depending on the size of the major axis and the current size of the minor axis. For this analysis, all geometric constants were kept the same from the previous elliptical analysis, except for the major axis and the minor axis. Now, the major axis will be kept at a constant 6mm while the minor axis will be varied. The material is also assumed to be polypropylene with a stiffness of 1.725GPa, and the load is 10N at an offset of 92.5mm.

4.2.5.1 Tip Displacements

In figure 4.26, the sources of error present when varying the minor axis can be seen. Unlike when varying the major axis, it is rather clear that increasing the minor axis harms the accuracy of the theory. Increasing the minor axis from 4mm to 10mm saw an increase of error overall from 9.57% to 11.16%. This increase is much more substantial than that of

the major axis. Error from specifically the node and the preserve region also showed an interesting relationship. For the same increase of 4mm to 10mm, the error present due to the preserve region decreased from 7.49% to 5.36%, while the error present only within the node increased from 2.08% to 5.8%. It is worth noting, however, that altering the minor axis in the way that was performed in this analysis leads to some very odd node shapes. This irregular shape could be contributing towards some of the errors present. The trend of more error being present within the node at higher values seems very similar to that found in varying the radius of the fillet in the previous analysis. This is likely because for smaller minor axes a stress concentrator may form similar to that of smaller radial fillets. However, there may also be a relationship between the error in the preserve region and the size of the interface between the node and the preserve region.

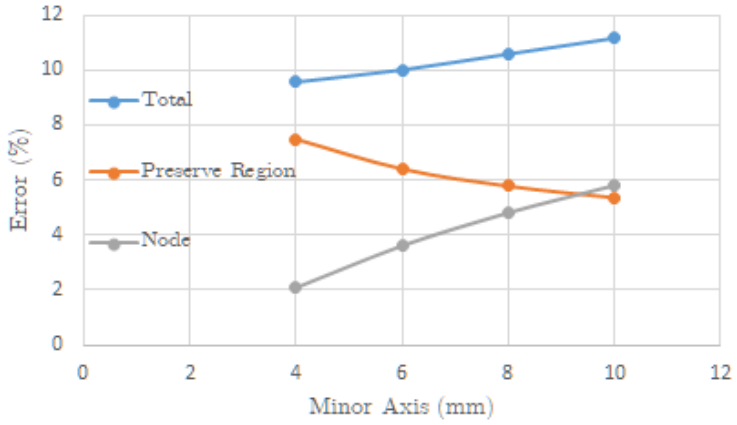

(a)

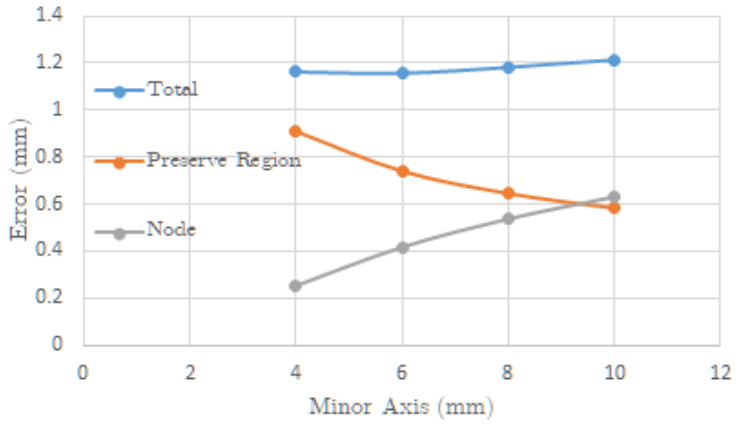

(b)

Figure 4.26: *Error sources as minor axis varies: a) Relative error b) Absolute error*

4.2.5.2 Preserve Region Size and Shape

Analysing the size and shape of the minor axis variation presented challenges that were not present in the rest of the data. Until this point in the investigation, all of the sizes of the preserve regions can be defined by an arc propagating past the node with a diameter that is always larger than the node boundary. However, due to the minor axis increasing the size of this node boundary so significantly, the diameter of the arc that encompasses most of the error in the preserve region does not exceed the size of the node boundary. This leads to the flexible region during the size analysis to include sharp corners where the arc meets the node, which could lead to unexpected and unpredictable results. It seems as though the minor axis has a lesser impact on the preserve region's shape and size. Increasing the size of the minor axis only saw an increase in the size of the preserve region from 8.5 to 10.25mm, with the increase from 8mm to 10mm only yielding an increase in the preserve region size of 0.25mm. This minor impact can also be seen in the shape. For the 2 largest values tested, the preserve region is nearly identical in shape, while the 6mm minor axis also has a very similar shape, only slightly lower at the starting point. From this data, it appears as though any value for the minor axis above the major axis yields less impact on the result.

In figure 4.27c the strain along the boundary of the preserve region can be seen. As with all the previous strain distributions, this one shows that the strain propagating past the node takes an elliptical shape. From this investigation, it can be said that larger values of the minor axis lead to a more elliptical distribution of strain past the node. Knowing this, and knowing that during the radial fillet investigation, the larger values for the radius also lead to less variation along an elliptical boundary, it can be concluded that the larger interface between the preserve region and the node region leads to strain distribution that is easier to resemble with an ellipse or circle. This is further reinforced by the fact that increasing any of the other geometric variables did not lead to nearly as much of an improvement in strain variation along the boundary, making their strain distribution slightly less elliptical. When B is set to 4mm, the maximum variation from the target is 17.82%, which got progressively better till it reached a maximum variation

of 3.30% when B was set to 10mm. All of these variations include the up and down flunctuations at the start and end shown by all of the other geometries, granting further confidence that the size of the minor axis made the shape more elliptical.

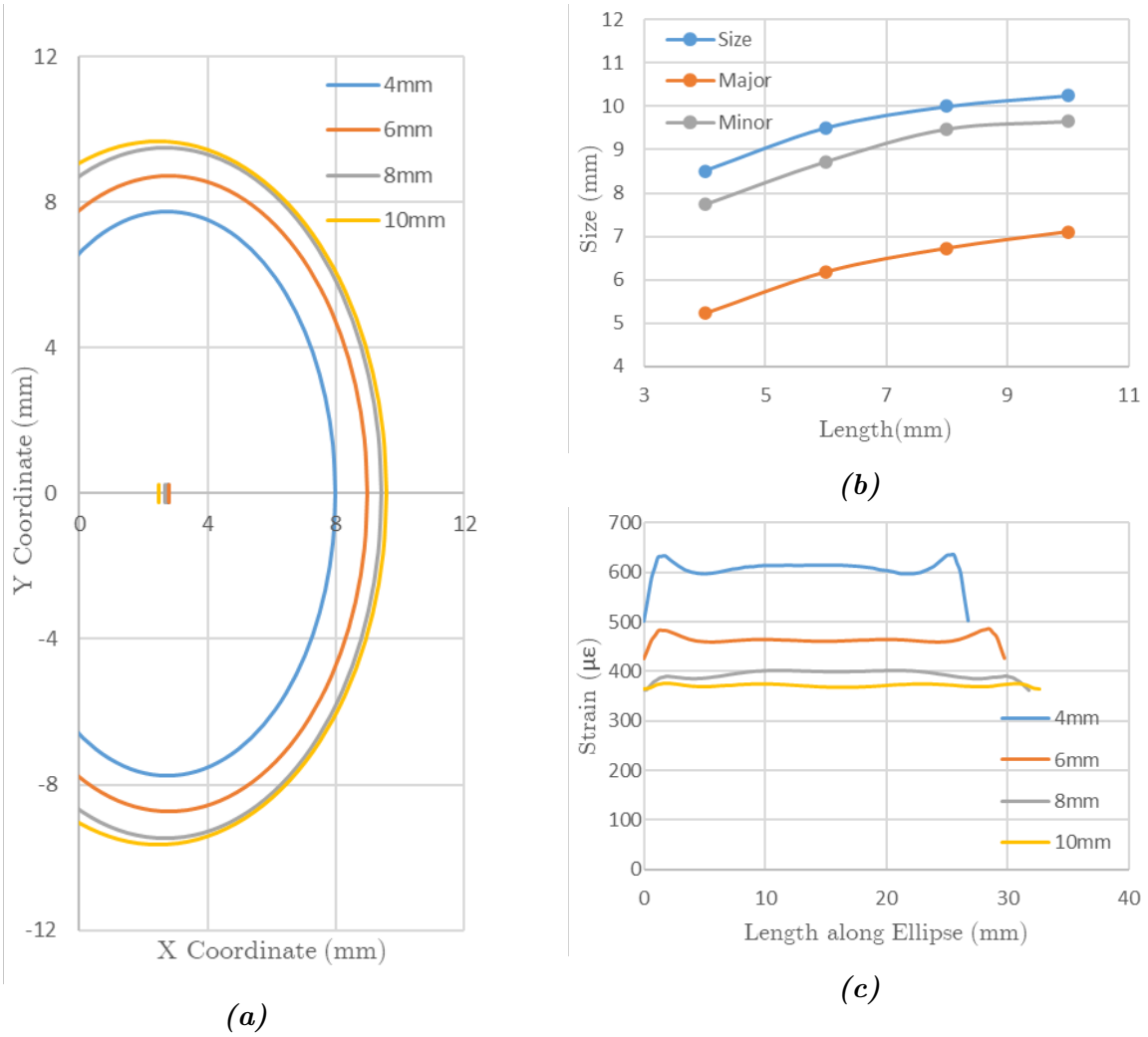

Figure 4.27: *Preserve region attributes as minor axis varies: a) Shape of the region b) Size of the arc c) Strain along the boundary*

In figure 4.28, the strain values past the node horizontally can be seen. The change in the strain outside the node reduces as the minor axis becomes larger. This reduction is not as large, however, especially when comparing it to the major axis variation. The difference in strain right at the node boundary sees a reduction of 22.02% from 4mm to 10mm, while for the major axis, there is a reduction of 48.33% from 4mm to 10mm. At a minor axis of 4mm, the strain takes 11.15mm to reach 10% of its original value, while for

a 10mm minor axis, it takes 11.60mm to reach 10% of its original value. This shows that the minor axis did impact strain propagation past the node, but not as much as other variables

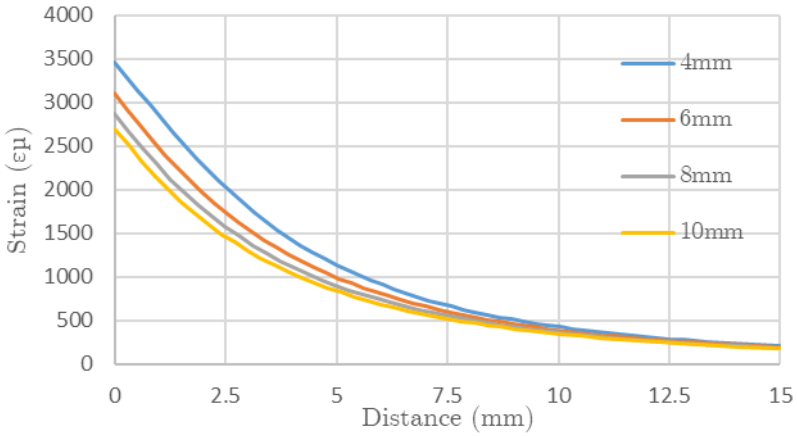

Figure 4.28: *Strain propagation horizontally as minor axis varies*

4.2.5.3 Effective Compliance

In figure 4.29 the values for effective compliance can be seen. Much like the error in tip displacement, the increase of the minor axis leads to an increase in error between the theory and the FEA. This increase is not as drastic as other variables, with only an increase from 35.09% to 40.63% when increasing the minor axis from 4mm to 10mm. This trend is the same for both the minor axis and the major axis of the fillet, where the smaller both variables are, the smaller the error becomes.

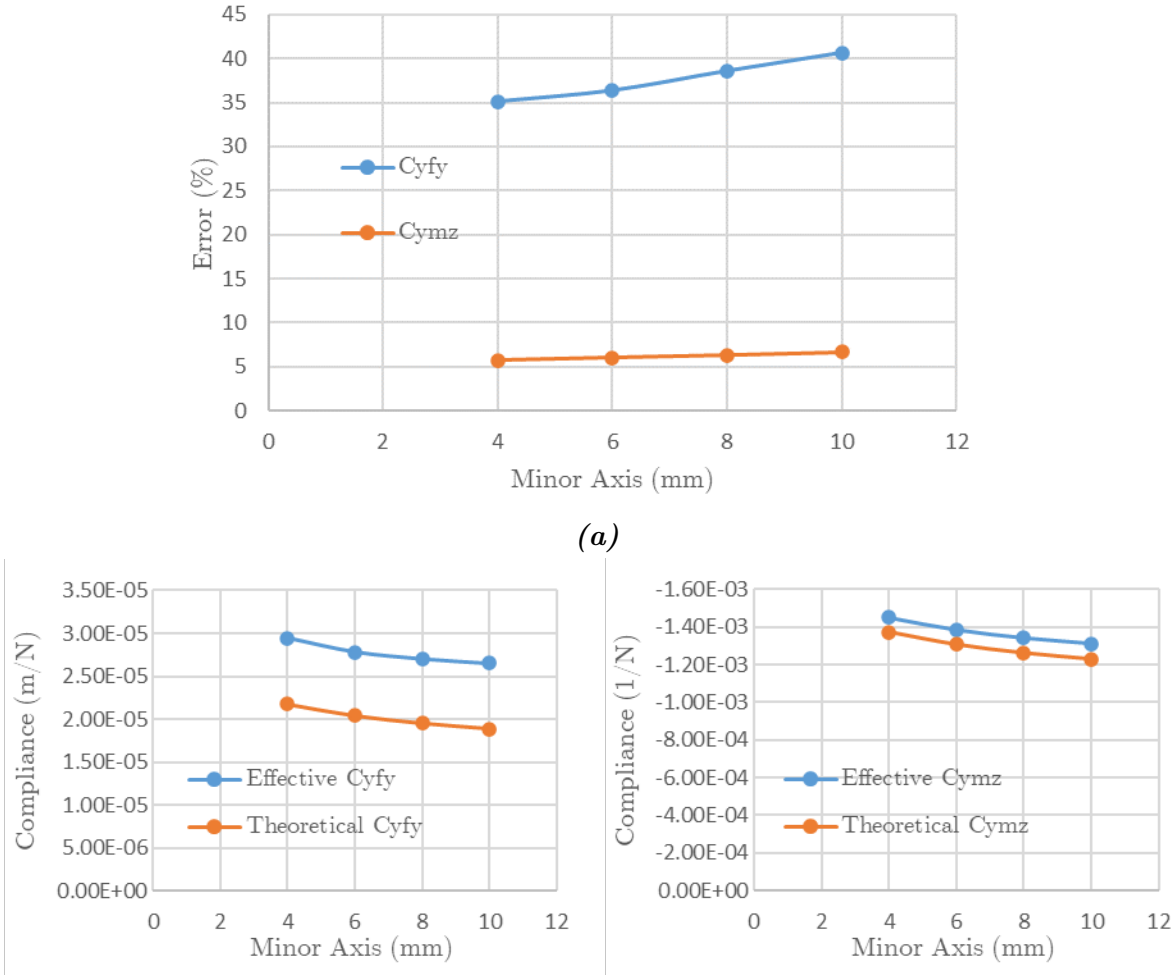

Figure 4.29: *Effective compliances as the minor axis varies a) Relative Error b) C_{y-fy} c) C_{y-mz}*

4.2.6 Preserve Region Analysis Summary

During this investigation, a vast range of geometries were analysed to find the effect they have on the preserve region, specifically its impact, size and shape. Overall, it is very clear that certain geometries are much more important to consider when trying to understand the impact of the preserve region, namely the thickness and the fillets. The length was found analytically to have virtually no impact on the absolute error present in the preserve region despite it having a substantial impact on the relative error overall. Altering the fillet radius showed a very interesting relationship to error, where the sources of error

change substantially. At smaller radii, there is more error found within the preserve region and less inside the node, while at larger radii, there is more error within the node and less error in the preserve region.

4.3 FEA Validation

As a large portion of the results were found on FEA, DIC was used on physical samples to validate the preserve region analysis performed in section 4.2. First was an investigation into how well the DIC system can measure the displacements at the tip of the samples. This is critical, as much of the FEA was used to verify tip displacements to that of the theory. After the displacements had been analysed, an investigation into the strain propagation was also done. Both a general observational approach as well as a quantitative approach was used.

4.3.1 Displacement Validation

Figure 4.30 shows an image of the analysis done with DIC, as well as the same analysis done using FEA. In both the FEA and the DIC scenarios, there is a void where the displacement should be measured. This means there is no point in measuring the tip displacement directly on the load. For this reason, a point just above where the load was placed was used. This is because, for DIC, no material can be speckled in this area so no data can be extracted. In FEA's case, there is no mesh in that area so there are no points to measure the displacement. For the purposes of FEA, the stiffness value was found to be 1968.57 MPa and the Poisson's ratio was assumed to be 0.45. The stiffness was found using dogbone samples made from the same sheet of polypropylene and the Poisson's ratio was found from another source [58].

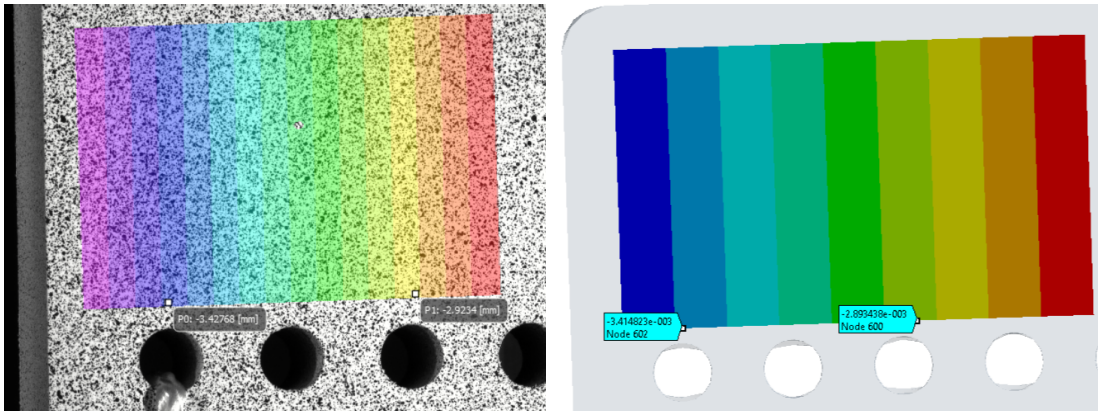

(a) *(b)*

Figure 4.30: *Displacement measurement a) DIC b) FEA*

Figure 4.31 shows the measured displacements from DIC and FEA. Already a source of error can be identified. During the test, as time passed, the displacement at the tip continuously increased. This is due to creep. Creep is time-dependent deformation under constant stress [60]. Creep is normally only present at high-stress scenarios or elevated temperatures. However, the threshold for polypropylene to experience creep is extremely low [61]. The creep was most present during the elliptical hinge test. The instantaneous displacement occurred at 1.4 seconds and was 3.42mm. After a further 8.6 seconds, the displacement increased by 11.4% to 3.81mm. This means that the only displacement that will be used to compare the DIC and the FEA is the instantaneous displacement, where the displacement abruptly stops before it begins to grow due to creep. It must be said that technically this instantaneous strain might experience a very small increase in displacement due to creep that occurred during the loading, however, this is assumed to be negligible.

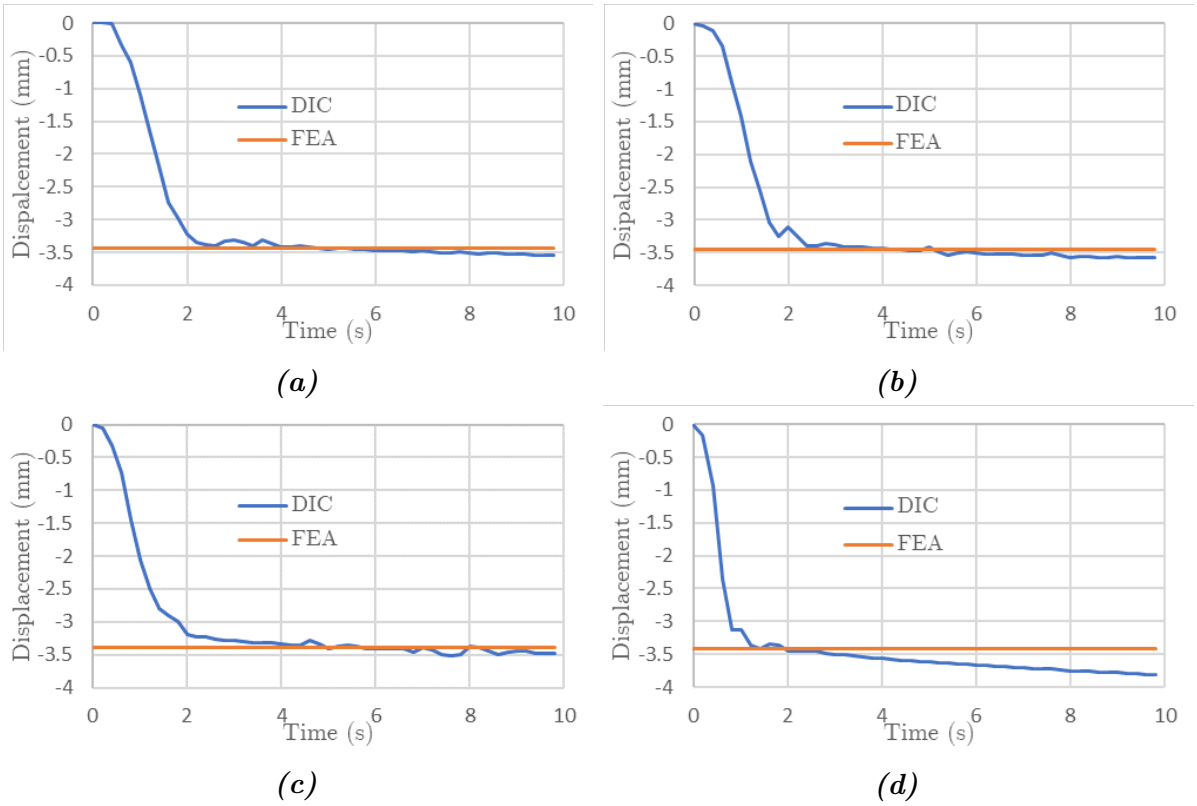

Figure 4.31: *Comparison of measured DIC and FEA tip displacement values. a) Circular filleted b) Circular hinge c) Elliptically filleted d) Elliptical hinge*

Looking at all of the instantaneous displacements, the circular filleted, elliptically filleted and the elliptical hinge all show similarity to that of the FEA. The circular hinge, however, appears to show a slightly lower displacement in the experimental test as opposed to the FEA. In table 4.1 all of the instantaneous displacements and their FEA counterparts can be seen.

Table 4.1: Table of displacement values

Node	Instantaneous Displacement (mm)	FEA Displacement (mm)	Error (FEA)	Error (Theory)
Circular filleted	3.405	3.440	1.01%	8.44%
Elliptically filleted	3.401	3.443	1.22%	8.38%
Circular hinge	3.200	3.386	5.49%	1.91%
Elliptical hinge	3.359	3.419	1.75%	6.97%

Both the circular filleted and elliptically filleted nodes are very similar on both FEA and DIC. This is expected as these two nodes are the most similar in dimensions. The

circular hinge showed the lowest displacement of the four node types. In theory, all of these node types would show a displacement of 3.14mm. However, as shown on the FEA, the displacements are substantially larger. The largest is the circular filleted node with an error of 8.44% and the lowest is the circular hinge with an error of 1.91%. When only investigating the FEA, it shows that if a node has a certain required compliance, achieving that compliance with different geometries may impact the accuracy. If a node was designed theoretically with an elliptically filleted node shape, an error of 9.55% will be seen. If, instead, a circular hinge node was designed with the same compliance, an error of 7.83% will be seen. This relationship was even more exaggerated when collecting the data using DIC, where the circular hinge only showed an error of 1.91%.

4.3.2 Strain Field Validation

The goal of this section is to compare the strain fields produced by the DIC analysis to that of the FEA analysis of the samples.

Figure 4.32 shows a collection of images taken from both FEA and DIC for each of the types of experimental nodes tested. From these images, it is difficult to conclude whether the FEA resembles the DIC. However, there are similarities between the two sources of data. The general shape that the preserve region forms on FEA can be roughly seen on the DIC as well. This is particularly true the closer the values are to the boundary between the node and the preserve region where the strain values are larger. Most of the images exhibit an elliptical shape in the high-strain regions. This is not compelling enough to say with certainty that the FEA resembles the same as the DIC results, hence why a more in-depth comparison of individual strain values was done in section 4.3.3. It is worth noting that from the strain field images, there is a clear outlier in the form of the Circular Hinge. It is nearly impossible to draw a shape from the results seen in this image. At best, it can be seen that the strain is localised near the node boundary. However, this provides very little useful information. As will be discussed later, the reason for this is the small strain values present in the preserve region. The effect of this can even be seen on

the FEA strain field, where the strain values are on average so low that even the minor strain values present further away from the node are included in the strain field.

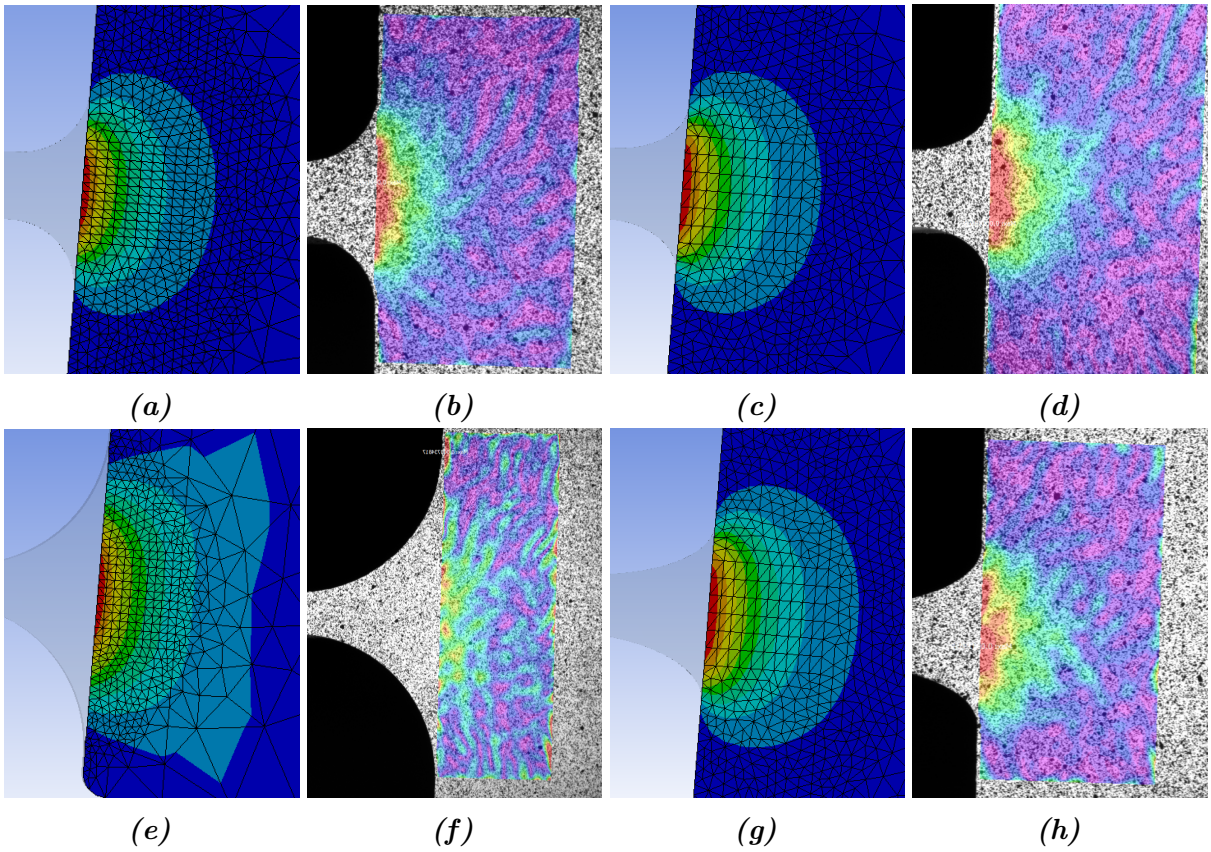

Figure 4.32: *Comparison between preserve regions on FEA and DIC. circular filleted: a) FEA b) DIC, elliptically filleted: c) FEA d) DIC, circular hinge: e) FEA f) DIC, elliptical hinge: g) FEA h) DIC*

4.3.3 Strain Line Validation

Following are the results comparing the strain values measured on DIC and FEA on the same lines past the nodes.

4.3.3.1 Circular Filleted

Figure 4.33 shows the strains for a set of horizontal lines at various vertical distances from the centre line for the circular filleted node. The starting point for all of the lines shows a

lower strain value on the DIC than what was to be expected from the FEA. The largest difference in value is at the line that is 4.5mm away from the centre of the preserve region with a value 29.92% lower on DIC than what was expected on FEA. This is substantially worse than the other 3 lines, with the next worst being 18.04%. Despite the start of the lines generally having less strain on the DIC than the FEA, the trend for both datasets is very similar. This is emphasized when looking at the exponential trendlines that are formed from the DIC datasets. Although all the trendlines begin lower than the FEA values, they nearly perfectly meet further down the line in a very similar shape.

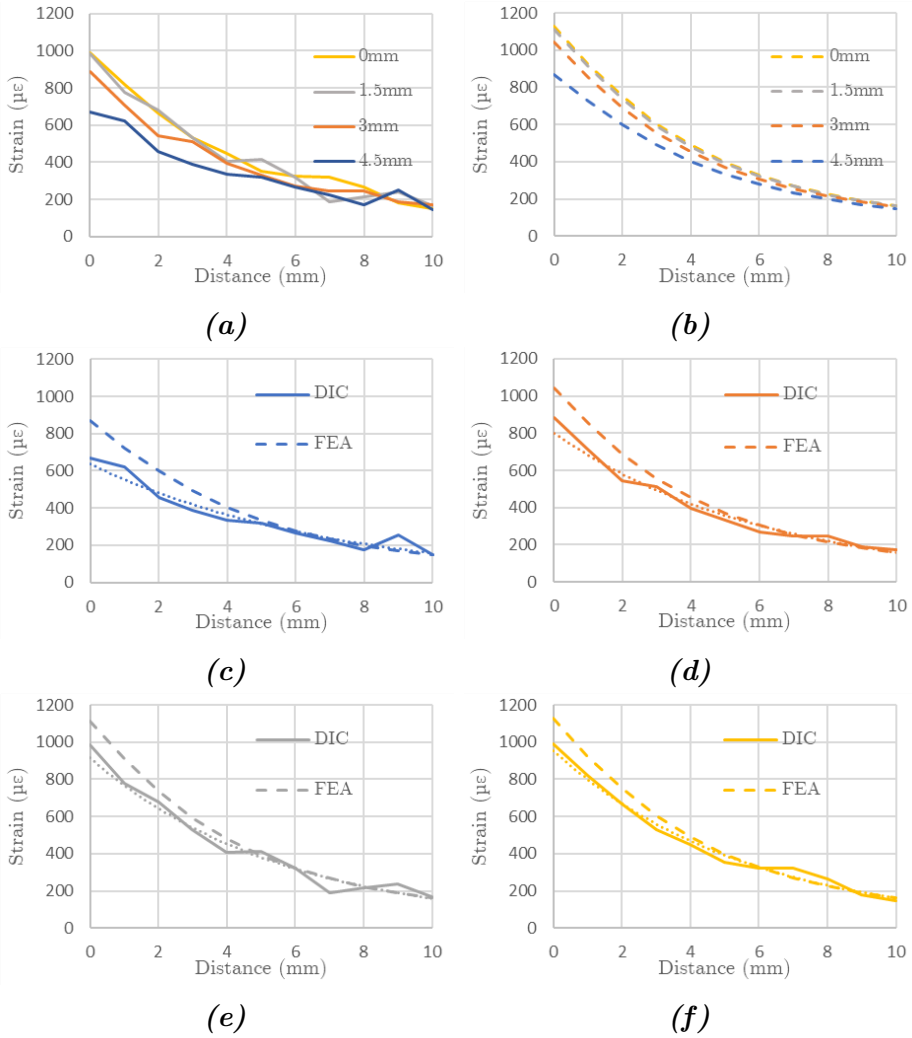

Figure 4.33: *Strain lines comparison between FEA and DIC for circular filleted node. a) All DIC values b) All FEA values c) Line 4.5mm above centre d) Line 3mm above centre e) Line 1.5mm above centre f) Line at centre*

4.3.3.2 Elliptically Filleted

In figure 4.34 are the results from the investigation using the elliptically filleted sample. Much like the investigation for the circular filleted sample, the lines all start with a lower value of strain than expected, and then continue to follow a trend very similar to that of the FEA results. This offset is even larger for this set of data, the maximum being at 4.5mm with a 39.09% difference between the FEA and the DIC. The same exponential trendline can be seen that shows a shape very similar to that of the previous investigation. Many of the lines in the elliptically filleted analysis appear to have an even stronger resemblance to an exponential relationship than the circular filleted sample.

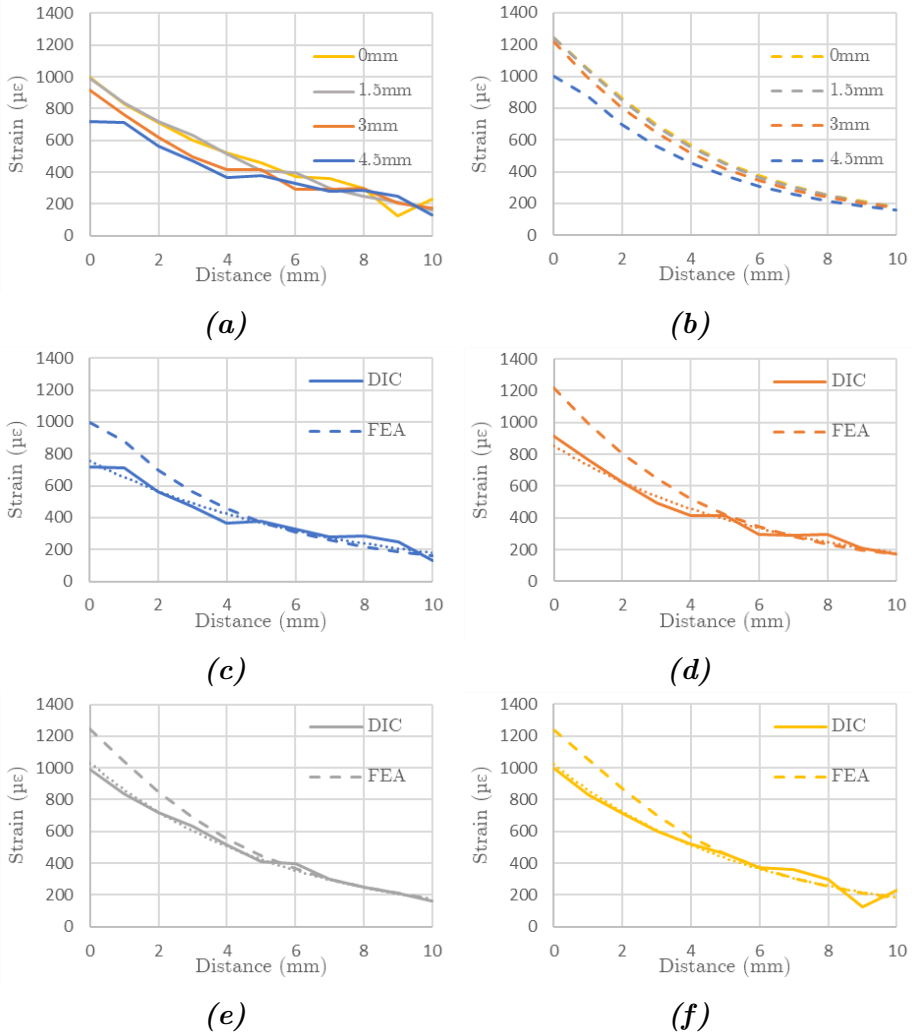

Figure 4.34: *Strain lines comparison between FEA and DIC for elliptically filleted node. a) All DIC values b) All FEA values c) Line 4.5mm above centre d) Line 3mm above centre e) Line 1.5mm above centre f) Line at centre*

4.3.3.3 Elliptical Hinge

In figure 4.35 are the results from the investigation using the elliptical hinge sample. The strain at the boundary of the elliptical hinge already shows a substantial difference from that of the previous samples. It shows individual values that are far more similar to that of the FEA, with the maximum difference being 17.27% and the minimum being 0.48%. However, the distribution of the strain along the node boundary appears far less consistent with that of the previous samples. The most likely cause for this is speckling. Looking at the images that were used to find this data there were some rather large black spots near the node, which can often introduce noise into the data. Although the first point of these lines appears to not be as consistent as previous samples, the strain further past the boundary is very similar to that of the FEA. This further reinforces that speckling was an issue present at the node boundary, as the consistency of the results saw a vast improvement after this point. The trend lines found for the DIC data are nearly identical for the line along the middle of the preserve region and the line 1.5mm above the centre. For the lines 3mm and 4.5mm above, the lines don't align as closely when compared to the more central lines. This is expected as the values of strain higher up in the preserve region have lower strain values and, therefore, are more susceptible to noise.

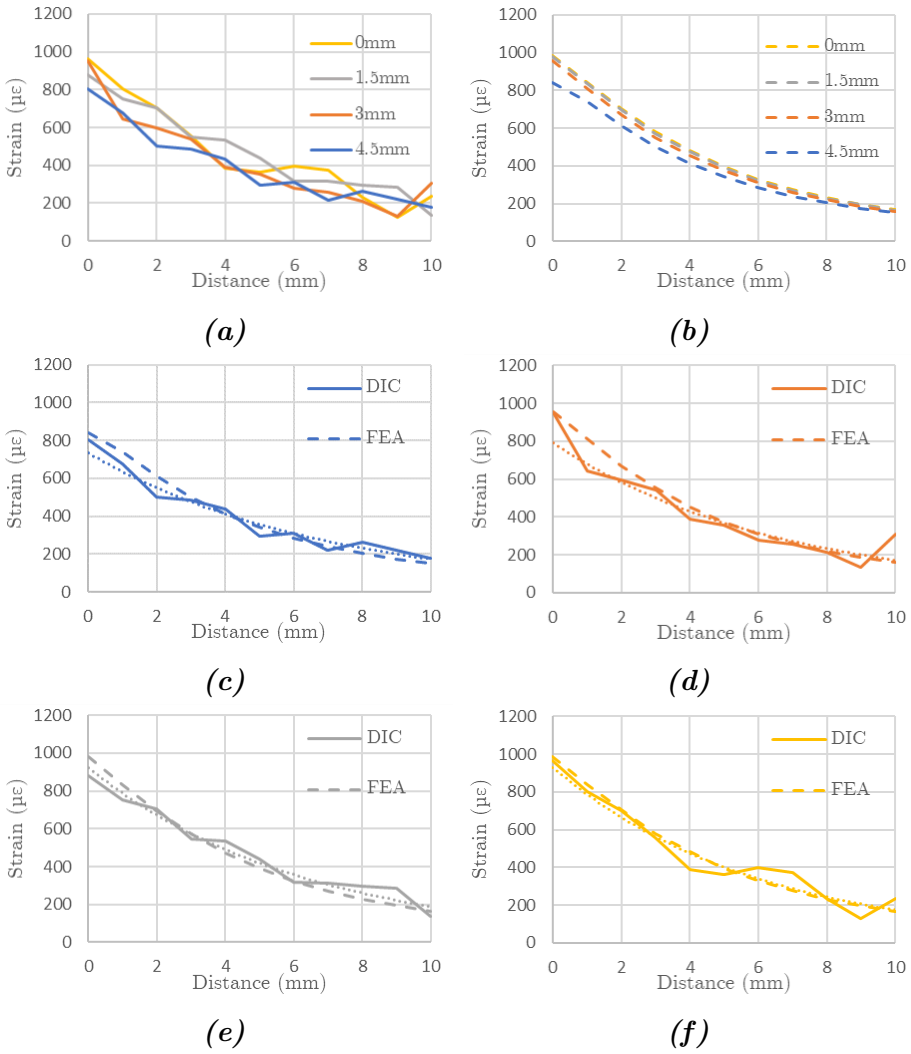

Figure 4.35: *Strain lines comparison between FEA and DIC for elliptical hinge node. a) All DIC values b) All FEA values c) Line 4.5mm above centre d) Line 3mm above centre e) Line 1.5mm above centre f) Line at centre*

4.3.3.4 Circular Hinge

In figure 4.36 are the results from the DIC analysis of circular hinges. Unfortunately, measuring strains within the preserve region of the circular hinge sample proved difficult. During the theoretical to FEA comparison, it was found that the circular hinge showed the least amount of error in tip displacement between the two methods. It would reason that this sample would have the least amount of strain outside of the node boundary contributing towards the error. This is seen on both the FEA and the DIC, where the

maximum strain found at the node boundary was 298$\mu\epsilon$ on FEA and 299$\mu\epsilon$ on DIC. This is substantially lower than the other samples, for example, the elliptically filleted sample had a maximum strain on DIC of 1000$\mu\epsilon$, more than 3 times the circular hinge. This means that the strain that is being measured is greatly affected by noise, as seen in the strain along the horizontal lines. This dataset gives no clear image of how the strain propagates, as the values are simply far too low to be accurately measured on the DIC. A slight trend can be seen where the strain appears to be reducing overall as the line moves further away from the node boundary, however, this trend is not clear enough to draw any conclusion on the shape of the strain distribution.

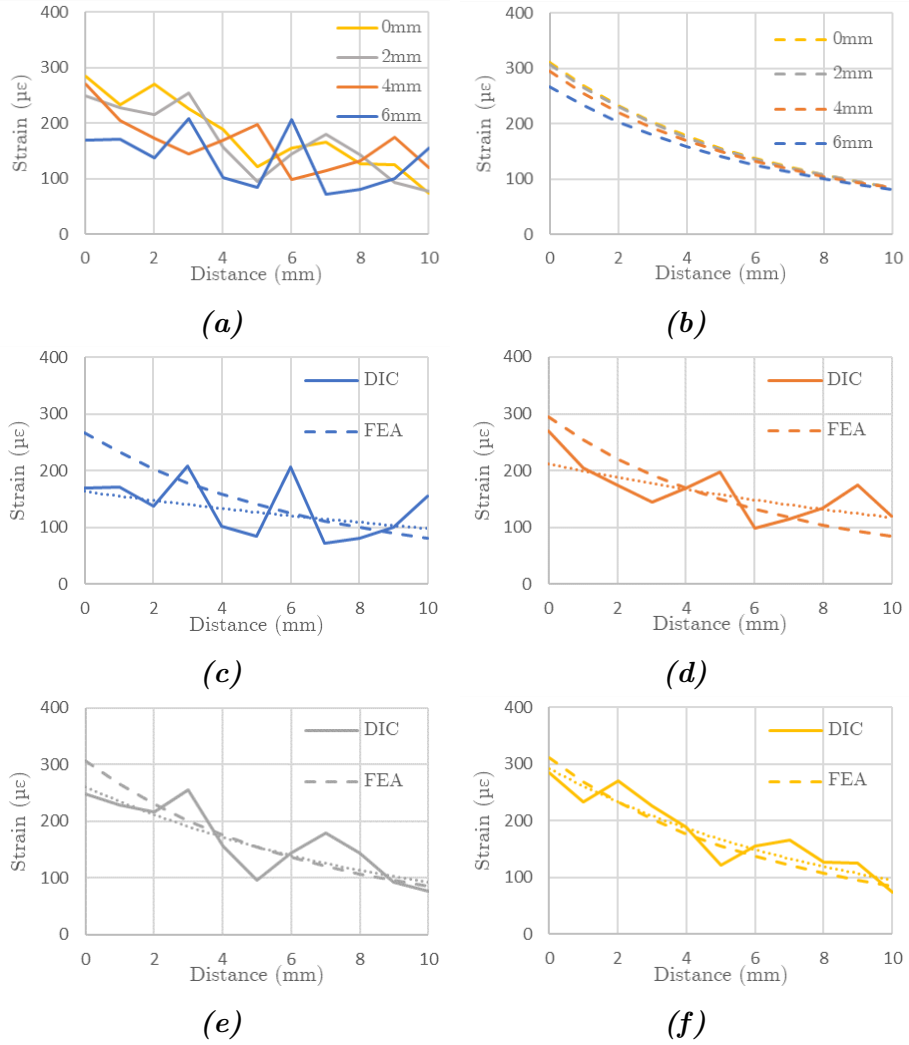

Figure 4.36: *Strain lines comparison between FEA and DIC for circular hinge node. a) All DIC values b) All FEA values c) Line 4.5mm above centre d) Line 3mm above centre e) Line 1.5mm above centre f) Line at centre*

4.3.4 FEA Validation Summary

The use of DIC has granted newfound confidence in the conclusions drawn about the impact the preserve region has on nodes and their modelling. On a displacement level, the error present in the FEA is also present within the experimental data as well, showing that the impact of the preserve region is consistent between the experimental samples and the simulated samples. However, to further solidify this, the strain values within the preserve region were analysed. Three out of the four experimental samples tested show a strong resemblance between the strain found within the preserve region in both the simulated data as well as the measured data. For the one sample that the trend could not be identified experimentally, there were practical reasons as to why it was not possible and can be easily remedied with a redesign of the sample. However, all other samples confirmed further that the use of FEA to understand the impact of the preserve region is accurate and appropriate.

4.4 Application

For every geometric variation done in the preserve region analysis section 4.2, the effective compliance that was found using FEA was verified. To do this, the loading scenario was slightly altered. When the effective compliance of the node was found, it was found using a reference point about the first hole on the sample, 62.5mm away from the node. To ensure that this value was correct, the effective compliance of the node was used to find the compliance about a reference point different to the one it was found with. Instead, the effective compliance of the node was translated to find the matrix about a reference point 92.5mm away from the node. Using the compliance for all of the geometric variation never exceeded an error value of 0.2%, meaning when the effective compliance of the node was found, it can be used instead of the theoretical compliance for a substantial increase in accuracy.

This case, however, is very limited, as it used the same sample with the same loading scenario only translated further down the mechanism. It does not account for the rotation of compliance matrices and the effect of axial loads. To help confidently verify whether or not the effective compliance found using this method is truly an improved substitute for the values found theoretically, a new mechanism was designed. The design can be seen in figure 4.37. It is made to resemble a parallel mechanism, where the top and bottom pieces remain parallel when a load is placed at the top. All of the nodes are identical and are circular filleted nodes with a thickness of 4mm, a length of 15mm and a fillet radius of 3mm. They sit at a 70-degree angle, and the material is assumed to be polypropylene with a stiffness of 1.725GPa. First, the mechanism will be modelled using only a theoretical approach to calculate the compliance of the nodes. The mechanism will then be modelled by finding the effective compliance of one of the nodes using the method discussed earlier. Both these compliances will be used to predict the motion the mechanism undergoes when a 60N load is placed at the top, after which FEA will be used to assess the accuracy of each method.

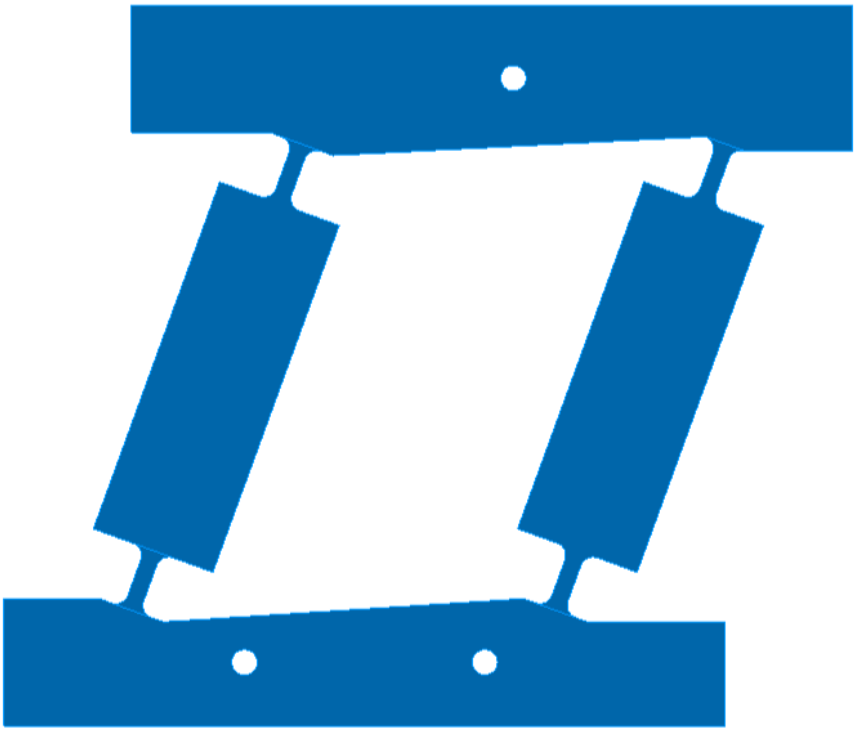

Figure 4.37: *Parallel mechanism tested*

When the theoretical compliances and effective compliances were found, there was a difference of 65.9%, 8.4% and 13.7% in the values for C_{y-fy}, C_{y-mz} and C_{z-mz} respectively. When the mechanism was loaded in FEA, a vertical displacement of 2.86mm was seen. When the mechanism was modelled using a theoretical approach, a vertical displacement value of 2.50mm was seen, while using the effective compliance showed an expected displacement of 2.88mm. This means that using an exclusively theoretical approach would have led to an error of 14.45%. While using the effective compliance, which accounts for the preserve region, gives an error of 0.56%. This shows the importance of the consideration of the preserve region in designing compliant mechanisms, as a great deal of error can be avoided for certain node geometries.

It is worth noting that while this approach was very effective at reducing the impact of sources of error such as the preserve region, there are circumstances where the compliance matrix method already produces an accurate model of the mechanism. For example, if the same loading scenario shown 4.37 was designed with much thinner nodes at 2.3mm thickness, the compliance matrix model only shows an error of 1.48%. This is already unlikely to need any further reductions in error, and using the effective compliance leads to an error that is slightly higher at 3.09%. In conclusion, the method used in the preserve region analysis to find the effective compliance of the node is most applicable for nodes that exhibit a large amount of error in the preserve region, which was found to be particularly thick samples.

Chapter 5

Conclusion

This work aimed to understand and describe key features of the preserve region present around the nodes used within compliant mechanisms. During this research, a method to isolate sources of error between the FEA and the theoretical results was devised, and through the use of DIC, the findings were verified with experimental data. Using this method granted insight into key geometric variables and their effect on the preserve region's size, shape, and impact on accuracy.

5.1 Preserve Region Size

The key observations were that geometries that reduce the strain outside of the would increase the size of the preserve region. It was found that the offset distance of the load, the size of the load, and the stiffness of the material had little effect on the preserve region. The variables that had a significant impact on the size of preserve region were the thickness, the radius of the fillet, and the major and minor axes of the fillet. Increasing all of these variables overall increased the thickness within the node, leading to a smaller amount of strain throughout the mechanism, making the strain within the preserve region much more impactful. The most substantial of these is the thickness. When the thickness

was increased from 4mm to 8mm, the size increased from an arc with a radius of 8.5mm to 13mm.

5.2 Preserve Region Shape

The strain was found to propagate in an elliptical shape. This conclusion was verified for all combinations of geometries by analysing the strain values in an elliptical shape and seeing the amount of variation in the values. This variation was insignificant for all of these geometries, although all of them did show some deviation closer to the corners of the node. This deviation could sometimes reach values of 17.82%. However, if the inconsistencies near the corners are removed, the worst variation seen is 6.17%. Increasing the radius and minor axis of the fillet had the largest impact on the shape of the preserve region regarding its suitability to an ellipse. Seeing as both the radius and the minor axis have this effect, it implies that the larger interface between the node boundary and the preserve region is likely the reason for the change in shape.

5.3 Preserve Region Impact

A part of the method within the preserve region analysis involved finding the compliance of the node by using measurements from FEA software. This method granted insights into how the preserve region impacts error on a theoretical level. However, there was room for improvement. With the inclusion of the preserve region into the compliance matrix, the compliance in the y direction due to a moment about the z direction saw only minor impacts from this increased strain, whilst the y compliance saw drastic changes. Of the geometries that impacted this value, by far the largest of them was the thickness and the length of the node. An increase in thickness from 4mm to 8mm increased the error for the compliance in the y direction due to a force in the y direction from 20.53% to 102.18%. This is due to these variables substantially increasing or decreasing the

compliances, making the compliance gained outside of the node either far more or far less impactful. The effective compliance was also found and tested for a multi-nodal mechanism and was found to be far more accurate than a purely theoretical approach to compliance.

5.4 Future Work

The research done has shown that the existence of the preserve region is substantial and worth considering when taking on a theoretical approach. The work done in this thesis, however, covered only a certain set of node types and loading scenarios. More investigation can be done into more unconventional node shapes and more elaborate loading scenarios and how this impacts the preserve region.

The method for finding the effective compliance could likely be revised as well. In its current form, it can grant good insights into what the true compliance of the node is, however with the method used to find it, it is very sensitive to inaccuracies and general noise. Changing the number of significant figures had a noticeable impact on the value that was found. However, it did not change any of the conclusions. Any other source of error would then be magnified with the current method, so a different set of loading scenarios should be used instead.

This investigation was also done within the context of the compliance matrix method. These observations cannot be transferred over to a different theoretical method, such as the pseudo-rigid-body model, for example, and therefore, a different method would have to be devised to understand the preserve region's impact on that model.

All of the analyses were also done with the samples being able to fully develop the preserve region with no interference in the form of voids or alterations to the area outside of the node. Investigation can be done into factors and variables outside of the node and what impact they have on the characteristics of the preserve region.

References

[1] Juan A Gallego and Just Herder. Synthesis methods in compliant mechanisms: An overview. In *International Design Engineering Technical Conferences and Computers and Information in Engineering Conference*, volume 49040, pages 193–214, 2009.

[2] S P Jagtap, B B Deshmukh, and S Pardeshi. Applications of compliant mechanism in today's world – a review. *Journal of Physics: Conference Series*, 1969(1):012013, jul 2021. doi: 10.1088/1742-6596/1969/1/012013. URL https://dx.doi.org/10.1088/1742-6596/1969/1/012013.

[3] Larry L. Howell, Spencer P. Magleby, and Brian M. Olsen. *Handbook of Compliant Mechanisms*. John Wiley & Sons, Incorporated, 2013. ISBN 978-1-118-51651-5. URL http://ebookcentral.proquest.com/lib/waikato/detail.action?docID=1119456.

[4] Mauricio Arredondo-Soto, Enrique Cuan-Urquizo, and Alfonso Gómez-Espinosa. The compliance matrix method for the kinetostatic analysis of flexure-based compliant parallel mechanisms: Conventions and general force–displacement cases. *Mechanism and Machine Theory*, 168:104583, February 2022. ISSN 0094-114X. doi: 10.1016/j.mechmachtheory.2021.104583. URL https://www.sciencedirect.com/science/article/pii/S0094114X21003256.

[5] Benliang Zhu, Xianmin Zhang, Hongchuan Zhang, Junwen Liang, Haoyan Zang, Hai Li, and Rixin Wang. Design of compliant mechanisms using continuum topology optimization: A review. *Mechanism and Machine Theory*, 143:103622,

2020. ISSN 0094-114X. doi: 10.1016/j.mechmachtheory.2019.103622. URL https://www.sciencedirect.com/science/article/pii/S0094114X19315538.

[6] Nicolae Lobontiu. *: Design of Flexure Hinges*. CRC Press, 2 edition, 2020. ISBN 978-0-429-18466-6. doi: 10.1201/9780429184666.

[7] Robert M. Fowler, Alex Maselli, Pieter Pluimers, Spencer P. Magleby, and Larry L. Howell. Flex-16: A large-displacement monolithic compliant rotational hinge. *Mechanism and Machine Theory*, 82:203–217, December 2014. ISSN 0094-114X. doi: 10.1016/j.mechmachtheory.2014.08.008. URL https://www.sciencedirect.com/science/article/pii/S0094114X14002055.

[8] Mark Naves, Marijn Nijenhuis, W.B.J. Hakvoort, and D.M. Brouwer. Flexure-based 60 degrees stroke actuator suspension for a high torque iron core motor. *Precision Engineering*, 63, February 2020. doi: 10.1016/j.precisioneng.2020.02.001.

[9] Lifang Qiu, Yuansong Liu, Yue Yu, and Yuntian Brian Bai. Design and stiffness analysis of a pitch-varying folded flexure hinge (PFFH). *Mechanism and Machine Theory*, 157:104187, March 2021. ISSN 0094-114X. doi: 10.1016/j.mechmachtheory.2020.104187. URL https://www.sciencedirect.com/science/article/pii/S0094114X20304043.

[10] Jelle Rommers and Just Herder. Design of a Folded Leaf Spring with high support stiffness at large displacements using the Inverse Finite Element Method. pages 2109–2118. June 2019. ISBN 978-3-030-20130-2. doi: 10.1007/978-3-030-20131-9_209.

[11] Larry L. Howell. *Compliant Mechanisms*. John Wiley & Sons, 2001. ISBN 978-0-471-38478-6. Google-Books-ID: tiiSOuhsIfgC.

[12] Sridhar Kota. Design of compliant mechanisms: applications to MEMS. In Vijay K. Varadan, editor, *Smart Structures and Materials 1999: Smart Electronics and MEMS*, volume 3673, pages 45 – 54. International Society for Optics and Photonics, SPIE, 1999. doi: 10.1117/12.354294. URL https://doi.org/10.1117/12.354294.

[13] O. Sigmund. A 99 line topology optimization code written in matlab. *Structural*

and Multidisciplinary Optimization, 21(2):120–127, 2001. ISSN 1615-1488. doi: 10.1007/s001580050176. URL https://doi.org/10.1007/s001580050176.

[14] Michael Yu Wang, Xiaoming Wang, and Dongming Guo. A level set method for structural topology optimization. *Computer Methods in Applied Mechanics and Engineering*, 192(1):227–246, 2003. ISSN 0045-7825. doi: 10.1016/S0045-7825(02)00559-5. URL https://www.sciencedirect.com/science/article/pii/S0045782502005595.

[15] Vivien J. Challis. A discrete level-set topology optimization code written in matlab. *Structural and Multidisciplinary Optimization*, 41(3):453–464, 2010. ISSN 1615-1488. doi: 10.1007/s00158-009-0430-0. URL https://doi.org/10.1007/s00158-009-0430-0.

[16] G. Allaire and O. Pantz. Structural optimization with $\tt{FreeFem++}$. *Structural and Multidisciplinary Optimization*, 32(3):173–181, 2006. ISSN 1615-147X, 1615-1488. doi: 10.1007/s00158-006-0017-y. URL http://link.springer.com/10.1007/s00158-006-0017-y.

[17] Xiaodong Huang and Yi-Min Xie. A further review of ESO type methods for topology optimization. *Structural and Multidisciplinary Optimization*, 41(5):671–683, 2010. ISSN 1615-147X, 1615-1488. doi: 10.1007/s00158-010-0487-9. URL http://link.springer.com/10.1007/s00158-010-0487-9.

[18] Erik Andreassen, Anders Clausen, Mattias Schevenels, Boyan S. Lazarov, and Ole Sigmund. Efficient topology optimization in MATLAB using 88 lines of code. *Structural and Multidisciplinary Optimization*, 43(1):1–16, 2011. ISSN 1615-147X, 1615-1488. doi: 10.1007/s00158-010-0594-7. URL http://link.springer.com/10.1007/s00158-010-0594-7.

[19] Cameron Talischi, Glaucio H. Paulino, Anderson Pereira, and Ivan F. M. Menezes. PolyTop: a matlab implementation of a general topology optimization framework using unstructured polygonal finite element meshes. *Structural and Multidisciplinary Optimization*, 45(3):329–357, 2012. ISSN 1615-1488. doi: 10.1007/s00158-011-0696-x. URL https://doi.org/10.1007/s00158-011-0696-x.

[20] Kai Liu and Andrés Tovar. An efficient 3d topology optimization code written in matlab. *Structural and Multidisciplinary Optimization*, 50(6):1175–1196, 2014. ISSN 1615-147X, 1615-1488. doi: 10.1007/s00158-014-1107-x. URL `http://link.springer.com/10.1007/s00158-014-1107-x`.

[21] Rouhollah Tavakoli and Seyyed Mohammad Mohseni. Alternating active-phase algorithm for multimaterial topology optimization problems: a 115-line MATLAB implementation. *Structural and Multidisciplinary Optimization*, 49(4):621–642, 2014. ISSN 1615-1488. doi: 10.1007/s00158-013-0999-1. URL `https://doi.org/10.1007/s00158-013-0999-1`.

[22] Zhi Hao Zuo and Yi Min Xie. A simple and compact python code for complex 3d topology optimization. *Advances in Engineering Software*, 85:1–11, 2015. ISSN 0965-9978. doi: 10.1016/j.advengsoft.2015.02.006. URL `https://www.sciencedirect.com/science/article/pii/S0965997815000241`.

[23] Weisheng Zhang, Jie Yuan, Jian Zhang, and Xu Guo. A new topology optimization approach based on moving morphable components (MMC) and the ersatz material model. *Structural and Multidisciplinary Optimization*, 53(6):1243–1260, 2016. ISSN 1615-147X, 1615-1488. doi: 10.1007/s00158-015-1372-3. URL `http://link.springer.com/10.1007/s00158-015-1372-3`.

[24] Rubén Ansola Loyola, Osvaldo M Querin, Alain Garaigordobil Jiménez, and Cristina Alonso Gordoa. A sequential element rejection and admission (sera) topology optimization code written in matlab. *Structural and Multidisciplinary Optimization*, 58: 1297–1310, 2018.

[25] Peng Wei, Zuyu Li, Xueping Li, and Michael Yu Wang. An 88-line MATLAB code for the parameterized level set method based topology optimization using radial basis functions. *Structural and Multidisciplinary Optimization*, 58(2):831–849, 2018. ISSN 1615-1488. doi: 10.1007/s00158-018-1904-8. URL `https://doi.org/10.1007/s00158-018-1904-8`.

[26] Dalibor Petkovic, Nenad D. Pavlovic, Shahaboddin Shamshirband, and Nor Badrul

Anuar. Development of a new type of passively adaptive compliant gripper. *The Industrial Robot*, 40(6):610–623, 2013. ISSN 0143991X. doi: 10.1108/IR-12-2012-452. URL https://www.proquest.com/docview/1442847092/abstract/A92F19E09DAE4903PQ/1. Num Pages: 610-623 Place: Bedford, United Kingdom Publisher: Emerald Group Publishing Limited.

[27] Annem Narayana Reddy, Nandan Maheshwari, Deepak Kumar Sahu, and G. K. Ananthasuresh. Miniature compliant grippers with vision-based force sensing. *IEEE Transactions on Robotics*, 26(5):867–877, 2010. ISSN 1941-0468. doi: 10.1109/TRO.2010.2056210. Conference Name: IEEE Transactions on Robotics.

[28] I-Ting Chi, Teeranoot Chanthasopeephan, and Dung-An Wang. Design of a Parallel Gripper Based on Topology Synthesis and Evolutionary Optimization. *Journal of Mechanisms and Robotics*, 14(021008), September 2021. ISSN 1942-4302. doi: 10.1115/1.4052335. URL https://doi.org/10.1115/1.4052335.

[29] Hisham A Maddah. Polypropylene as a promising plastic: A review. *Am. J. Polym. Sci*, 6(1):1–11, 2016.

[30] Yanling Tian, Bijan Shirinzadeh, and David Zhang. Closed-form compliance equations of filleted v-shaped flexure hinges for compliant mechanism design. *Precision Engineering*, 34(3):408–418, 2010.

[31] Farid Parvari Rad. Design and characterization of curved and spherical flexure hinges for planar and spatial compliant mechanisms. 2014.

[32] Ruiqi Li, Zhijun Yang, Bingyu Cai, Guimin Chen, Baisheng Wu, and Yutai Wei. A compliant guiding mechanism utilizing orthogonally oriented flexures with enhanced stiffness in degrees-of-constraint. *Mechanism and Machine Theory*, 167:104555, 2022.

[33] Simon Henein, Peter Spanoudakis, Serge Droz, Leif I Myklebust, and Emmanuel Onillon. Flexure pivot for aerospace mechanisms. In *Proceedings of the 10th European Space Mechanisms and Tribology Symposium*, pages 285–288, 2003.

[34] M. Rösner, R. Lammering, and R. Friedrich. Dynamic modeling and model order reduction of compliant mechanisms. *Precision Engineering*, 42:85–92, Oc-

tober 2015. ISSN 0141-6359. doi: 10.1016/j.precisioneng.2015.04.003. URL https://www.sciencedirect.com/science/article/pii/S0141635915000574.

[35] Marco Ceccarelli, Giorgio Figliolini, Erika Ottaviano, Antonio Simon Mata, and Emilio Jimenez Criado. Designing a robotic gripper for harvesting horticulture products. *Robotica*, 18(1):105–111, 2000.

[36] Ramesh Kolluru, Kimon P Valavanis, SS Smith, and Nikos Tsourveloudis. Design fundamentals of a reconfigurable robotic gripper system. *IEEE Transactions on Systems, Man, and Cybernetics-Part A: Systems and Humans*, 30(2):181–187, 2000.

[37] Henry Williams, Canaan Ting, Mahla Nejati, Mark Hedley Jones, Nicky Penhall, JongYoon Lim, Matthew Seabright, Jamie Bell, Ho Seok Ahn, Alistair Scarfe, et al. Improvements to and large-scale evaluation of a robotic kiwifruit harvester. *Journal of Field Robotics*, 37(2):187–201, 2020.

[38] Jung-Yuan Wang and Chao-Chieh Lan. A constant-force compliant gripper for handling objects of various sizes. *Journal of Mechanical Design*, 136(7), 2014. ISSN 1050-0472. doi: 10.1115/1.4027285. URL https://doi.org/10.1115/1.4027285.

[39] Eric Diller and Metin Sitti. Three-dimensional programmable assembly by untethered magnetic robotic micro-grippers. *Advanced Functional Materials*, 24(28):4397–4404, 2014.

[40] Gondi Kondaiah Ananthasuresh. *A new design paradigm for micro-electro-mechanical systems and investigations on the compliant mechanisms synthesis*. University of Michigan, 1994.

[41] Xiang Xi, Tyler Clancy, Xuezhong Wu, Yu Sun, and Xinyu Liu. A mems xy-stage integrating compliant mechanism for nanopositioning at sub-nanometer resolution. *Journal of Micromechanics and Microengineering*, 26(2):025014, 2016.

[42] Ted Nachazel. What is a strain gauge and how does it work? URL https://www.michsci.com/what-is-a-strain-gauge/.

[43] GRt Higson. Recent advances in strain gauges. *Journal of Scientific Instruments*, 41 (7):405, 1964.

[44] M. Fujigaki and Y. Morimoto. Sampling moiré method for accurate small deformation distribution measurement. *Experimental Mechanics*, 50(4):501–508, 2010. ISSN 1741-2765. doi: 10.1007/s11340-009-9239-4. URL https://doi.org/10.1007/s11340-009-9239-4.

[45] Po-Chih Hung and A. S. Voloshin. In-plane strain measurement by digital image correlation. *Journal of the Brazilian Society of Mechanical Sciences and Engineering*, 25: 215–221, 2003. ISSN 1678-5878, 1806-3691. doi: 10.1590/S1678-58782003000300001. URL http://www.scielo.br/j/jbsmse/a/bKv3tYCRZXB3bjLzGrWHHMQ/abstract/?lang=en. Publisher: Associação Brasileira de Engenharia e Ciências Mecânicas - ABCM.

[46] J McKelvie. Moiré strain analysis: An introduction, review and critique, including related techniques and future potential. *The Journal of Strain Analysis for Engineering Design*, 33(2):137–151, 1998. ISSN 0309-3247. doi: 10.1243/0309324981512878. URL https://doi.org/10.1243/0309324981512878. Publisher: IMECHE.

[47] Ole Lekberg. Electronic speckle pattern interferometry. *Physics in Technology*, 11(1):16, 1980. ISSN 0305-4624. doi: 10.1088/0305-4624/11/1/303. URL https://dx.doi.org/10.1088/0305-4624/11/1/303.

[48] Lianxiang Yang, Xin Xie, Lianqing Zhu, Sijin Wu, and Yonghong Wang. Review of electronic speckle pattern interferometry (ESPI) for three dimensional displacement measurement. *Chinese Journal of Mechanical Engineering*, 27(1): 1–13, 2014. ISSN 1000-9345, 2192-8258. doi: 10.3901/CJME.2014.01.001. URL http://link.springer.com/10.3901/CJME.2014.01.001.

[49] M.A.M. Bourke, D.C. Dunand, and E. Ustundag. SMARTS – a spectrometer for strain measurement in engineering materials. *Applied Physics A*, 74(1):s1707–s1709, 2002. ISSN 1432-0630. doi: 10.1007/s003390201747. URL https://doi.org/10.1007/s003390201747.

[50] Bing Pan, Kemao Qian, Huimin Xie, and Anand Asundi. Two-dimensional digital image correlation for in-plane displacement and strain measurement: a review. *Measurement Science and Technology*, 20(6):062001, 2009. ISSN 0957-0233. doi: 10.1088/0957-0233/20/6/062001. URL https://dx.doi.org/10.1088/0957-0233/20/6/062001.

[51] Martin Reis, Marcel Adorna, Ondřej Jiroušek, and Anne Jung. Improving DIC accuracy in experimental setups. *Advanced Engineering Materials*, 21 (7):1900092, 2019. ISSN 1527-2648. doi: 10.1002/adem.201900092. URL https://onlinelibrary.wiley.com/doi/abs/10.1002/adem.201900092. _eprint: https://onlinelibrary.wiley.com/doi/pdf/10.1002/adem.201900092.

[52] Harilal R, Mohammad Kashfuddoja, Saranath K M, and Ramji M. *Material Characterization of Carbon Fiber Reinforced Polymer Laminate Using Virtual Fields Method*. ResearchGate, 2014. doi: 10.13140/RG.2.1.2911.4406.

[53] S.-W. Khoo, S. Karuppanan, and C.-S. Tan. A review of surface deformation and strain measurement using two-dimensional digital image correlation. *Metrology and Measurement Systems*, pages 461–480, 2016. ISSN 0860-8229. doi: 10.1515/mms-2016-0028. URL https://www.infona.pl//resource/bwmeta1.element.baztech-f2855177-34dc-41e9-bf74-80f4121ce746.

[54] Jaroslav Hricko and Stefan Havlik. Vision-way testing in design of small compliant mechanisms. In Saïd Zeghloul, Med Amine Laribi, and Juan Sebastian Sandoval Arevalo, editors, *Advances in Service and Industrial Robotics*, Mechanisms and Machine Science, pages 588–595. Springer International Publishing, 2020. ISBN 978-3-030-48989-2. doi: 10.1007/978-3-030-48989-2_62.

[55] Sheng Yao, Hai Li, Shuiquan Pang, Longhuan Yu, Sergej Fatikow, and Xianmin Zhang. Motion measurement system of compliant mechanisms using computer micro-vision. *Optics Express*, 29(4):5006–5017, 2021. ISSN 1094-4087. doi: 10.1364/OE.415097. URL https://opg.optica.org/oe/abstract.cfm?uri=oe-29-4-5006. Publisher: Optica Publishing Group.

[56] Heng Wu, Xianmin Zhang, Jinqiang Gan, Hai Li, and Zhenya He. High-precision displacement measurement method for three degrees of freedom-compliant mechanisms based on computer micro-vision. *Applied Optics*, 55(10):2594–2600, 2016. ISSN 2155-3165. doi: 10.1364/AO.55.002594. URL `https://opg.optica.org/ao/abstract.cfm?uri=ao-55-10-2594`. Publisher: Optica Publishing Group.

[57] fit_ellipse, February 2024. URL `https://au.mathworks.com/matlabcentral/fileexchange/3215-fit_ellipse`.

[58] PPI Home. URL `https://www.plasticpipe.org/PPI-Home/PPI-Home/Default.aspx`.

[59] ASTM International. *Standard test method for tensile properties of plastics*. ASTM international, 2014.

[60] William N Findley and Francis A Davis. *Creep and relaxation of nonlinear viscoelastic materials*. Courier corporation, 2013.

[61] Can-Can Zhang, Jun-Long Yang, Ya-Jiang Huang, and Guang-Xian Li. Highly improved creep resistance in polypropylene through thermally reduced graphene oxide and its creep lifetime prediction. *Chinese Journal of Polymer Science*, pages 1–11, 2023.

Chapter 6

Appendix

6.1 DIC Testing Parameters

Test	Subset Size	Step Size	Calibration Score	Angle of Cameras (◦)
CF Strain	29	7	0.078	28.47
CF Displacement	31	7	0.086	28.47
CH Strain	44	8	0.071	28.47
CH Displacement	31	7	0.086	28.43
EF Strain	35	8	0.078	28.47
EF Displacement	35	7	0.086	28.43
EH Strain	31	7	0.086	28.43
EH displacement	31	7	0.086	28.43

The average value of projected error never exceeded a value 0.1, as per the recommendation from the supplier. The software used was VIC 3D Version 9. The cameras were two AVT Alvium 12.4MP cameras with 60mm lenses.

6.2 Dogbone Testing Results

Table 6.1: Stiffness testing results for dogbones

Test Number	Stiffness (MPa)
1	2051.39
2	1986.35
3	2007.37
4	1805.24
5	1924.41
6	1959.18
7	1990.11
8	2024.52
Average	1968.57

The stiffness values were found with the built-in software for the Instron. A strain gauge was placed directly on the sample, and a 5Kn load cell was used.

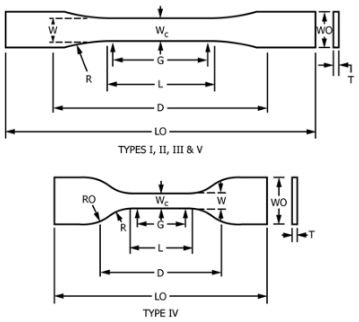

Specimen Dimensions for Thickness, *T*, mm (in.)[A]

Dimensions (see drawings)	7 (0.28) or under		Over 7 to 14 (0.28 to 0.55), incl	4 (0.16) or under		Tolerances
	Type I	Type II	Type III	Type IV[B]	Type V[C,D]	
W—Width of narrow section[E,F]	13 (0.50)	6 (0.25)	19 (0.75)	6 (0.25)	3.18 (0.125)	±0.5 (±0.02)[B,C]
L—Length of narrow section	57 (2.25)	57 (2.25)	57 (2.25)	33 (1.30)	9.53 (0.375)	±0.5 (±0.02)[C]
WO—Width overall, min[G]	19 (0.75)	19 (0.75)	29 (1.13)	19 (0.75)	...	+ 6.4 (+ 0.25)
WO—Width overall, min[G]	...	...	...	...	9.53 (0.375)	+ 3.18 (+ 0.125)
LO—Length overall, min[H]	165 (6.5)	183 (7.2)	246 (9.7)	115 (4.5)	63.5 (2.5)	no max (no max)
G—Gage length[I]	50 (2.00)	50 (2.00)	50 (2.00)	...	7.62 (0.300)	±0.25 (±0.010)[C]
G—Gage length[I]	...	...	...	25 (1.00)	...	±0.13 (±0.005)
D—Distance between grips	115 (4.5)	135 (5.3)	115 (4.5)	65 (2.5)[J]	25.4 (1.0)	±5 (±0.2)
R—Radius of fillet	76 (3.00)	76 (3.00)	76 (3.00)	14 (0.56)	12.7 (0.5)	±1 (±0.04)[C]
RO—Outer radius (Type IV)	...	...	...	25 (1.00)	...	±1 (±0.04)

Figure 6.1: *ASTM standard dogbone sample dimensions*

For the purposes of this thesis, a type three dogbone sample was used.